

# Electrochemical Machining of Gold Nanostructures and Optical Characterization with Cathodoluminescence

Zur Erlangung des akademischen Grades eines

DOKTORS DER NATURWISSENSCHAFTEN

(Dr. rer. nat.)

der Fakultät für Chemie und Biowissenschaften

Karlsruher Institut für Technologie (KIT) – Universitätsbereich

Genehmigte

DISSERTATION

Von

**Xinzhou Ma**

Aus

Guangdong, China

Dekan: Prof. Dr. Matrin Bastmeyer

Referent: Prof. Dr. Rolf Schuster

Korreferent: PD. Dr. Andreas-Neil Unterreiner

Tag der mündlichen Prüfung: 16. 12. 2011



# Contents:

<b>Contents:</b> .....	<b>I</b>
<b>Zusammenfassung</b> .....	<b>III</b>
<b>Abstract</b> .....	<b>VI</b>
<b>Chapter 1 Introduction</b> .....	<b>1</b>
<b>Chapter 2 Theoretical background</b> .....	<b>6</b>
2.1 Electrochemical micromachining with ultra-short voltage pulses .....	6
2.1.1 Principle of electrochemical micromachining.....	6
2.1.2 Comparison with other micro- and nanofabrication methods .....	9
2.2 Propagating surface plasmons at planar metal/dielectric interfaces .....	11
2.2.1 Dispersion relation of propagating surface plasmons .....	11
2.2.2 Excitation of surface plasmon polaritons by light.....	15
2.2.3 Excitation of propagating surface plasmons by electrons .....	15
2.3 Localized surface plasmons .....	17
2.4 Optical properties of gold and silver .....	18
<b>Chapter 3 Experimental details</b> .....	<b>21</b>
3.1 Chemicals.....	21
3.2 Electrochemical micromachining set-up.....	21
3.3 Measurement of the differential capacitance.....	24
3.4 Light collection and detection for cathodoluminescence experiments.....	24
3.4.1 Light collection with optical fibers .....	24
3.4.2 Light collection with a parabolic mirror.....	28
3.4.3 Detection of low light levels and photon counting.....	32
3.4.4 Spectrally resolved measurements .....	33
3.4.5 Angular intensity distribution measurements .....	35
<b>Chapter 4 Electrochemical machining of gold microstructures</b> .....	<b>37</b>
4.1 Electrochemical behavior of gold in different solutions .....	37
4.1.1 Gold in aqueous chloride solutions .....	37
4.1.2 Gold in LiCl/DMSO solutions .....	39
4.1.3 Gold in LiCl/DMSO-water mixtures.....	43
4.1.4 Thermodynamic considerations .....	46
4.1.5 Differential capacitance of gold in LiCl/DMSO .....	50
4.1.6 Specific resistance of LiCl in DMSO-water mixtures.....	53
4.1.7 Electrochemistry of LiCl/DMSO at carbon fibers.....	54
4.2 Electrochemical machining of gold nanostructures .....	56
4.2.1 Preparation of carbon fiber tools .....	56
4.2.2 Electrochemical micromachining of gold .....	61
4.3 Conclusions.....	71
<b>Chapter 5 Cathodoluminescence of gold nanostructures</b> .....	<b>73</b>
5.1 Electron-specimen interactions .....	73
5.2 Cathodoluminescence .....	74

---

5.2.1 Cherenkov radiation .....	75
5.2.2 Bremsstrahlung and Transition Radiation .....	76
5.2.3 Radiative plasmons .....	78
5.3 Cathodoluminescence of smooth silver and gold surfaces.....	79
5.4 Panchromatic CL maps of gold structures.....	84
5.5 Cathodoluminescence of silver particles.....	91
5.6 Angular distribution of emitted light.....	93
5.8 Conclusions and Outlook .....	108
<b>Chapter 6 Cathodoluminescence of silver and gold tips .....</b>	<b>110</b>
6.1 Nanometer-sized metal tip: an optical antenna .....	110
6.2 Preparation of gold and silver tips.....	112
6.2.1 Preparation of gold tips .....	112
6.2.2 Preparation of silver tips .....	113
6.3 Cathodoluminescence of silver tips.....	114
6.4 Cathodoluminescence of gold tips .....	119
6.5 Conclusions and outlook.....	126
<b>Chapter 7 Light emission from scanning tunneling microscope.....</b>	<b>128</b>
7.1 Light emission induced by inelastically tunneling electrons in an STM.....	128
7.2 Home-built scanning tunneling microscope for light emission investigations.....	131
7.3 STM induced light emission .....	137
7.3.1 Light emission from flat gold films.....	137
7.3.2 Light emission from gold microstructures .....	139
7.4 Conclusions, problems and outlook .....	140
<b>Appendix.....</b>	<b>142</b>
<b>Bibliography .....</b>	<b>144</b>
<b>Acknowledgments .....</b>	<b>150</b>
<b>Publications.....</b>	<b>152</b>
<b>Curriculum Vitae .....</b>	<b>153</b>

# Zusammenfassung

Die optischen Eigenschaften metallischer Nanostrukturen werden größtenteils von der Anregbarkeit kollektiver Elektronenschwingungen, meist sogenannte Oberflächenplasmonen, bestimmt. Um ein besseres Verständnis der an Nanostrukturen anregbaren Oberflächenplasmonen, sowie der Verteilung und Verstärkung des elektromagnetischen Nahfeldes in der unmittelbaren Umgebung solcher Strukturen zu erlangen, befasst sich diese Arbeit mit i) der Entwicklung eines Verfahrens zur Herstellung von Gold-Nanostrukturen mittels elektrochemischer Mikrostrukturierung sowie ii) mit der optischen Charakterisierung der elektrochemisch hergestellten Gold-Nanostrukturen anhand ihrer Kathodolumineszenz, die entweder mit dem hochenergetischen Elektronenstrahl eines Rasterelektronenmikroskops (scanning electron microscope, SEM), oder mit inelastischen Tunnelelektronen in einem Rastertunnelmikroskop (scanning tunneling microscope, STM) lokal angeregt werden kann.

Zur elektrochemischen Herstellung der Gold-Nanostrukturen auf Goldfolien oder -filmen wurden ultrakurze Spannungspulse an eine „Werkzeug-Elektrode“ angelegt, mit deren Hilfe, ähnlich einem Miniaturfräser, möglichst tiefe, dreidimensionale Strukturen aus der Goldoberfläche herausgefräst wurden. Die Verwendung ultrakurzer Spannungspulse im Nanosekundenbereich bewirkte eine Eingrenzung der elektrochemischen Reaktionen auf Bereiche, in denen sich die beiden Elektroden in unmittelbarer Nähe zueinander befanden. Die Spaltbreite zwischen Werkzeug und -stück hängt im Wesentlichen von der Ladezeitkonstante der Doppelschichtkapazität ab und skaliert daher ca. linear mit Pulslänge und Elektrolytwiderstand. Die Verwendung von Elektrolyten mit hohem spezifischem Widerstand war daher von Vorteil, sodass in dieser Arbeit LiCl/DMSO-Elektrolyte anstelle von wässrigen Lösungen verwendet wurden.

Zur Bestimmung der elektrochemischen Bearbeitungsparameter wurde zunächst das

elektrochemische Verhalten von Gold in wasserfreien und wasserhaltigen LiCl/DMSO-Lösungen mittels zyklischer Voltammetrie untersucht. Das Gold wurde als Au(I)-Komplex, wahrscheinlich  $[\text{AuCl}_2]^-$ , gelöst. Die hohe Stabilität von  $[\text{AuCl}_2]^-$  in DMSO führte zu einem stark irreversiblen Verhalten des Redoxprozesses und einem 800 mV breiten elektrochemischen Potentialfenster zwischen der Goldabscheidung und -auflösung. Dagegen liegt Gold in wässrigen chloridhaltigen Lösungen als  $[\text{AuCl}_4]^-$  vor, das leicht reduzierbar ist. Die Zugabe von Wasser zu LiCl/DMSO verkleinerte das elektrochemische Potentialfenster signifikant, was der Destabilisierung von  $[\text{AuCl}_2]^-$  zugeschrieben wurde. Um routinemäßig eine hohe Bearbeitungsgenauigkeit zu erreichen und um adäquate elektrochemische Parameter für das Strukturieren im submikrometer-Bereich zu bestimmen, wurde der Einfluss der Pulsdauer und -amplitude sowie des eingestellten Ruhepotentials auf die Präzision der Strukturen umfassend untersucht. Eine Spaltbreite von 100 nm wurde durch das Anlegen von Potentialpulsen mit moderaten Pulsdauern in der Größenordnung von 10 ns in LiCl/DMSO realisiert.

Die optischen Eigenschaften der hergestellten Goldstrukturen wurden zunächst mittels Lichtemission durch Anregung mit inelastischen Tunnelelektronen in einem STM untersucht. Befand sich die Au-Spitze nahe der Kante einer zum Beispiel mikrometergroßen dreieckigen Goldstruktur, trat eine erhöhte Emission auf. Aufgrund einiger Schwierigkeiten bei den benötigten hohen Tunnelspannungen, wie Goldoxidation, wurden die optischen Eigenschaften der Goldstrukturen anhand ihrer Kathodolumineszenz bei Bestrahlung mit 15keV Elektronen in einem SEM näher untersucht. Zur effizienten Erfassung des emittierten Lichts wurde ein Parabolspiegel verwendet. Die ortsabhängige Anregung von Lichtemission an Nanostrukturen wurde anhand von Photonenkarten dargestellt. Zur Bestimmung der Austrittswinkel des emittierten Lichts wurde eine Methode entwickelt, die die Emissionsrichtungen ( $\theta$ ,  $\varphi$ ) aus der Projektion des Lichts auf einen Farb-CCD-Chip ermittelt. Zusätzlich wurden mit einem Monochromator mit CCD-Detektor Emissionsspektren aufgenommen. Zu Vergleichszwecken wurden die Kathodolumineszenz von 200 nm dicken, glatten

Goldfilmen, und von mechanisch polierten Goldfolien untersucht. Sowohl die Winkelverteilung, als auch das Emissionsmaximum im grünen Spektralbereich zeigten, dass die Lichtemission flacher Goldoberflächen bei Anregung mittels Elektronen von Übergangsstrahlung dominiert wird. Trifft der Elektronenstrahl jedoch auf Gold-Mikrostrukturen, wie beispielsweise mikrometerbreite Balken, submikrometergroße Pyramiden oder Dreiecke, so wird die Lichtemission stark erhöht. Aus den Emissionsspektren ergab sich für diesen Fall zudem ein Maximum im roten Spektralbereich. Die erhöhte Emission wurde der Anregung von Oberflächenplasmonen, die ihre Energie durch Strahlung abgeben, zugeschrieben. Analog hierzu wurde auch am Apex elektrochemisch geätzter Gold- bzw. Silberspitzen Anregung von Oberflächenplasmonen beobachtet.

Beim Übergang von der Bestrahlung relativ großer, flacher Strukturen, wie eines mikrometergroßen Au-Balkens, zur Bestrahlung des Apex von Au-Pyramiden im Nanometerbereich änderte sich die Winkelverteilung der Lichtemission stark. Die Bestrahlung des Au-Balkens führte zur Emission von rotem Licht mit Zenitwinkeln von  $60^\circ$  bis  $75^\circ$ , während bei der Bestrahlung der Au-Pyramide rotes Licht mit Zenitwinkeln von weniger als  $35^\circ$  beobachtet wurde. Wegen der relativ großen, flachen Oberfläche des Au-Balkens wurde die Lichtemission in diesem Fall auf die effektive Streuung propagierender Oberflächenplasmonen an den Kanten der Struktur zurückgeführt. Die Ursache der Emission am Pyramiden-Apex kann dagegen durch das Auftreten von strahlenden, lokalisierten Oberflächenplasmonen mit parallel zur Goldoberfläche oszillierendem Dipolmoment erklärt werden.

# Abstract

The optical properties of metallic nanostructures are to a large extent determined by their susceptibility towards the excitation of collective electron oscillations mostly bound to the surface, i.e., so called surface plasmons. In order to gain better understanding about such surface plasmons on nanostructures as well as the distribution and the enhancement of the electromagnetic near field in the vicinity of the nanostructures, this thesis concentrates on: i) the development of a method for the fabrication of gold nanostructures by electrochemical machining; ii) the optical characterization of the electrochemically fabricated gold structures by their cathodoluminescence (CL), which is locally induced either with a high energy electron beam in a scanning electron microscope (SEM) or with inelastically tunneling electrons in a scanning tunneling microscope (STM).

For electrochemically fabricating gold nanostructures out of gold sheets or films, ultra-short voltage pulses were applied to a tool electrode, which was then mechanically fed like a miniature milling cutter into a gold sheet in order to obtain thick, three dimensional structures. Due to the application of ultra-short voltage pulses in the nanosecond range to the electrodes, the electrochemical reactions are strongly confined to regions, where both electrodes are in very close proximity. The gap width between tool and workpiece is essentially determined by the charging time constant of the double layer capacitance and is hence about proportional to pulse duration and electrolyte conductivity. Therefore, the application of electrolytes with rather high specific electrolyte resistance is beneficial and LiCl/DMSO electrolytes rather than aqueous solutions were chosen for the electrochemical machining of gold. In order to determine the electrochemical machining parameters, the electrochemical behavior of gold in LiCl/DMSO with and without water was studied with cyclic voltammetry. Gold was dissolved as Au(I) complex, probably  $[\text{AuCl}_2]^-$  in LiCl/DMSO. The high stability of  $[\text{AuCl}_2]^-$  in DMSO resulted in a strongly irreversible behavior of gold dissolution/deposition and the electrochemical potential-window between gold



dissolution/deposition was as wide as 800mV. In contrast, in aqueous chloride solutions gold was dissolved as  $[\text{AuCl}_4]^-$  and the electrochemical potential window between gold dissolution/deposition was narrow. Upon addition of water to LiCl/DMSO, the electrochemical potential window between gold dissolution/deposition was significantly narrowed, which was attributed to strong destabilization of  $[\text{AuCl}_2]^-$ . In order to determine appropriate electrochemical parameters for the routine machining of sub-micrometer gold structures, the influence of the machining parameters, like pulse duration and amplitude, the rest potential of gold workpiece on the machining precision was thoroughly investigated. A machining precision of the order of 100nm was achieved by application of voltage pulses with moderate pulse durations of the order of 10ns in LiCl/DMSO.

Optical properties of the fabricated gold structures were first investigated with scanning tunneling microscope induced light emission. Enhanced emission was observed when an Au-tip closed to the edges of, e.g., micrometer sized triangular gold structures. However, due to some difficulties under ambient conditions in requirement of high bias voltages, such as gold surface oxidation, the optical properties of the electrochemically fabricated gold structures were then investigated by their cathodoluminescence upon irradiation with 15keV electrons in an SEM. For efficient collection of the emitted light, a parabolic mirror was employed. The spatially dependent excitation of light emission on nanostructures was reflected by their photon maps. In order to reveal the emission angle of the emitted light, an angularly resolved method was developed, i.e., revealing the emission directions ( $\theta, \varphi$ ) from the projection of the emitted light on a color CCD-chip. In addition, spectra of the emitted light were recorded with a monochromator and a CCD detector. As a reference, the cathodoluminescence of 200nm thick, flat Au films as well as of mechanically polished Au foils was studied. Both, the angular distribution of the emitted light and the emission spectra peaking in the green spectral region indicated that transition radiation was the predominant contribution to the observed light from electron beam irradiated flat gold surfaces. Upon electron irradiation of gold microstructures, like a micrometer wide Au-bar, sub-micrometer sized Au-pyramids, triangles, strongly

enhanced emission was observed when the electron beam hit the gold structures. Spectral measurements revealed that maximum emission was in the red spectral region. The enhanced emission was ascribed to excitation of radiatively decaying surface plasmons. Similarly, excitation of surface plasmons at the apex of electrochemically etched Au-tips and Ag-tips was also observed.

The angular emission pattern changed strongly when going from the irradiation of relatively wide, flat structured elements like a  $\mu\text{m}$ -wide Au bar to irradiation of the apex of nanometer-sized Au-pyramids. Grazing emission of red light with zenith angles between  $60^\circ$  and  $75^\circ$  was found for irradiation of the Au-bar. Whereas for the Au-pyramid, emission of red light with zenith angles less than  $35^\circ$  was found. Due to irradiation of the flat surface on the relatively wide Au-bar, light emission was ascribed to the effective scattering of propagating surface plasmons at the edges of the Au-bar. In contrast the light emitted from the nanometer-sized pyramid apex was better described as originating from radiative localized surface plasmons with an oscillating dipole parallel to the gold substrate surface.

# Chapter 1 Introduction

Surface plasmons<sup>[1]</sup>, i.e., oscillations of surface electrons associated with surface electromagnetic waves bounded to metal/dielectric interfaces, were first theoretically predicted by Ritchie<sup>[2]</sup> in 1957. The existence of surface plasmons was then experimentally demonstrated by the characteristic electron energy losses in aluminum which were measured by Powell and Swan two years later<sup>[3]</sup>. Surface plasmons were then intensively studied, e.g., with electron energy loss spectroscopy<sup>[4-6]</sup> and via radiation from electron irradiated roughened metal surfaces<sup>[7-9]</sup>, during the 1960's and 70's. The excitation of surface plasmons by light was also developed during the same period by Otto<sup>[10]</sup>, Raether and Kretschmann<sup>[11]</sup>. On planar metal surfaces, e.g., silver and gold, surface plasmons excited by light are also called surface plasmon polaritons, which propagate along metal/dielectric interfaces<sup>[12]</sup>. Surface plasmons attract broad interest from physicists, chemists, material scientists and biologists for their applications to manipulate and focus light at nanometer scale. These propagation properties of the surface plasmon polaritons provide pathways for scientists to miniaturize photonics devices and open an avenue for merging photonics with electronics at nanometer scale<sup>[13, 14]</sup>, regardless of the optical diffraction limit of conventional dielectric photonics devices. Extraordinary transmission of light through an array of sub-wavelength holes in silver film was discovered by Ebbesen and his co-workers<sup>[15]</sup>. The extraordinary transmission of light was understood by the coupling of light with surface plasmons via the hole array, i.e., surface plasmons, excited by the incoming light were in turn converted to light at the backside of the film, which led to the enhanced transmission.

In addition to guiding light along designed pathways, metallic nanostructures, nanoparticles and nanocavities can act as 'focusing elements' or so called optical antennas<sup>[16]</sup> to effectively concentrate light into a very small volume upon the excitation of so called localized surface plasmons. Oscillations of electrons on the 'focusing elements', which are excited by light, in turn generate their own

electromagnetic field associated with the oscillations. At specific frequencies, collective oscillations may be excited which result in strongly enhanced electromagnetic fields, compared to that of the exciting light<sup>[1]</sup>. The strongly enhanced electromagnetic field localized in the vicinity of the ‘focusing elements’ relates to various phenomena and applications. Examples are light emission from a scanning tunneling microscope<sup>[17, 18]</sup>, enhanced second harmonic generation<sup>[19, 20]</sup>, surface enhanced Raman scattering (SERS)<sup>[21, 22]</sup> and tip-enhanced Raman scattering (TERS)<sup>[23, 24]</sup>. Vibration spectroscopy, for example conventional Raman scattering, provides detailed information on the structure of molecules<sup>[21]</sup>. However, its applications are usually limited by the extremely small Raman cross sections in the order of  $10^{-30}$  cm<sup>2</sup> per molecule<sup>[22]</sup>. In surface enhanced Raman scattering (SERS), local electromagnetic field enhancement, confined to small metal structures, plays a very important role<sup>[25]</sup>. In theory, the enhancement factor of the Raman intensity scales with the forth power of the enhancement of the electric field<sup>[26]</sup>. Therefore, by excitation of localized surface plasmons on silver colloids, leading to a strongly enhanced electric field in the vicinity of them, cross sections of  $10^{-15}$  cm<sup>2</sup> per molecule were obtained and single molecule detection became possible<sup>[21, 22]</sup>. Recently, Tian et al. coated Au nanoparticles with a thin silica film or a thin alumina film, which served as substrates for surface enhanced Raman spectroscopy, in order to avoid the distortion of vibration information via preventing the direct interactions between adsorbate and the Au nanoparticles<sup>[27]</sup>. However, the reproducible fabrication of SERS active substrates is still challenging for routine applications of SERS as an analytical spectroscopic tool<sup>[28, 29]</sup>. Recently, AFM and STM tips were used for local field enhancement in tip-enhanced Raman spectroscopy<sup>[23, 24]</sup>. A metallic tip provides a relatively uniform geometry and reproducible local field enhancement<sup>[28]</sup>. The theoretically predicted electric field enhancement can be up to  $10^3$  inside the cavity<sup>[30-32]</sup>, formed by a tip and a substrate, however, the predicted enhancements of Raman intensity of up to 12 orders of magnitude were not experimentally obtained and only  $10^7$  fold enhancements were reported so far<sup>[24, 33]</sup>.

In order to get better understanding of surface plasmons as well as the resulting

surface electric field distribution, surface plasmons can be directly imaged by a scanning near field optical microscope (SNOM) with a typical resolution of about 50nm<sup>[12]</sup>. To avoid the perturbation of the tip on the local near field<sup>[12]</sup>, surface plasmons, which were locally excited on metallic nanostructures by a highly focused electron beam, were investigated using electron energy loss spectroscopy<sup>[34-36]</sup> and cathodoluminescence<sup>[37-41]</sup>, recently.

This thesis yields at the optical characterization of three dimensional, individually prepared, metallic, e.g., Au and Ag nanostructures, in order to gain better understanding and characterization of the electromagnetic near field in the vicinity of the designed metallic nanostructures upon excitation of surface plasmons. In contrast to employ conventional micromachining methods like focused ion beam milling or electron beam lithograph, we fabricated gold structures using our electrochemical micromachining method with ultra-short voltage pulses<sup>[42]</sup>. In order to study the geometry and size dependent electromagnetic near field distribution, various gold structures were designed and successfully fabricated, e.g., square columns, triangles and pyramids, which were scaled from a few micrometers to a few 100nm and extended from two dimensions to three dimensions. The following optical characterization of the electrochemically fabricated gold structures was mainly performed with cathodoluminescence, i.e., light emission induced with a highly focused electron beam in a scanning electron microscope. Furthermore, in order to clarify the role of the metallic tips and the nanometer-sized cavities in tip-enhanced spectroscopy, optical properties of free-standing Au-tips and Ag-tips were also studied with cathodoluminescence. In addition, the properties of the nanometer-sized cavities were investigated with STM induced light emission.

This thesis is organized as following: After this introduction, the second chapter briefly introduces the principle of the electrochemical micromachining method based on ultra-short voltage pulses and its advantages in comparison with other modern fabrication techniques. Theoretical basis of surface plasmons, e.g., the excitation of propagating surface plasmons and localized surface plasmons by light and by electrons, is also introduced. The dielectric properties of gold and silver between the

near ultra violet (UV) and the near infrared (IR) spectral regime are also discussed in the second part of this chapter.

Experimental details on the electrochemical micromachining set-up and low level light collection and detection for cathodoluminescence appear in chapter 3. The description of a developed method for measuring angular distribution of the emitted light is also included in this chapter.

In chapter 4, the electrochemical behavior of gold in LiCl/DMSO and in LiCl/DMSO-H<sub>2</sub>O mixtures is thoroughly discussed. The different electrochemical behavior of gold in these solutions is considered from a thermodynamic point view. The double layer capacitance of gold in LiCl/DMSO and the specific electrolyte resistance of 1M LiCl in DMSO-H<sub>2</sub>O mixtures are also discussed in this chapter, in order to estimate the charging time constant of the double layer of gold in LiCl/DMSO. A detailed description on the preparation of carbon fiber tools and the influence of the machining parameters like pulse duration and amplitude, rest potentials of gold workpieces and carbon fiber tools, as well as the water content in the electrolytes on the machining precision are also parts of this chapter. The fabrication of a few sub-micrometer structures, e.g., a high aspect ratio Au-structure of a 2 x 2 pillar array, is also presented.

In chapter 5, various contributions to the observed light upon bombardment with high energy electrons, i.e., Cherenkov radiation, Bremsstrahlung, transition radiation and radiative plasmons, are considered. The spectra as well as the spatial intensity distribution of light emitted from the electrochemically fabricated gold structures and silver particles are also studied in this chapter. Additionally, emission directions ( $\theta$ ,  $\varphi$ ) of light emitted from 200nm thick Au-films, a relatively big Au-bar and apexes of the nanometer-sized Au-pyramids are measured, in order to support the assignment of the origin of the observed light.

In chapter 6, preparation of Au-tips and Ag-tips by electrochemical etching is described. Optical properties of an individual Au-tip and an individual Ag-tip are also studied by cathodoluminescence. The spatial intensity distribution of the light emitted from a free-standing Au-tip and from a free-standing Ag-tip, as well as the spectra of

the emitted light, are measured and discussed.

In chapter 7, a home-built scanning tunneling microscope (STM) with a lateral manipulator for positioning the fabricated gold structures to an Au-tip is briefly described. Light emission from Au films and from fabricated Au nanostructures, induced by inelastically tunneling electrons in the home-built STM, are studied.

# Chapter 2 Theoretical background

## 2.1 Electrochemical micromachining with ultra-short voltage pulses<sup>[42, 43]</sup>

### 2.1.1 Principle of electrochemical micromachining

The principle of electrochemical micromachining with ultra-short voltage pulses is sketched in Fig. 2.1 (a). It is based on the local charging of the double layers (DL) at the electrode/electrolyte interfaces upon application of ultra-short voltage pulses between the tool electrode and the workpiece electrode. An equivalent circuit between the tool electrode and the workpiece electrode is also sketched. There are two capacitors, at the tool/electrolyte interface and at the workpiece/electrolyte interface, respectively, in series with an electrolyte resistor. The electrodes are assumed to be ideally polarizable electrodes and the effect of electrochemical reactions is disregarded for simplicity<sup>[43]</sup>. Upon application of voltage pulses between the tool and the workpiece, the charging current flows into the two capacitors via the electrolyte resistor, which results in the raising of the local potentials. The charging time constant  $\tau$  of the double layers is dependent on the overall capacitance  $C_{DL}$  of the equivalent circuit and the electrolyte resistance  $R$ , as given by  $\tau = RC_{DL}$ . The overall capacitance  $C_{DL}$  is related to the tool capacitance  $C_{tool}$  and the workpiece capacitance  $C_{wp}$  by

$$\frac{1}{C_{DL}} = \frac{1}{C_{wp}} + \frac{1}{C_{tool}}.$$

The electrolyte resistances are locally different, since the length of the charging current paths  $d$  are dependent on the local separations between the electrodes. In a simple model assuming parallel electrodes, if the specific electrolyte resistance is  $\rho$ , the electrolyte resistance  $R$  at a separation  $d$  of the electrodes is equal to  $\rho d$ . Thus the charging time constant of the double layers is proportional to the separation of the electrodes, as expressed by  $\tau = \rho d C_{DL}$ .

By application of a voltage pulse with amplitude  $U$  and duration  $t$  between the tool



and the workpiece, the overall charging potential across the two interfaces  $\Phi_{DL}$  is dependent on the charging time constant  $\tau$ , as given by equation 2.1:

$$\Phi_{DL} = U \left[ 1 - \exp\left(-\frac{t}{\tau}\right) \right] \quad \text{where } \tau = \rho d C_{DL}. \quad (2.1)$$

As sketched in Fig. 2.1 (a),  $R_S$  represents a small electrolyte resistance at a small separation between the electrodes and  $R_L$  represents a large electrolyte resistance at a large separation between the electrodes. The smaller electrolyte resistance  $R_S$  results in a smaller charging time constant. The charging amplitudes of the double layers at two locations upon the pulse with duration  $t$  are plotted in Fig. 2.1(b). In both curves, the charging amplitude increases with time during the voltage pulse. At the end of the pulse the double layers are significantly charged at the electrode areas where the charging time constant is small due to the small separation of the electrodes; in contrast the double layers are just slightly charged upon the same pulse at electrode areas where the charging time constant is large due to the large local separation of the electrodes. For a typical specific electrolyte resistance of  $\rho=30\Omega\cdot\text{cm}$  (0.1M  $\text{HClO}_4$ ) and a typical double layer capacitance of  $c=10\mu\text{F}\cdot\text{cm}^{-2}$  [44], the charging time constant  $\tau$  is 30ns for a separation  $d=1\mu\text{m}$  between parallel electrodes [42]. By employing a 30ns pulse, the double layers at this separation are charged by 63% of the applied pulse amplitude. In contrast, if the separation of the electrodes is as wide as  $3\mu\text{m}$ , the double layers are only charged by 28% of the applied pulse amplitude with the same duration. Thus, the charging amplitude of the double layers is very sensitive to the separation of the electrodes, in the order of micrometers.

The charging amplitude at an individual interface, i.e., the workpiece/electrolyte interface and the tool/electrolyte interface, is proportional to the overall charged amplitude  $\Phi_{DL}$  and reversely proportional to the respective capacitances. The corresponding charging amplitudes on the workpiece and on the tool can be calculated by equation 2.2, where  $\Phi_{DL}$  is the total charging amplitude given by equation 2.1:

$$\begin{aligned}\Phi_{\text{wp}} &= \frac{C_{\text{tool}}}{C_{\text{tool}} + C_{\text{wp}}} \Phi_{\text{DL}} \\ \Phi_{\text{tool}} &= \frac{C_{\text{wp}}}{C_{\text{tool}} + C_{\text{wp}}} \Phi_{\text{DL}}.\end{aligned}\quad (2.2)$$

For a small separation, both double layers are significantly polarized at the electrode/electrolyte interfaces. The fast raising potential at the workpiece  $\Phi_{\text{wp}}$ , adds to its rest potential and eventually exceeds the threshold potentials of electrochemical reactions. Thus the electrochemical reactions are driven at these surface areas. For a slightly larger electrode separation, the slowly raising potential adding to its rest potential stays lower than the onset potentials of electrochemical reactions and no electrochemical reaction occurs there. According to Butler-Volmer equation for the charge transfer controlled electrochemical reactions, the rate of the electrochemical reactions is exponentially dependent on the potential drop across the double layer. The rate increases by one order of magnitude with increasing potential of  $60\text{mV}/\alpha n$  at room temperature, where  $n$  is the number of transferred electrons per reacted molecule and  $\alpha$  is the transfer coefficient<sup>[45]</sup>. Therefore, the charging amplitude of the double layers and the resulting electrochemical reactions are very sensitive to the separation of the electrodes. The electrochemical reactions are strongly confined to the workpiece surface areas where they are in close proximity to the tool.

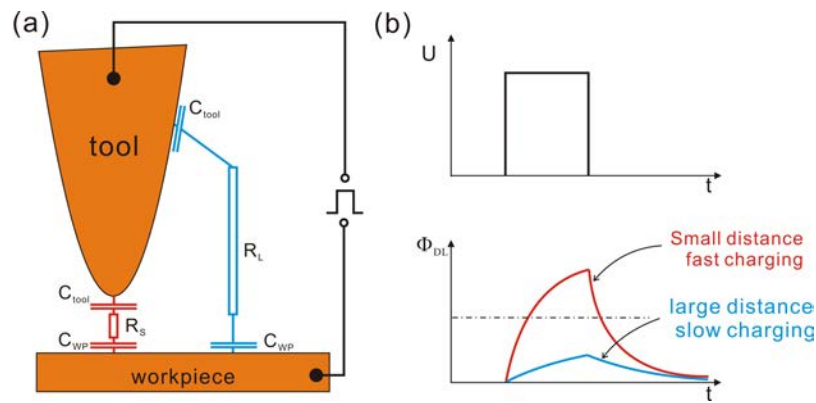


Fig. 2.1 (a) Scheme of the principle of electrochemical micromachining using ultra-short voltage pulses; (b) Plots of the charging amplitude of the double layers versus pulse duration, dependent on the charging current path indicated in (a), fast charging is achieved due to the short charging current path and slow charging results from the long charging current path.

## 2.1.2 Comparison with other micro- and nanofabrication methods

There are many methods, which were developed for micro- and nanofabrication. It is impossible to describe each method here. The widely used micro- and nanofabrication methods can be roughly divided into two groups: mask and mask-less methods. Generally, for the mask based methods, patterns on a mask are transferred to a photoresist, covering the substrate surfaces, by UV exposure or X-ray exposure<sup>[46]</sup> for high aspect ratio structures. Then the patterns on the photoresist are further transferred to the substrates by various etching methods or by filling the patterns, e.g., by metal deposition. The etching methods include wet etching (chemical etching, electrochemical etching etc.) and dry etching (plasma, reactive ion etching and deep reactive ion etching etc.)<sup>[47]</sup>. In addition to traditional lithography, soft lithography is a novel method to achieve functional surface patterns<sup>[48]</sup>. The mask-less micro- and nanofabrication techniques are mainly based on direct writing on the substrates by laser<sup>[49]</sup>, electron beam<sup>[50]</sup>, focus ion beam<sup>[51, 52]</sup>, scanning probe<sup>[53-55]</sup> and so on. With the micromachining methods based on electrochemistry, similar to our method, the

modifications at the electrode/electrolyte interfaces are mainly based on localized deposition or etching induced by small tools, e.g., a tip in STM<sup>[56, 57]</sup>, a microelectrode in SECM<sup>[58]</sup> and a patterned tool electrode in the confined etchant layer technique (CELT)<sup>[59]</sup>. However those structuring methods are mainly limited to two dimensional electrode/electrolyte interface and they are difficult to be used for high aspect ratio structure constructions. Detailed comparisons between our electrochemical micromachining method with other three-dimensional micromachining techniques like electrical discharge machining (EDM)<sup>[60]</sup>, LIGA<sup>[61]</sup>, focus ion beam milling<sup>[52]</sup>, laser ablation<sup>[62, 63]</sup> can be found, e.g., in Dr. Kock's Ph.D thesis<sup>[64]</sup>. In those techniques, only LIGA and focus ion beam milling can achieve machining precisions comparable with our electrochemical micromachining method. The requirements of thick photoresist layers and the expensive synchrotron radiation X-ray exposure source<sup>[61]</sup> limit the wide application of LIGA. Focus ion beam milling is a powerful tool for the fabrication of three dimensional micro- and nanostructures. However, it also has disadvantages, e.g., i) the high cost for the set-up and the maintenance; ii) the unavoidable surface damage during the high energy ion milling. Compared with those three dimensional micromachining techniques, our electrochemical micromachining with short voltage pulses has several advantages: i) capability to fabricate very high aspect ratio structures with submicron precisions on most electrochemically active materials; ii) relatively low cost of the experimental set-up, maintenance and the machining process; iii) a mask-less and freely designable process, no multi-steps as in lithography is required; iv) nearly no surface damage like ion implantation, except slight roughness due to corrosion. This method was successfully applied to microstructuring of many metals and semiconductors, including Cu<sup>[42]</sup>, Ni<sup>[65]</sup>, stainless steel<sup>[66]</sup>, iron<sup>[67]</sup> and Si<sup>[68]</sup>. All those experiments were carried out in aqueous solutions. In this thesis, nonaqueous solutions, i.e., LiCl/DMSO, are used for micromachining of gold. In comparison with aqueous solutions, nonaqueous solutions show some advantages, e.g., relatively wide electrochemically stable window; relatively low specific electrolyte conductivity at the same ions strength. More details can be found in chapter 4.

## 2.2 Propagating surface plasmons at planar metal/dielectric interfaces

### 2.2.1 Dispersion relation of propagating surface plasmons

Oscillations of surface electrons of metals can be excited by either light or by impinging electrons, in general by an external electric field. Such an excited surface electron density oscillation, propagating along a planar metal/dielectric interface longitudinally, is called propagating surface plasmons<sup>[1]</sup>. As sketched in Fig. 2.2 (a), a surface electron density wave  $\sigma(x, t)$ , oscillating with a frequency of  $\omega$  and propagating along the x-direction with a wave vector of  $\mathbf{q}$ , can be described by equation 2.3<sup>[69]</sup>:

$$\sigma(x,t) = \sigma_0 \exp i(\mathbf{q}x - \omega t), \quad (2.3)$$

where  $\sigma_0$  is the amplitude of the electron density wave.

The surface electron density wave  $\sigma(x, t)$  is accompanied by a surface electromagnetic field. Since there must be a component of the electric field normal to the interface, a p-polarized (transverse magnetic, TM) electromagnetic field is produced by the surface electron wave  $\sigma(x, t)$ <sup>[70]</sup>. Therefore, the magnetic field  $\mathbf{H}$  of the p-polarized electromagnetic field is perpendicular to the propagation direction  $x$  at the interface. Hence, magnetic field  $\mathbf{H}$  only has the component in  $y$  direction, i.e.,  $\mathbf{H}_y$ . The electric field of the p-polarized electromagnetic field is perpendicular to the magnetic field  $\mathbf{H}_y$  with a component  $\mathbf{E}_x$  (longitudinal component) along the interface and a component  $\mathbf{E}_z$  (transverse component) perpendicular to the interface. Therefore the electromagnetic field at an ideal metal/dielectric interface is expressed by equation 2.4<sup>[1, 70]</sup>:

$$\begin{aligned} \text{Metal:} \quad \mathbf{E}_1 &= E_1^0(x,0,z) \exp i(\mathbf{k}_{z1} |Z_1|) \exp i(\mathbf{q}x - \omega t) \\ \mathbf{H}_1 &= H_1^0(0,y,0) \exp i(\mathbf{k}_{z1} |Z_1|) \exp i(\mathbf{q}x - \omega t) \\ \text{Dielectric:} \quad \mathbf{E}_2 &= E_2^0(x,0,z) \exp i(\mathbf{k}_{z2} |Z_2|) \exp i(\mathbf{q}x - \omega t) \\ \mathbf{H}_2 &= H_2^0(0,y,0) \exp i(\mathbf{k}_{z2} |Z_2|) \exp i(\mathbf{q}x - \omega t). \end{aligned} \quad (2.4)$$

In equation 2.4, subscript 1 represents the electromagnetic field on the metal side and subscript 2 represents the electromagnetic field on the dielectric side.  $E_j^0(x, 0, z)$  ( $j=1, 2$ ) represents the amplitude of the electric field in x and z directions and  $H_j^0(0, y, 0)$  ( $j=1, 2$ ) represents the amplitude of the magnetic field in y direction in both metal and dielectric sides.  $|Z_1|$  is the decay length of the electric field inside the metal and  $|Z_2|$  is the decay length of the electric field inside the dielectric medium.

Since wave vector  $\mathbf{k}_{zj}$  in z direction and wave vector  $\mathbf{q}$  in x direction are the components of the wave vector of light  $\sqrt{\epsilon_j} \frac{\omega}{c}$  [69], the relation between  $\mathbf{k}_{zj}$  and  $\mathbf{q}$  is given by equation 2.5:

$$\mathbf{k}_{zj}^2 + \mathbf{q}^2 = \epsilon_j \left( \frac{\omega}{c} \right)^2, j = 1, 2. \quad (2.5)$$

For nonradiative surface plasmons, the wave vector  $\mathbf{k}_{zj}$  is imaginary and the transverse component of the electric field exponentially decays with increasing distance from the interface into metal and dielectric medium<sup>[1]</sup>. The decay length  $|Z_2|$  of the electric field in the dielectric medium is of the order of 100nm and the decay length  $|Z_1|$  for the metal is of the order of 10nm, depending on the frequency and the permittivity properties of metals and dielectric media<sup>[1]</sup>. The ratio of the longitudinal component  $E_x$  and the transverse component  $E_z$  of the electric field is given by  $-\mathbf{i}\mathbf{k}_z/\mathbf{q}$  on the dielectric side and  $\mathbf{i}\mathbf{k}_z/\mathbf{q}$  on the metal side<sup>[29]</sup>.

The dispersion relation  $\omega\text{-}\mathbf{q}$  of propagating surface plasmons (surface plasmon polaritons) at a metal/dielectric interface can be obtained from Maxwell's equations and the continuity boundary conditions, as expressed by equation 2.6<sup>[1]</sup>:

$$\mathbf{q}(\omega) = \frac{\omega}{c} \left( \frac{\epsilon_m(\omega)\epsilon_d(\omega)}{\epsilon_m(\omega) + \epsilon_d(\omega)} \right)^{1/2}. \quad (2.6)$$

Where  $\mathbf{q}$  is the wave vector of the propagating surface plasmons;  $\epsilon_m(\omega)$  and  $\epsilon_d(\omega)$  are the frequency dependent dielectric constants of the metals and the dielectric media, respectively.

According to the Drude model for free electron metals, the complex dielectric constant  $\varepsilon_m(\omega)$  of the free electron metals is given by equation 2.7<sup>[29]</sup>:

$$\begin{aligned}\varepsilon_m(\omega) &= \varepsilon_m'(\omega) + i\varepsilon_m''(\omega) = 1 - \frac{\omega_p^2 \tau^2}{\omega^2 \tau^2 + i\omega\tau} \\ \varepsilon_m'(\omega) &= 1 - \frac{\omega_p^2 \tau^2}{1 + \omega^2 \tau^2}, \quad \varepsilon_m''(\omega) = \frac{\omega_p^2 \tau}{\omega(1 + \omega^2 \tau^2)}.\end{aligned}\quad (2.7)$$

Where  $\varepsilon_m'(\omega)$  and  $\varepsilon_m''(\omega)$  are the real and the imaginary components of the frequency dependent dielectric constant  $\varepsilon_m(\omega)$  of the metals.  $\omega_p$  is the bulk plasmon frequency of the metals, which is given by  $\omega_p^2 = 4\pi n e^2 / m$ <sup>[71]</sup> ( $n$  is the electron density of the metals;  $e$  is the electron charge;  $m$  is the effective electron mass).  $\tau$  is the relaxation time of the free electrons, which is of the order of  $10^{-14}$  s at room temperature for most metals<sup>[71]</sup>.

As an approximation, at high frequencies, i.e.,  $\omega\tau \gg 1$ , the imaginary part of the complex dielectric constant of the metals  $\varepsilon_m''(\omega) \approx 0$  and hence the dielectric constant of metals  $\varepsilon_m(\omega) \approx \varepsilon_m'(\omega) = 1 - \frac{\omega_p^2}{\omega^2}$ . The dispersion relation  $\omega$ - $\mathbf{q}$  of propagating

surface plasmons at a planar metal/vacuum interface is obtained by substituting of  $\varepsilon_m(\omega) \approx \varepsilon_m'(\omega) = 1 - \frac{\omega_p^2}{\omega^2}$  and  $\varepsilon_d(\omega) = 1$  into equation 2.6, as expressed by equation

2.8:

$$\left(\frac{\omega(\mathbf{q})}{\omega_p}\right)^2 = \frac{1}{2} + \left(\frac{c\mathbf{q}}{\omega_p}\right)^2 - \sqrt{\frac{1}{4} + \left(\frac{c\mathbf{q}}{\omega_p}\right)^4}.\quad (2.8)$$

The dispersion relation of surface plasmons described by equation 2.8<sup>[70]</sup> is plotted by a solid curve in Fig. 2.2 (b). According to equation 2.5, the wave vector  $\mathbf{k}_{zj}$  is imaginary, thus the wave vector of the nonradiative propagating surface plasmons  $\mathbf{q}$  along the interface is larger than the wave vector of light  $\omega/c$  ( $\varepsilon=1$ ) in vacuum. Therefore, as indicated in Fig. 2.2 (b), the dispersion curve of the propagating surface plasmons is on the right side with respect to the line of  $\omega/c$ .

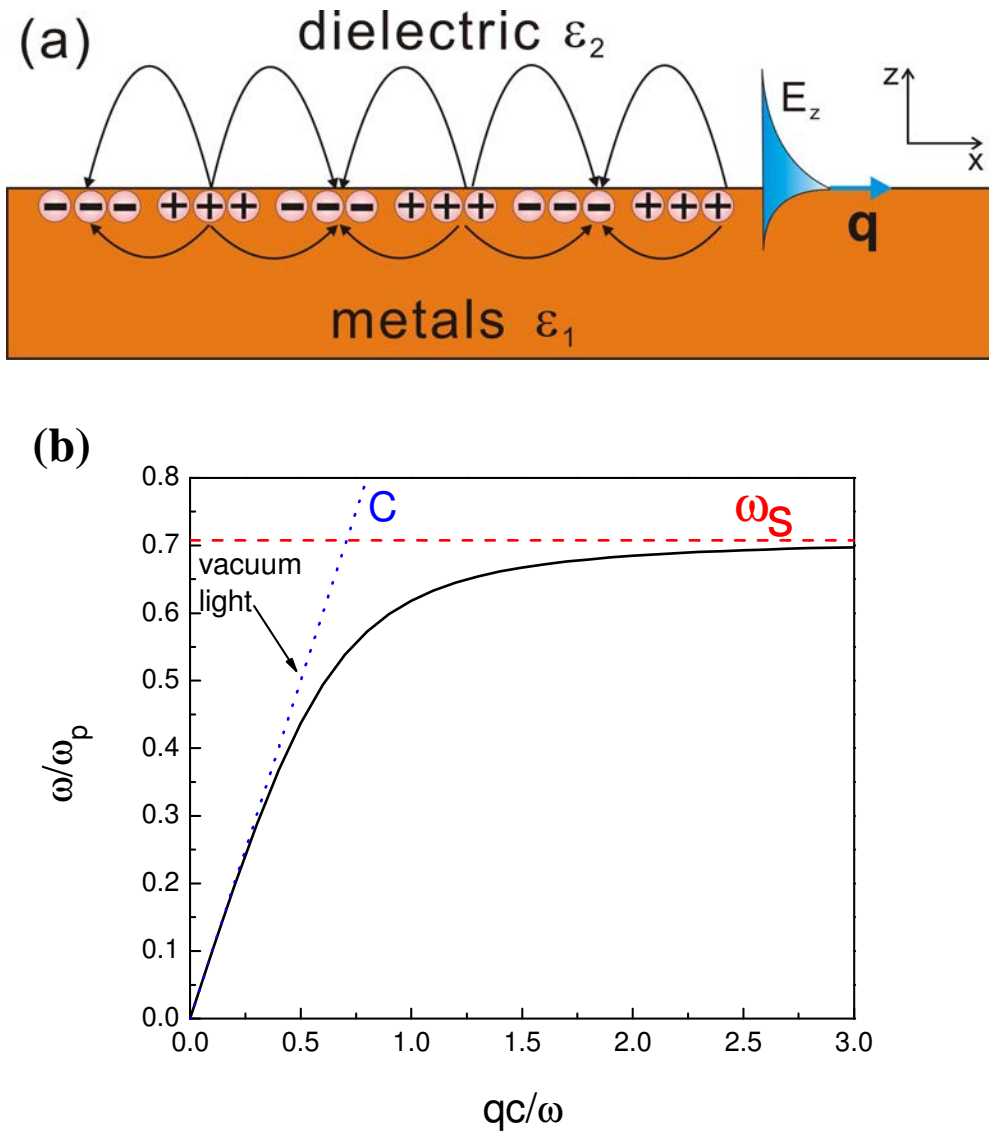


Fig. 2.2 (a) Scheme of an electron density wave propagating along a metal/dielectric interface with a wave vector of  $\mathbf{q}$  and the associated electromagnetic near fields; (b) Plot of the dispersion relation of propagating surface plasmons at the interface between a free electron metal and vacuum (solid line); the blue dotted line represents the dispersion relation of light in vacuum, the parallel red dashed line represents the characteristic surface plasmon frequency at  $\omega_s = \frac{\omega_p}{\sqrt{2}}$ .



## 2.2.2 Excitation of surface plasmon polaritons by light

The hybrid of light with surface plasmons propagating along metal/dielectric interfaces is called surface plasmon polaritons (SPPs)<sup>[12]</sup>. As indicated in Fig. 2.2 (b), the wave vectors of the SPPs are higher than the wave vectors of light in vacuum for any given frequency. Due to the insufficient wave vector of light, direct excitation of the SPPs by light at a planar metal/vacuum interface is impossible. Increase of the wave vector of light can be achieved by different approaches, for example, grating couplers (structured and roughened metal surfaces) and prism couplers (e.g., the Otto configuration<sup>[10]</sup> and the Kretschmann-Raether configuration<sup>[11]</sup>). The excitation of surface plasmon polaritons by light has been described in detail, e.g., in these references<sup>[1, 12]</sup>.

## 2.2.3 Excitation of propagating surface plasmons by electrons

As mentioned above, momentum conservation techniques are needed for excitation of propagating surface plasmons at a planar metal/vacuum interface by light as well as in turn for the decay of the propagating surface plasmons into light. Due to the fact that non-relativistic free electrons have a much higher momentum than the visible light<sup>[72]</sup>, propagating surface plasmons at the metal/vacuum interface can be directly excited by impact of electrons, as theoretically predicted by Ritchie<sup>[2]</sup>. Powell and Sam reflected high energy electrons at an Al foil surface and the measured electron energy losses were characteristically at 15eV and 10.6eV<sup>[3]</sup>. They were ascribed to the excitation of bulk plasmons and surface plasmons by electrons. As sketched in Fig. 2.3, the impinging electrons are scattered by the free electrons of a metal target. They transfer a small fraction  $\Delta E$  of the initial energy  $E$  and a momentum  $\hbar\mathbf{q}$  to the sea of the free electrons of the metal, which excite collective oscillations of the bulk electrons and the surface electrons. The transferred momentum  $\hbar\mathbf{q}$  is given by equation 2.9<sup>[69, 73]</sup>:

$$\mathbf{q} = \mathbf{k}_e \sqrt{\theta^2 + \theta_{\Delta E}^2}, \quad \text{with } \theta_{\Delta E} = \frac{\Delta E}{2E}. \quad (2.9)$$

Where  $\mathbf{k}_e$  is the wave vector of the impinging electrons,  $\theta$  is the scattering angle of the impinging electrons. Since the energy loss  $\Delta E$  is very small in comparison with the initial energy  $E$  of the impinging electrons,  $\theta_{\Delta E}$  is much smaller than the scattering angle  $\theta$  of the impinging electrons<sup>[69]</sup>. The transferred momentum  $\hbar\mathbf{q}$  is approximately equal to  $\hbar\mathbf{k}_e \cdot \theta$ . The transferred wave vector  $\mathbf{q}$  is nearly perpendicular to the wave vector of the impinging electrons  $\mathbf{k}_e$ <sup>[69, 73]</sup>, thus the component of the wave vector  $\mathbf{q}$  at the interface  $\mathbf{k}_x$  is approximately equal to  $\mathbf{q}$  and therefore proportional to the scattering angle  $\theta$ :  $\mathbf{k}_x \approx \mathbf{k}_e \cdot \theta$ . According to this relation, the dispersion relation  $\omega(\mathbf{k}_x)$  of surface plasmons can be determined by measurements of the energy losses at different scattering angles of the impinging electrons<sup>[69]</sup>.

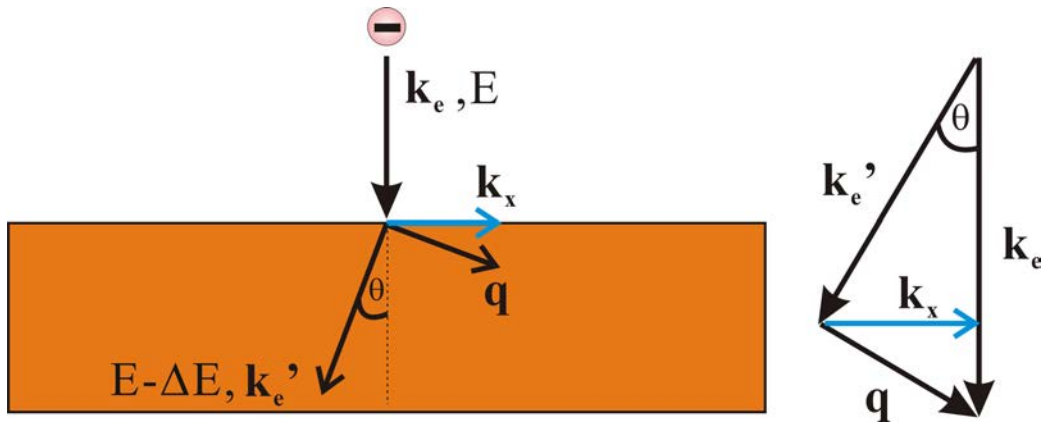


Fig. 2.3 Scheme of excitation of propagating surface plasmons by normally incident electrons, adopted from reference<sup>[69]</sup>; the incident electrons are scattered at various angles  $\theta$  by conduction electrons of a metal target and loss a small fraction energy  $\Delta E$  and a momentum  $\hbar\mathbf{q}$ .

The interaction between the impinging electrons and the free electrons of metals can also be understood as follows: the impinging electrons, moving along a straight trajectory with a uniform velocity  $\mathbf{V}$ , establish an electromagnetic field on a polarized metal surface, which acts against the impinging electrons and causes the energy losses of the impinging electrons<sup>[69]</sup>. Calculations of the locally established electric field by the impinging electrons can reveal the locally resulting energy loss of the impinging

electrons and the corresponding energy gain of the collectively oscillating electrons<sup>[74]</sup>. Similarly, mapping the electron energy loss of the impinging electrons after penetration of metallic nanoparticles reveals the distribution of the surface electric field upon excitation of surface plasmons<sup>[34, 36]</sup>.

In addition to the excitation of surface plasmons by high energy electrons in a scanning electron microscope or in a scanning transmission microscope, surface plasmons can also be excited by low energy electrons, e.g., electrons with a few eV, inelastically tunneling in a scanning tunneling microscope (STM), where gap plasmons are induced inside a tip-sample cavity by inelastically tunneling electrons<sup>[75]</sup>. The gap plasmons may directly decay into light or into propagating surface plasmons. The leakage radiation at the metallic film/dielectric interface due to the decay of the excited propagating surface plasmons in an STM was observed. The leakage radiation was emitted at specific emission angles, fulfilling the Kretschmann's relation of  $K_{spp} = (n\omega \sin\theta_L)/c$ <sup>[72, 76, 77]</sup> ( $K_{spp}$  is the wave vector of propagating surface plasmons,  $n$  is the refractive index of the dielectric,  $\omega/c$  is the wave vector of light,  $\theta_L$  is the emission angle). This demonstrates the generation of propagating surface plasmons by inelastically tunneling electrons. The detailed discussions about the excitation of surface plasmons by tunneling electrons in an STM and the resulting light emission can be found in chapter 7.

## 2.3 Localized surface plasmons

Unlike that surface plasmons propagating along a planar metal/dielectric interface, surface plasmons excited in curved surfaces, e.g., metallic nanoparticles and voids, are called localized surface plasmons<sup>[78]</sup>. For example, due to the excitation of localized surface plasmons on noble metal nanoparticles by light, the extinctions occur at the resonant frequencies of the excited localized surface plasmons, which are very sensitive to the size and the shape of the particles as well as their dielectric environment. Hence metallic nanoparticles exhibit various colors<sup>[79, 80]</sup>. Compared to propagating surface plasmons, localized surface plasmons are non-propagating modes

trapped on, e.g., nanoparticles and nanostructures. They can be excited by light directly or in turn effectively radiate light, regardless of the dispersion relation<sup>[78]</sup>. Since the energy of light can be concentrated into a very small volume via the nanostructures, the surface electromagnetic field is strongly amplified in the vicinity of the nanostructures upon the excitation of the localized surface plasmons<sup>[81, 82]</sup>. Such strongly amplified surface electric fields play an important role in surface enhanced spectroscopy<sup>[25]</sup>, e.g., surface enhanced Raman scattering (SERS)<sup>[21, 22]</sup>.

## 2.4 Optical properties of gold and silver

Fig. 2.4 shows the real and imaginary parts of the complex dielectric constants of Au and Ag in the wavelength range between 200nm and 1000nm. The data were calculated from the optical constants (n, k) of Au and Ag, which were obtained from the reference<sup>[83]</sup>. Since the absolute value of  $|\epsilon'(\lambda)|$  of Au and Ag is relatively large in the visible and the near infrared, in order to exhibit the part of the curves with relatively small values of  $|\epsilon'(\lambda)|$ , the real part  $\epsilon'(\lambda)$  of Au and Ag with wavelength longer than 600nm is divided by 10, as indicated in Fig. 2.4.

In the long wavelength range below the threshold of interband transitions from the d band to the sp band, which are 2.4eV for Au<sup>[84]</sup> and 4eV for Ag<sup>[84]</sup>, respectively, the Drude model is valid for the description of the optical response of Au and Ag<sup>[29, 85]</sup>. The frequency dependent dielectric constants of Au and Ag follow equation 2.7 in this wavelength range. Due to the effects of interband transitions, the frequency dependent dielectric constants of Au and Ag deviate from the Drude model in short wavelength range<sup>[29]</sup>. In the case of Ag, the imaginary part  $\epsilon''_{Ag}(\lambda)$  rapidly increases when the energy slightly exceeds the threshold of interband transitions of 4eV. The bulk plasmon energy of Ag is 3.75eV (about 330nm)<sup>[86]</sup>, where the real part  $\epsilon'_{Ag}(330\text{nm})$  is equal to 0 and the imaginary part  $\epsilon''_{Ag}(330\text{nm})$  is close to 0, following the prediction of the equation 2.7. Thus, Ag can be regarded as a free electron metal and the effects

of the interband transitions can be neglected when the wavelength longer than 330nm. The characteristic surface plasmon energy of Ag is 3.65eV (340nm) in vacuum<sup>[87]</sup>. At this wavelength the requirement of  $\epsilon'_{\text{Ag}}(\lambda) + \epsilon_d = 0$  is fulfilled<sup>[29]</sup> (where  $\epsilon_d$  represents the dielectric constant of a dielectric medium, which is equal to 1 in vacuum). As shown in Fig. 2.4, the imaginary part  $\epsilon''_{\text{Ag}}(\lambda)$  has a minimum at its bulk plasmon energy and slightly increases with increasing wavelength. Due to the low imaginary part of Ag and the resulting very low dielectric losses, the excited bulk plasmons of Ag mainly decay into light. As a consequence, an intense and narrow peak at 330nm was observed in the cathodoluminescence spectra from, flat Ag films<sup>[86]</sup> and Ag foils<sup>[88]</sup>. More details can be found in chapter 5 where the cathodoluminescence of Ag is fully discussed. Additionally, due to the relatively low imaginary part of Ag over the near UV to near infrared (IR) spectral range, Ag is a very important material for supporting surface plasmons to achieve high surface electromagnetic field enhancements, e.g., for surface enhance Raman spectroscopy<sup>[89]</sup> and tip-enhanced Raman spectroscopy<sup>[90]</sup>.

For gold, due to the occurrence of interband transitions in the short wavelength range (shorter than 520nm), the real part of the dielectric constants of gold  $\epsilon'_{\text{Au}}(\lambda)$  significantly deviates from the prediction of the Drude model and  $\epsilon'_{\text{Au}}(\lambda)$  varies around -1 over a wide wavelength range. The imaginary part of the dielectric constants  $\epsilon''_{\text{Au}}(\lambda)$  is high in this wavelength region. Since the reported bulk plasmon energy of Au ranging from 4.4eV to 9eV<sup>[84]</sup> is much higher than the threshold of interband transitions of 2.4eV, the excited bulk plasmons of gold are expected to efficiently be damped by generation of electron-hole pairs<sup>[29]</sup>. The surface plasmon energy of gold was determined to be 2.58eV (480nm)<sup>[91]</sup> in vacuum. Due to interband transitions and the strong internal damping at energies above 2.4eV, excitation of surface plasmons on gold rarely occurs in the short wavelength range. In contrast, the imaginary part of the dielectric constants of Au is low in the long wavelength range with a minimum at about 650nm. Therefore, Au is an interesting material for

sustaining surface plasmons in the visible and near-infrared spectral range<sup>[84]</sup>.

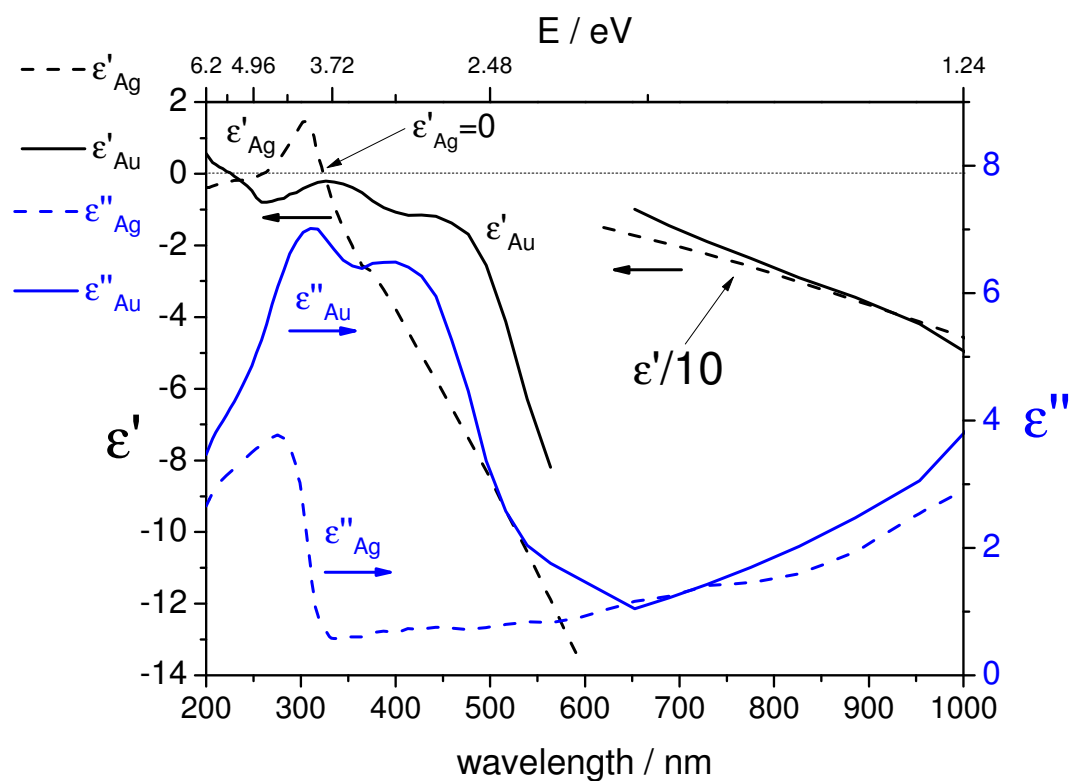


Fig. 2.4 The real and imaginary parts of the complex dielectric constants of gold (solid curve) and silver (dashed curve) in the wavelength range between 200nm and 1000nm, calculated from the optical constants of gold and silver, which were obtained from the reference<sup>[83]</sup>.

# Chapter 3 Experimental details

## 3.1 Chemicals

LiCl, analytical grade, water content < 0.5%, Merck;

HClO<sub>4</sub>, 70%, analytical grade, Merck;

Dimethyl sulfoxide (DMSO), water content < 0.05%, Merck;

Ultra-pure water, Sartorius Arium;

NaOH, analytical grade, Merck;

Au foil, 0.1mm thick, 99.999%, Wieland;

Au wire,  $\phi$  1mm, 99.999%, Wieland; Au wire,  $\phi$  0.25mm, 99.999%, Wieland;

Ag wire,  $\phi$  0.25mm, 99.9985%, Alfa Aesar;

Carbon fiber,  $\phi$  7 $\mu$ m, Goodfellow.

## 3.2 Electrochemical micromachining set-up<sup>[42, 43]</sup>

Fig. 3.1 (a) shows the scheme of the electrochemical micromachining set-up based on the application of ultra-short voltage pulses. It is a typical four electrodes system, as it is also used in, e.g., scanning electrochemical microscopy (SECM) or electrochemical scanning tunneling microscopy (ECSTM). The potential of reference electrode, counter electrode and two working electrodes (here tool and workpiece) are controlled by a home-built bi-potentiostat in an electrochemical cell. A high frequency voltage pulse train, generated by a pulse generator, is applied to the tool via a high frequency preamplifier. The potentials of the tool and the workpiece are rapidly perturbed by the pulses with respect to their rest potentials, which are controlled by the bipotentiostat. A photograph of the experimental set-up, which we use for electrochemical micromachining of gold, is shown in Fig. 3.1 (b). An electrochemical cell made of KEL-F was assembled and mounted on a Piezo-driven XYZ stage (P-562 XYZ Nanopositioning system, Physik Instrumente). The tool electrode was connected to

the high frequency preamplifier by a sheet of Cu foil coated with a thin Au film. Pulses generated by a HP 8130A (300MHz) pulse generator are amplified by a factor of 3.12 by the high frequency preamplifier before application to the tool electrode. The preamplifier was mounted close to the tool electrode to avoid pulse distortion due to the use of long cables. The pulse train and the corresponding high frequency current flowing across the tool electrode upon application of the pulses are simultaneously monitored by a Tektronix TDS 3054 oscilloscope (500MHz). A home built computer based bipotentiostat programmed by Labview 6.0 via a National Instruments (NI) DAQcard of PCI6052E, is used to control the rest potentials of the tool electrode and the workpiece electrode.

The manipulator, i.e., P-562 XYZ Piezo-nanopositioning system (Physik Instrumente, PI), sitting beneath the electrochemical cell, has a  $200\mu\text{m} \times 200\mu\text{m} \times 200\mu\text{m}$  closed-loop travel ranges with a 1nm closed-loop resolution (specification obtained from Physik Instrumente, PI). It is controlled by an E-516 modular piezo controller unit (PI), which has a RS232 and a GPIB interface. Herein, we use the GPIB interface to communicate with the controller unit to achieve programmable movement of the electrochemical cell by the Labview program. The movement, such as speed, length per step and directions, can be controlled easily by the Labview program.

In order to determine the starting position for machining, the tool first approaches to the workpiece surface without application of pulses until it contacts the workpiece. Then the tool is withdrawn a few micrometers and this position is set to be the starting position. The approach of the tool electrode to the workpiece is monitored via the current flowing between the tool and the workpiece. When the tool contacts the workpiece, the current suddenly increases. If the current exceeds a given threshold, the tool is slightly retracted until the current is less than the threshold. The contact detection should be set to be very sensitive to avoid strong deformation of the tool upon contact. During the machining process, due to the high charging current flowing between the tool and the workpiece, the detection sensitivity must decrease, but it is still sensitive enough to detect the electrical contact. The rest potential of the workpiece would be disturbed upon the electrical contact with the tool, which leads to



a wide range corrosion of the workpiece. For our experimental set-up, the sensitivity of the contact measurement and the response of the following withdraw of the tool are good enough to avoid the wide range corrosion.

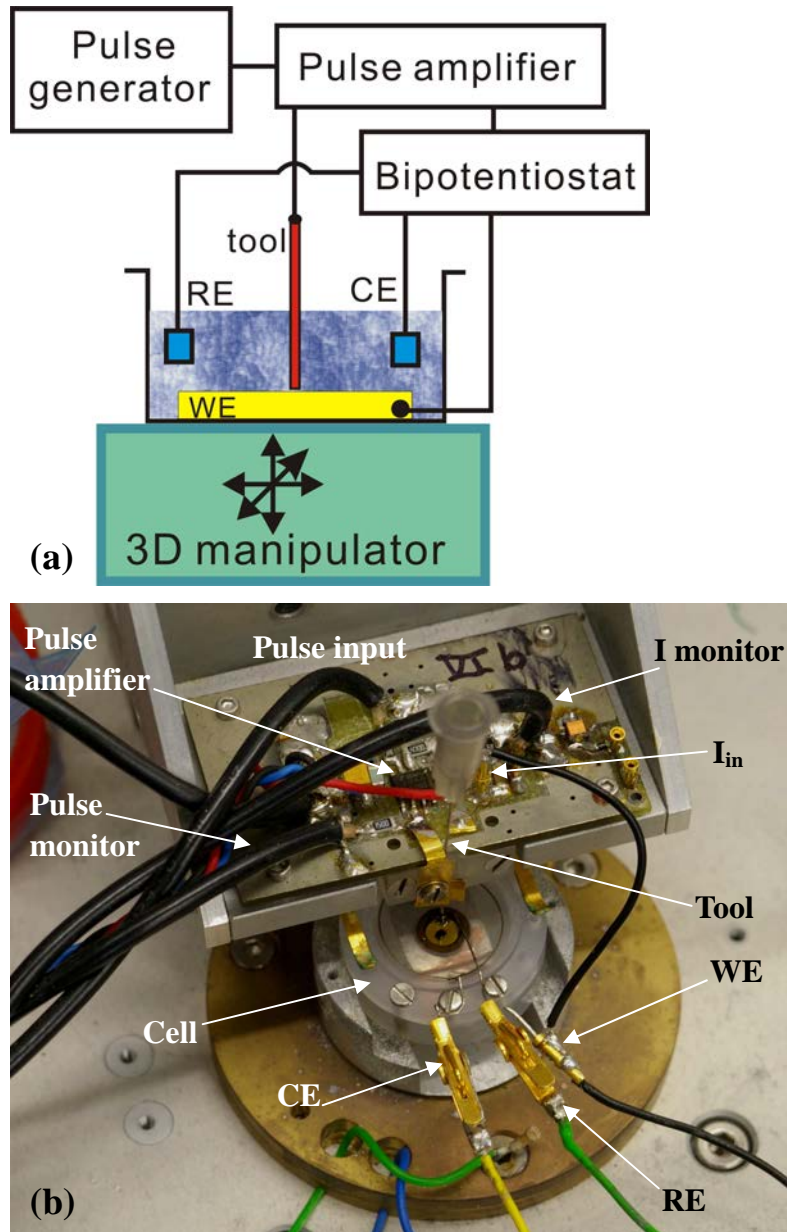


Fig. 3.1 (a) Scheme of the electrochemical micromachining set-up; (b) Photograph of the electrochemical micromachining set-up.

### 3.3 Measurement of the differential capacitance

AC voltammetry is a common method for measurement of the differential capacitance of a solid electrode<sup>[45]</sup>. In our experiments, the polarization of the electrode to be measured is controlled by a home-built potentiostat. An EG&G model 5210 Lock-in amplifier is coupled to the home-built potentiostat to simultaneously detect the in-phase and 90°-phase shifted ac components of the cell current upon potential modulation with a 5mV, 25Hz sine wave. The detected in-phase and 90°-phase shifted ac components are recorded and stored by a personal computer via a NI PCI 6251 DAQcard. From those signals the differential capacitance of the electrode can be calculated<sup>[45]</sup>. The differential capacitance of a gold electrode in LiCl/DMSO will be discussed in chapter 5.

### 3.4 Light collection and detection for cathodoluminescence experiments

#### 3.4.1 Light collection with optical fibers

The first method we tried for cathodoluminescence experiments was collecting and guiding emitted light with multi-optical fibers which were placed in the vicinity of the specimen, similar to Hoenk and Vahala's set-up<sup>[92]</sup>. Optical fibers can easily guide the light to the detectors since the optical path is flexible. Thus the set-up was quite simple. We chose low OH multimode optical fibers (Thorlabs) with a transmission spectral ranged from 400nm to 2200nm, whose core diameter was 1.0mm and the numeric aperture was 0.48. The front faces of the fibers were flatted and polished with 7 $\mu$ m, 3 $\mu$ m and 1 $\mu$ m diamond paste before fixing inside the SEM chamber. As shown in Fig. 3.2, six optical fibers were mounted around the electron beam irradiation area. The angle between the incidence of electron beam and the axis of the fiber was about 60°. Dependent on the distance from the front face of the optical fibers to the electron irradiation area, the collection solid angle of these six optical fibers was estimated to

be about  $0.24\pi$  and the corresponding collection efficiency was about 12% for an isotropic light source. The parts of the fibers close to the electron beam irradiation area were protected by aluminum foils to avoid charging by electrons. The fibers penetrated the wall of the vacuum chamber via a home-made feedthrough. The other ends of the fibers were mounted in front of the cathode of a photomultiplier or the entrance slit of a monochromator.

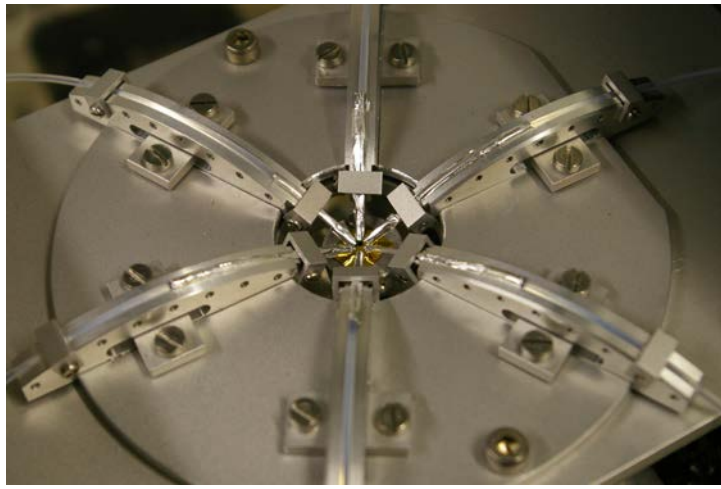


Fig. 3.2 Photograph of multi-optical fibers placed in the vicinity of a specimen inside the scanning electron microscope chamber.

Though the collection optics based on the optical fibers was easy to construct and the light could be easily guided to the detector, fatal shortcomings, which were not expected until the optical fibers were mounted inside the SEM chamber, were the influence of the backscattered electrons and the charging of the front faces of the fibers. The accumulated charges on the front faces of the fibers repelled the low energy secondary electrons, which decreased the brightness and the contrast of the secondary electron images. Extremely, the electric field resulted from the accumulated charges on the front faces of the fibers even affected the scanning of the high energy primary electron beam and led to distortions of the secondary electron (SE) images. A strongly distorted SE image of a gold micro-column array is shown in Fig. 3.3. The image was recorded with an externally controlled electron beam slowly scanning across the gold column array with a rate of 10ms/pixel. Light generated by the

backscattered electrons at the front faces of the fibers was another unacceptable effect. The evidence for the generation of light by backscattered electrons is shown in Fig. 3.4. The depicted spectra were obtained from Au, Si and Al samples upon bombardment with 20keV electrons. All spectra show a peak at 450nm, which is almost independent of the material of samples except the intensity. The intensity of the peak is correlated with the efficiency of backscattering of electrons. Au has the highest backscattering efficiency among those three materials because of its highest atomic number, whereas Al has the lowest backscattering efficiency, which led to the lowest intensity. Influences of the charging on the photon maps were also observed. Fig. 3.5 shows a photon map recorded with the fiber setup. The electron beam slowly scanned across the structure from the lower part of the image to the upper part. The intensity decreased with increase of the scanning time. This can be understood by the ongoing accumulation of charges on the front face of the fibers during recording the image. At the beginning of the scanning, due to the rather low accumulated charges, the backscattered electrons felt small repelling forces, which bombarded the front faces of the fibers and led to high intensity. With progressing scanning the accumulated charges increased and this led to lower intensity in the upper part of Fig. 3.5. During successive scans, the accumulated charges reached an equilibrium value and the intensity of the photon maps became independent of the scanning time. Very high intensity sparks were occasionally observed in the photon maps which were attributed to the discharging of high density surface charges on the front faces of the fibers. Negatively biasing of the fibers by application of a voltage of 3000V, in order to repel the incidence of the backscattered electrons, decreased the intensity, which gave a further evidence of the influence of the backscattered electrons. The unacceptable light generated by the backscattered electrons and the unwanted surface charging of the optical fibers were the reasons for giving up this approach and going to a collection optics employing an Al parabolic mirror. However, though the multi-fiber light collection stage can not be used in the SEM, it might be modified for light collection in scanning tunneling microscope induced light emission experiments.

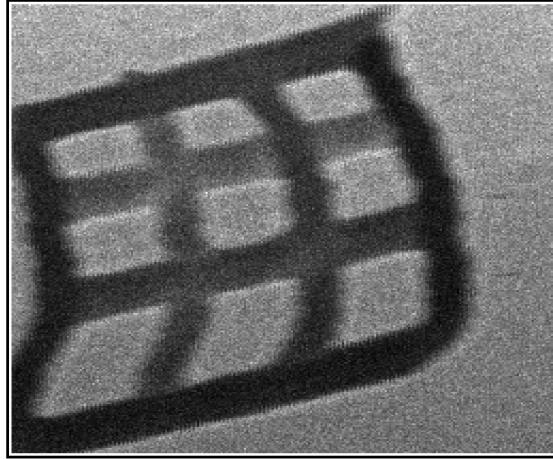


Fig. 3.3 Distorted secondary electron image upon the accumulated charges on the front surfaces of the optical fibers.

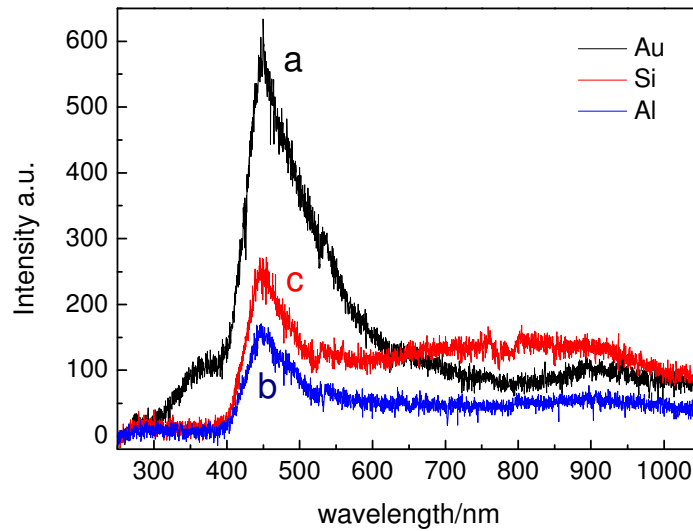


Fig. 3.4 Cathodoluminescence (CL) spectra collected with the multi-optical fibers, (a) from an Au film, (b) from an Al foil and (c) from a Si substrate upon irradiation with 20keV electrons.

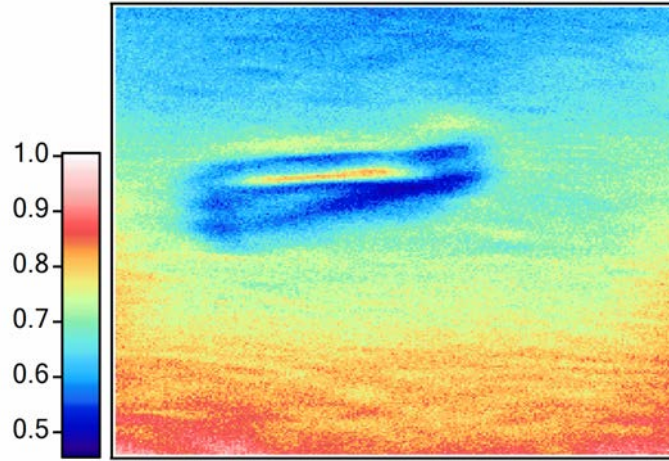


Fig. 3.5 Panchromatic CL image using the multi-fibers for light collection; the maximum intensity (3000 counts per 10ms) was normalized to 1.

### 3.4.2 Light collection with a parabolic mirror

An aluminum parabolic mirror manufactured from bulk aluminum by Linos Optics is used as a light collection element mounted inside a scanning electron microscope chamber, as shown in Fig. 3.7 (b). Fig. 3.6 shows a scheme of the geometry of the parabolic mirror. The focal length of the parabolic mirror is 2mm. The shape of the parabolic mirror is obtained by the curve of  $z^2=8(y+2\text{mm})$  rotating about the y-axis on the  $z>0$  half hemisphere. The surface of the parabolic mirror is described by the equation of  $x^2+z^2=8(y+2\text{mm})$ . The mirror is 7.5mm high and 15mm wide. There is a 1mm diameter hole drilled through the mirror along the z-axis for the passage of electrons. The hole cuts off the zenith angle  $\theta$  below  $7^\circ$ . The details can be found in chapter 5.

The angles from the focal point to the edges of the mirror in the y-z plane with respect to the surface normal are indicated in Fig. 3.6. The solid angle of our parabolic mirror can be estimated by equation 3.1:

$$\Omega = \int_0^\pi d\varphi \int_\pi^{0.29\pi} \sin \theta d\theta \quad (3.1)$$

$$\approx 1.6\pi.$$

In this equation,  $\theta$  is the zenith angle towards the rotational symmetry axis (y-axis in Fig. 3.6) and  $\varphi$  is the azimuthal angle, lying in the x-z plane of Fig. 3.6. The above

calculation disregards the small separation of 0.5mm between the specimen (focal point) and the mirror, which would slightly reduce the azimuthal integration interval and become dependent on the zenith angle  $\theta$ . We approximated the error to be of the order of  $0.1\pi$ . Thus the solid angle of the parabolic mirror is approximated to be  $1.6\pi$  and 80% of the emitted light can be collected if a light source is isotropic.

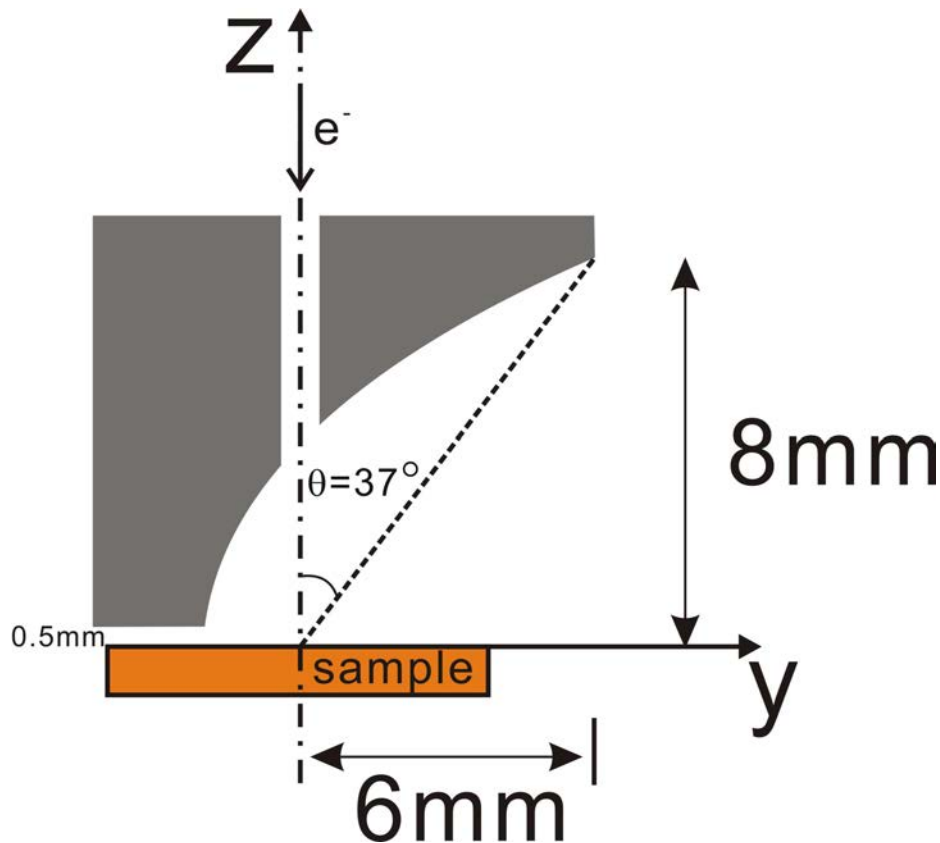


Fig. 3.6 Scheme of the geometry of the parabolic mirror in the y-z plane.

A parabolic mirror can focus a perfectly parallel beam along its optical axis into a tightly focused point; in turn a point light source at the focal point of a parabolic mirror will be converted to a perfectly parallel beam along its optical axis. A beam would deviate a few degrees off the optical axis if the point source shifts a few micrometers from the focal point of the parabolic mirror. Thus, the output of the parabolic mirror is very sensitive to the position of the light source with respect to the focal point of the parabolic mirror. As sketched in Fig. 3.7 (a), there is a  $\phi$  20mm optical window on the vacuum chamber of an SEM for passage of the parallel beam. The diameter of the optical window is slightly bigger than the cross section of the

parallel beam. Thus, the electron beam irradiated area where the light generated should be perfectly at the focal point of the mirror. Otherwise, the output beam shifts significantly off the optical axis and would be blocked by the wall of the vacuum chamber. This would significantly decrease the collection efficiency of the parabolic mirror (see discussion below).

For our experimental set-up, the mirror is attached to a three dimensional micromanipulator for adjustment of its positions from outside of the SEM chamber and it is placed 0.5mm above a specimen, as shown in Fig. 3.7 (b). Light generated at the focus point of the mirror upon electron beam bombardment is reflected by the mirror into a parallel beam. The parallel beam passes through a fused silica viewport (ordered from Allectra). Then it is reflected either by a switch-able aluminum mirror (Edmund Optics) to the cathode of a photomultiplier or is focused by a fused silica Plano convex lens (Thorlabs,  $f=100\text{mm}$ , aperture: 4.0) onto the entrance slit of a monochromator or onto a CCD camera. The material of the lens has to be chosen with care. At the beginning, a convex lens made of BK7 was used which strongly absorbed light with wavelength shorter than 350nm and the generated fluorescent light peaked at 380nm. This problem was solved by replacing the BK7 convex lens with the fused silica lens. Because the parabolic mirror is about 400mm away from the convex lens or from the photomultiplier, the parallel beam should not deviate larger than  $0.7^\circ$  from the optical axis in order to avoid hitting the wall of the tube which holds the mirror (see Fig. 3.7 b). Hence adjusting the mirror in three dimensions, in order to place the electron beam irradiation area perfectly at the focal point of the mirror is a critical issue for the parabolic mirror light collection optics. At the beginning, after the installation of the parabolic mirror inside the SEM, when the CCD camera was not available, the adjustment of the mirror position was very difficult. For a rough adjustment, light from a LED passed through a  $\phi 20\mu\text{m}$  aperture was used as a 'point' source. The  $\phi 20\mu\text{m}$  aperture was placed beneath the mirror. Then the position of the mirror and the position of the  $\phi 20\mu\text{m}$  aperture were roughly adjusted with the help of the SEM image to make sure that the electron beam passed through the hole in the parabolic mirror onto the center of the aperture. Afterwards the SEM was turned off



and the aperture was illuminated with the LED. Outside the vacuum chamber, the beam reflected by the parabolic mirror was observed by a telescope focused to infinity. Then the position of the parabolic mirror was adjusted until the brightest possible point was observed. Actually, the 20 $\mu$ m diameter light source was not a point source and the above procedure was only sufficient for a rough adjustment. The adjustment procedure became easier after using a CCD camera (Watec, model: WAT-525EXA), which was mounted behind the convex lens, replaced the slit of the monochromator. The light emitted from a nanometer area upon irradiation of a sample with a stationary electron beam was focused into the smallest and brightest possible spot by adjustment of the mirror. Then the electron beam irradiated area was on the focal point of the mirror.

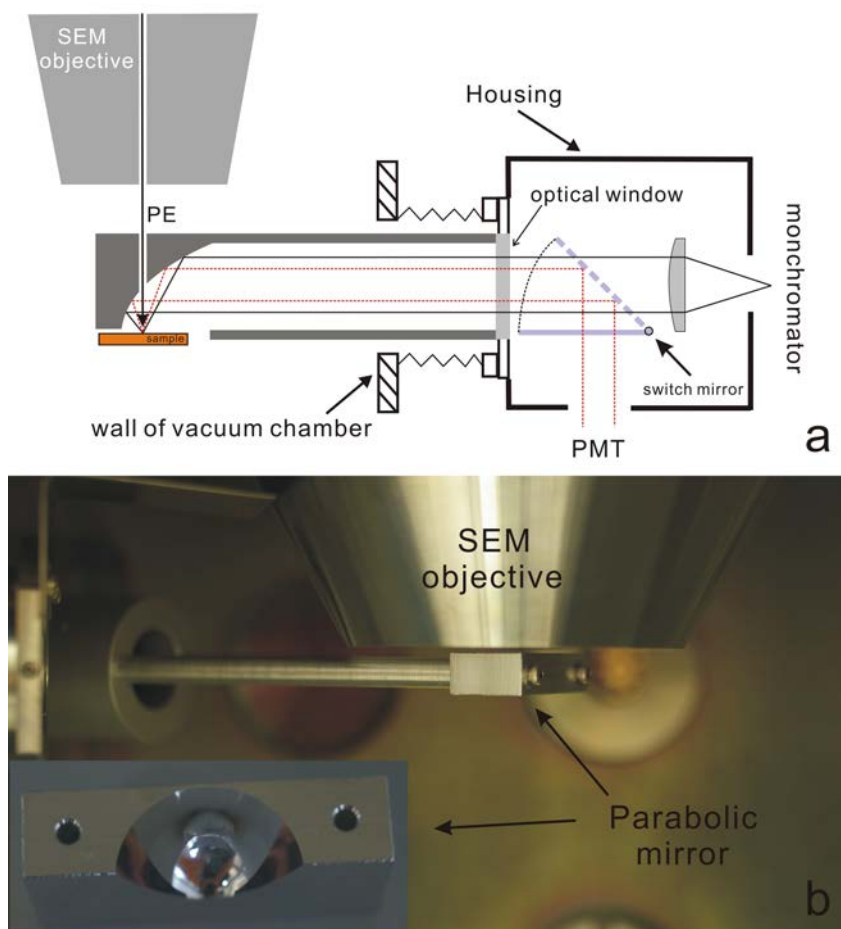


Fig. 3.7 (a) Scheme of the parabolic mirror based optical setup for light collection in cathodoluminescence measurements; and (b) photograph of the parabolic mirror placed inside the SEM chamber.

### 3.4.3 Detection of low light levels and photon counting

Due to their high sensitivity and stability, photomultiplier tubes (PMT) are widely used for the detection of weak light<sup>[93]</sup>. The photomultiplier converts light into electric signals and its spectral response is dependent on the cathode materials. Photoelectrons generated at the cathode of the photomultiplier by light are accelerated and amplified by a series of dynodes. The amplified photoelectrons reach the last anode of the photomultiplier and are detected as charge pulses. The charge pulses generated by very weak light can be counted since the pulse to pulse intervals are wide enough in comparison with the response time of the photomultipliers. The number of the charge pulses is proportional to the intensity of the incident light<sup>[94]</sup>. In our experiments, a model R649 photomultiplier tube is used to count single photons. The cathode of the R649 PMT is sensitive from 300nm to the near infrared at 850nm with maximum response at 420nm. A scheme of our photon counting system is shown in Fig. 3.8. The output of charge pulses from the anode of the photomultiplier are amplified by a fast preamplifier (model 9301, ORTEC), mounted close to the photomultiplier. The amplified charge pulses are fed into a model 9302 Amplifier Discriminator (ORTEC). Most of background noise pulses are eliminated by the discriminator via adjustment of the reference level. The photomultiplier is usually operated at room temperature and the dark count rate is about 600 counts per second, which can be neglected in comparison with the emitted light. The pulses from the amplifier/discriminator are counted by a counter (model 9315, ORTEC) and a NI PCI6251 DAQcard. In order to record the surface geometry simultaneously with the emitted light intensity, scanning of an electron beam of the SEM (Hitachi S570) is externally controlled by the NI PCI6251 DAQcard via an IgorPro program. The electron beam is slowly scanned with typical dwell times of 5-10ms/pixel. The secondary electron (SE) and the cathodoluminescence upon bombardment with the primary electron beam are recorded simultaneously. Simultaneously recorded SE images and CL images are typically 256 pixel x 256 pixel wide.

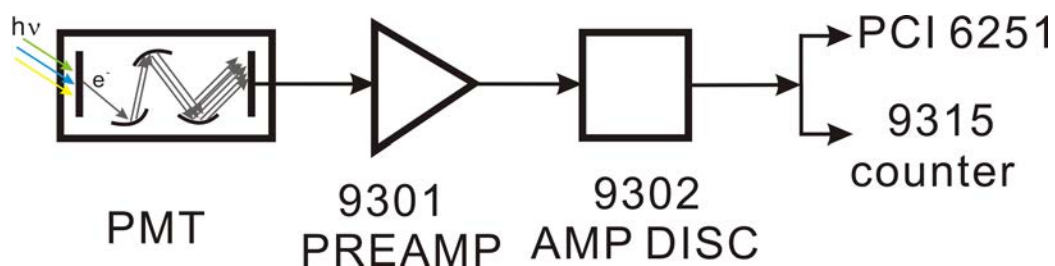


Fig. 3.8 Scheme of the photon counting system.

### 3.4.4 Spectrally resolved measurements

The wavelength distribution of the emitted light upon irradiation with the electron beam is measured with a Czerny-Turner type monochromator (Jobin Yvon, model Triax320). Fig. 3.9 shows the working principle of the Czerny-Turner configuration monochromator. Light from the entrance slit, which is placed at the focal point of a collimation mirror, is collimated. The collimated light beam is diffracted and dispersed by a grating, which can be rotated. The dispersed light is refocused by a focus mirror onto the exit slit plane. Light with different wavelengths is focused onto different positions of the exit slit plane. Due to the finite width of the exit slit, only light with a small wavelength interval can pass through the exit slit to the detector. The bandwidth of the light passing through the exit slit is dependent on the width of the exit slit and the grooves density of the grating<sup>[95]</sup>. By rotating the grating, the whole spectral range of interest can be scanned across the detector. The resolution of the monochromator is dependent on the length of optical path inside the monochromator, the width of the entrance slits and the grooves density of the grating<sup>[93]</sup>. The model Triax320 monochromator has a 320mm focal length and an aperture of  $f=4.1$ . It is fully automatically controlled by the Spectra Max 32 program. The exit slit in Fig. 3.9 is replaced by a liquid nitrogen cooled CCD (Spectrum one CCD) detector, which allows simultaneous recording of a spectral range of about 250nm width. The complete spectra, which typically range from 250nm to 1000nm, are recorded in three parts by rotation of a 300 grooves/mm grating. Light collected by the multi-optical fibers is guided to the monochromator by directly placing one end

of the fibers in front of the entrance slit of the monochromator; Light collected by the parabolic mirror is focused to the entrance slit of the monochromator by the Plano convex lens (Fig. 3.7). The numerical aperture (NA) of the convex lens is almost the same as the entrance slit aperture of the monochromator of  $f=4$ . Though the focusing of the emitted light into the brightest point is a perfect way for adjusting the position of the parabolic mirror, usually this mirror position is not the position for achieving maximum intensity with the monochromator. In order to find out the optimum mirror position for spectral measurements, we usually turn the mirror position carefully during electron beam irradiation of an electrochemically roughened gold substrate to achieve a maximum intensity. The focal length, i.e., the working distance of the SEM is monitored via the current through the objective lens of the SEM with a precision better than  $1\mu\text{m}$ . Hence, after exchanging of specimen, the exact focal point can be recovered by mechanically adjusting the position of the sample with the manipulator of the SEM for maximum sharpness of the SEM image.

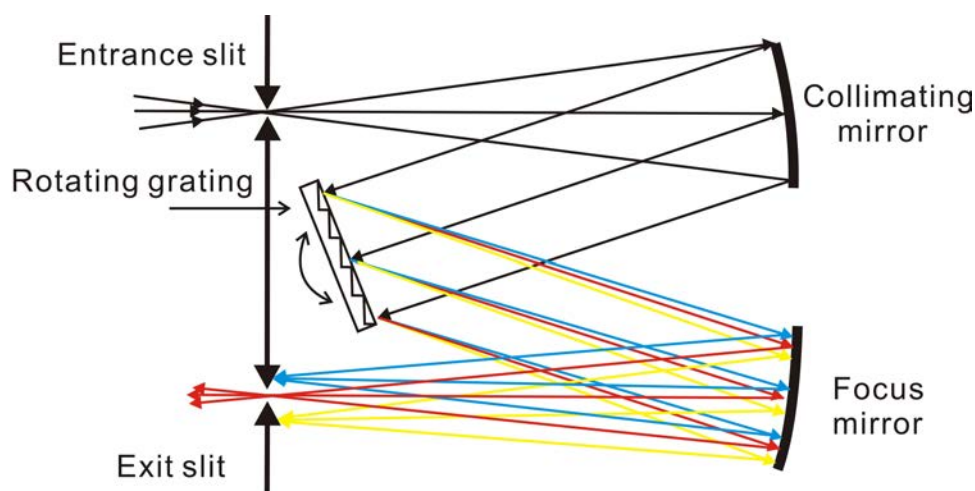


Fig. 3.9 Scheme of a Czerny-Turner type monochromator.

### 3.4.5 Angular intensity distribution measurements

As sketched in Fig. 3.10, light emitted from the focal point of the parabolic mirror with various emission angles is collimated and then re-focused by a convex lens. A CCD chip is placed about 35mm behind the focus plane of the convex lens to record the profile of the light. Light leaving the focal point with different directions will be imaged onto different positions of the CCD chip. In principle, the collimated light beam can be directly projected onto the CCD chip and no convex lens is necessary. However, the integration time has to be long enough for this case to record an intense cross section, due to the relatively low emission intensity. Using the convex lens, the light beam is concentrated onto the CCD chip. The ratio of the light beam cross section and the projected profile, in other word the magnification, is dependent on the position of the CCD chip from the lens. In order to eliminate the effect of CCD position on the size of projected profiles, the convex lens could be replaced by a beam extender in the future. In order to record the emission profile easily, a commercial digital camera is used (Pentax K100D) in our experiments, whose CCD chip is about 23.5mm x 15.7mm. The exposure time can be as long as a few 10s and the lowest ISO is 200. Though it is an un-cooled CCD chip, the dark noise is considerably low for a few 10s exposure. The angular intensity distribution of the emitted light revealed from the projected images will be discussed in detail in chapter 5, where the correlation between the emission angle and the projected position will be calculated. The similar angularly resolved method was published by Coenen et al. recently<sup>[96]</sup>. Similarly, using a small movable aperture, the angular intensity distribution of light reflected by a parabolic mirror was also measured by Yamamoto et al. recently<sup>[97, 98]</sup>.

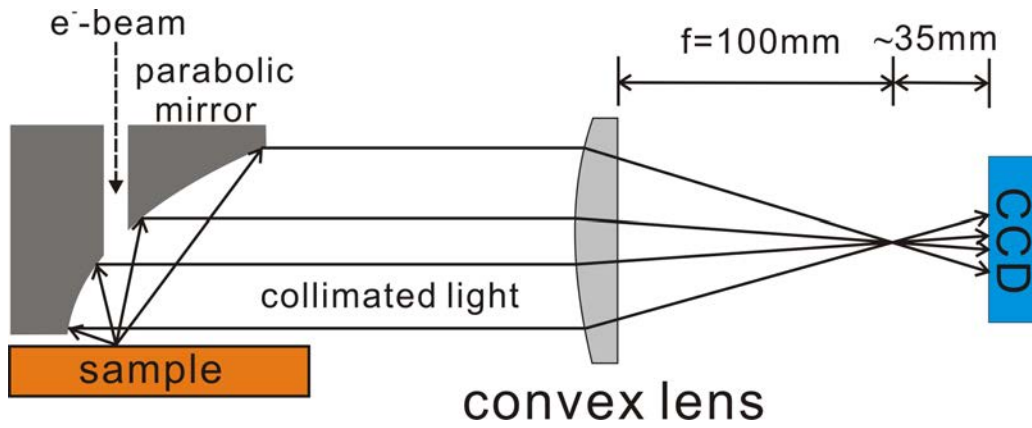


Fig. 3.10 Scheme of angular intensity distribution measurements.

# Chapter 4 Electrochemical machining of gold microstructures

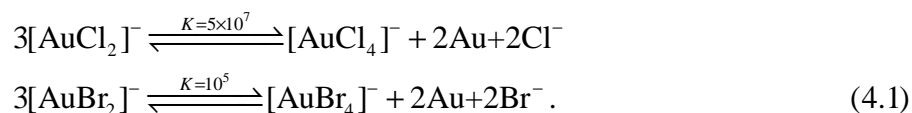
In this chapter, electrochemical machining of gold micro- and nanostructures in nonaqueous solutions, in our case of LiCl in dimethyl sulfoxide (DMSO), is described. First, the electrochemical behavior of gold in LiCl/DMSO and LiCl/DMSO-water mixtures is mainly investigated with cyclic voltammetry. Then the influence of machining parameters like pulse duration, pulse amplitude, rest potentials of gold workpieces and carbon fiber tools as well as water content in the solvent mixtures on the machining precision is studied by drilling holes with a well defined  $\phi$  7 $\mu$ m carbon fiber. The capabilities of machining complex gold micro- and nanostructures are demonstrated, too.

## 4.1 Electrochemical behavior of gold in different solutions

### 4.1.1 Gold in aqueous chloride solutions

Gold is a noble metal, located in group 11 in the periodic table of elements. The common oxidation states of gold are Au(I) and Au(III). Au(I) has a  $5d^{10}$  valence electron configuration and Au(III) has a  $5d^8$  valence electron configuration. Both Au(I) and Au(III) would coordinate with various ligands, e.g., with  $Cl^-$ ,  $Br^-$ ,  $I^-$ ,  $CN^-$ ,  $SCN^-$ , and mainly exist as complexes in aqueous solutions. The standard electrode potentials of Au(I) complex/Au couples as well as Au(III) complex/Au couples and the stability constants of Au(I) and Au(III) complexes in aqueous solutions were summarized, e.g., in reference<sup>[99]</sup>. Both Au(I) and Au(III) are polarizable ions and usually coordinate with ligands through the softer end of the ligands.  $Cl^-$  is one of widely used ligands for Au(I) and Au(III) and hence the dissolution of gold in aqueous chloride solutions has been well studied<sup>[100, 101]</sup>. Both  $[AuCl_2]^-$  and  $[AuCl_4]^-$  complexes are produced in the

process of electrochemical dissolution of gold in aqueous chloride solutions. The coordination number of  $[\text{AuCl}_2]^-$  is two, which has a linear geometry<sup>[99]</sup>. The coordination number of  $[\text{AuCl}_4]^-$  is four and it has a square planar geometry<sup>[99]</sup>. Au(I) halide complexes are not as stable as Au(III) halide complexes in aqueous solutions. They tend to disproportionate into Au(III) complexes and Au, as expressed by equation 4.1<sup>[99]</sup>:



The disproportionation equilibrium constants in equation 4.1 are  $5 \times 10^7$  and  $10^5$  for  $[\text{AuCl}_2]^-$  and  $[\text{AuBr}_2]^-$ , respectively<sup>[99]</sup>. Hence, the main product of gold dissolution in aqueous chloride solutions is  $[\text{AuCl}_4]^-$ <sup>[100, 101]</sup>. The concentration of  $[\text{AuCl}_2]^-$  is dependent on the concentration of  $\text{Cl}^-$ . In contrast, Au(I) cyanide complex is much more stable in aqueous solutions than Au(I) halide complexes since the cyanide is a much stronger (softer) ligand. It only slightly disproportionates into the Au(III) cyanide complex with an equilibrium constant of  $10^{-25}$ <sup>[99]</sup>.

Although the dissolution of gold in aqueous chloride solutions was well investigated and understood. We studied the electrochemistry of gold in these solutions with our equipment for comparison with the electrochemistry of gold in nonaqueous chloride solutions, e.g., in LiCl/DMSO.

Fig. 4.1 shows cyclic voltammograms (CVs) of a polycrystalline gold foil in 1M LiCl aqueous solution. The cyclic voltammetry measurements were carried out with an Autolab potentiostat (PGSTAT 30), (CV-parameters: counter electrode (CE): Pt wire ring; reference electrode (RE): aqueous  $\text{Cl}^-/\text{AgCl}/\text{Ag}$  (sat. KCl), connected to the solutions via a salt bridge). The potential was scanned from open circuit potential (OCP=0.75V) positively towards 1.2V and reversed at 1.2V. In the first scanning cycle, gold started to dissolve at 0.85V and the anodic current rapidly increased with increasing potential. Small magnitudes of overpotential already resulted in large anodic current densities. This indicates a large exchange current density for gold dissolution in 1M LiCl aqueous solution. Only one anodic peak was observed in the process of gold dissolution. The number of transferred electrons per dissolved gold



atom  $n$  was determined to be  $2.67 \pm 0.05$  at a dissolution potential of 1.2V by chronocoulometric measurements and the determination of the subsequent weight loss of the gold electrode. This indicates that  $[\text{AuCl}_4]^-$  was the predominate product, corresponding to the anodic peak at about 1V in Fig. 4.1. Only one corresponding cathodic peak at 0.55V was observed in the reversal scan, indicating that the reduction of  $[\text{AuCl}_4]^-$  into Au proceeded probably in a one step process<sup>[100]</sup>. After the first cycle, the anodic peak shifted negatively about 50mV, which demonstrates the easier dissolution of the re-deposited gold. The cathodic peak also shifted negatively to 0.5V.

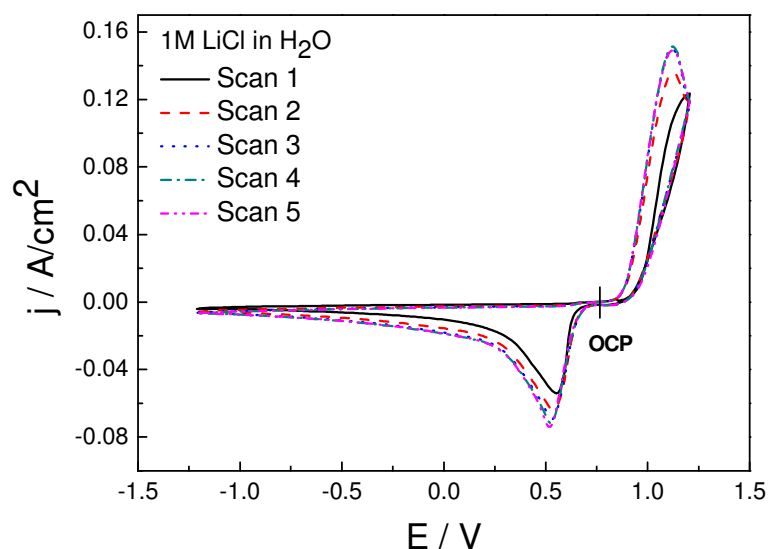


Fig. 4.1 Cyclic voltammograms of a polycrystalline gold foil in 1M LiCl aqueous solution. CV-parameters: CE: Pt wire; RE: aqueous  $\text{Cl}^-/\text{AgCl}/\text{Ag}$  (sat. KCl); scans:  $\text{OCP}=0.75\text{V} \rightarrow 1.2\text{V} \rightarrow -1.2\text{V} \rightarrow \text{OCP}$ , scan rate: 50mV/s.

#### 4.1.2 Gold in LiCl/DMSO solutions<sup>[102]</sup>

Solvent plays an important role in most chemical and electrochemical reactions<sup>[103]</sup>. For example, the stability of transition metal ions and their complexes changes from protic solvents to aprotic solvents, which is mainly dependent on the interactions between transition metal ions and the solvent molecules, as well as on the activities of the ligands in various solvents<sup>[103]</sup>. The relative stability of a given metal ion and its

complexes in various solvents can be reflected by the standard electrode potentials of the metal ion/metal couple and the complexes/metal couple<sup>[103, 104]</sup> in the different solvents, e.g., in water and in acetonitrile (AN). Persson reported that the standard electrode potential of  $\text{Au}^+/\text{Au}$  versus  $\text{H}^+/\text{H}_2$  (aqueous) was 1.83V in water and was 1.51V versus  $\text{H}^+/\text{H}_2$  (aqueous) in acetonitrile<sup>[104]</sup>. This shows that the free  $\text{Au}^+$  ion is more stable in acetonitrile than in water. The stability constants of various  $\text{Au}^+$  complexes in acetonitrile were summarized by Goolsby and Sawyer<sup>[105]</sup>.

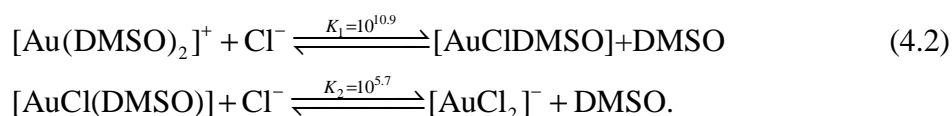
Similar to acetonitrile, dimethyl sulfoxide (DMSO) is another polar, aprotic solvent. DMSO is widely used, not only because of its high solubility capacity for various inorganic and organic materials and its chemical stability under alkaline, acidic and neutral conditions, but also for its compatibility with many container materials and its low toxicity for the users<sup>[106]</sup>. DMSO is highly polar (dipole moment:  $4.4\text{D}^{[103]}$ ) with a high dielectric constant of  $46.6\epsilon_0^{[103]}$ , which is slightly higher than the dielectric constant of acetonitrile ( $35.9\epsilon_0^{[103]}$ ). The high dielectric constant of DMSO is the reason for its high solubility power for various ionic salts. DMSO is also an important solvent in electrochemistry<sup>[107]</sup> because of its relatively wide electrochemical potential window. It is electrochemically stable from -4V to 1V vs. ferrocenium ion/ferrocene ( $\text{Fc}^+/\text{Fc}$ )<sup>[103]</sup>.

The electrochemistry and the stability of the Au(I) chloro complexes in DMSO have been studied with standard electrochemical methods, such as chronopotentiometry and potentiometric titration<sup>[108]</sup>. Little work, has been done on the dissolution of gold in DMSO chloride solutions<sup>[109]</sup>. In order to understand more about the electrochemical dissolution behavior of gold in LiCl/DMSO solutions for the determination of the electrochemical micromachining parameters, we investigated the reversible properties of dissolution and deposition processes of gold in LiCl/DMSO solutions with cyclic voltammetry. Solvent effects and the influence of the composition of DMSO-water mixtures on the electrochemistry of gold were also studied (see section 4.1.3).

Fig. 4.2 shows cyclic voltammograms of a polycrystalline Au foil in 1M LiCl/DMSO. An aqueous  $\text{Cl}^-/\text{AgCl}/\text{Ag}$  electrode was used as a reference electrode, connected to the

solution via a salt bridge. The potential was scanned from OCP at about 0.2V towards 1.2V and 1.8V, respectively. Gold started to dissolve at about 0.5V and the anodic current steeply increased with positively increasing potential. Considerable cathodic current was observed only below about -0.4V and a well defined cathodic peak was found at -0.75V. In order to identify the dissolved species of gold in LiCl/DMSO, chronocoulometric measurements and subsequent measurements of the weight loss of the gold electrode were performed to determine the number of transferred electrons per dissolved gold atom. The number  $n$  was determined to be  $0.99 \pm 0.03$  at both, 0.8V and 1.2V dissolution potentials. In DMSO, both, the free  $\text{Au}^+$  ions and the Au(I) chloro complexes were found to exist<sup>[105, 108]</sup> and all of them are relatively stable in DMSO with respect to aqueous solutions. Hence, the free  $\text{Au}^+$  ions and the  $[\text{AuCl}_m]^{(m-1)-}$  complexes are assigned to the possible dissolution products of gold when the potential was scanned up to 1.2V, which is in accordance with the results of Benari et al.<sup>[109]</sup>. However, the main dissolution products of gold among those Au(I) species need to be determined. The standard electrode potential of  $\text{Au}^+/\text{Au}$  is 1.21V vs.  $\text{H}^+/\text{H}_2$  (aqueous) in DMSO<sup>[104]</sup>, which is about -600mV more negative than the standard electrode potential of  $\text{Au}^+/\text{Au}$  in water. This points out that the free  $\text{Au}^+$  ion is thermodynamically stable in DMSO. The free  $\text{Au}^+$  ion can be solvated as  $[\text{Au}(\text{DMSO})_2]^+$  in  $\text{Cl}^-$  free DMSO solutions<sup>[105]</sup>. Although the free  $\text{Au}^+$  ion is thermodynamically stable in DMSO, however, according to Benari's investigations<sup>[109]</sup>, it was impossible to dissolve gold in  $\text{ClO}_4^-/\text{DMSO}$  solutions even upon the application of 1.85V vs. Ag/AgCl. This indicates the difficult formation of the free  $\text{Au}^+$  ions from gold dissolution in DMSO in the absence of strong coordination ligands, such as  $\text{Cl}^-$ . Hence, the free  $\text{Au}^+$  ions can be excluded as the main dissolution product of gold. Possibly, the  $[\text{AuCl}_m]^{(m-1)-}$  complexes were formed upon dissolution of gold in LiCl/DMSO. Only one well defined cathodic peak at -0.75V was observed in CVs after positively scanning up to 1.2V, implying that only one stable  $[\text{AuCl}_m]^{(m-1)-}$  complex species exists. This can indeed be substantiated by potentiometric titration experiments by Suarez et al.<sup>[108]</sup>. They studied the stability constants of  $[\text{AuCl}]$  formed from  $\text{Au}^+$  ions in DMSO and the subsequent formation of

$[\text{AuCl}_2]^-$ :



The formation constants  $K_1$  and  $K_2$  of  $[\text{AuCl}]$  and  $[\text{AuCl}_2]^-$  in DMSO are  $10^{10.9}$  and  $10^{5.7}$  [108].

Assuming that the concentration of  $\text{Cl}^-$  at gold surface was approximately maintained to be 1M during anodic dissolution, a ratio of  $[\text{AuCl}_2]^-/[\text{AuCl}]$  of about  $10^{5.7}$  and a ratio of  $[\text{AuCl}_2]^-/\text{Au}^+$  of about  $10^{16.6}$  would be resulted. For extremely fast dissolution, assuming that the concentration of  $\text{Cl}^-$  at the gold surface was two orders lower than the bulk concentration, the ratio of  $[\text{AuCl}_2]^-/[\text{AuCl}]$  would be about  $10^{3.7}$  and that of  $[\text{AuCl}_2]^-/\text{Au}^+$  would be  $10^{12.6}$ . Hence, under equilibrium conditions, the concentration of  $[\text{AuCl}_2]^-$  would always be much higher than that of the two other species and thus the predominate dissolved species is expected to be  $[\text{AuCl}_2]^-$  in the process of gold dissolution in 1M LiCl/DMSO. The cathodic peak at -0.75V then corresponds to the reduction of  $[\text{AuCl}_2]^-$  to Au in a one step process, which is in accordance with Suarez's investigations [108].

A two steps oxidation process was observed when the potential extended up to 1.8V from OCP, as also shown in Fig. 4.2. Chronocoulmetric measurements yielded a value of  $n$  for Au dissolution of  $n=1.3$  at 1.4V and between  $n=1.6$  and  $n=1.8$  at 1.8V. This demonstrates that gold was probably first oxidized to  $[\text{AuCl}_2]^-$ , which was then further oxidized to  $[\text{AuCl}_4]^-$ . However, a direct formation of  $[\text{AuCl}_4]^-$  from Au can not be excluded. No passivation or formation of an insoluble surface layer was observed in LiCl/DMSO, even though the potential range was extended to 1.8V. This is in contrast to aqueous chloride solutions, where passivation of the gold surface was indicated by a rapidly dropping anodic current when potential was scanned beyond 1.4V (data is not shown in this chapter). Upon reversing the potential scan direction after reaching 1.8V, small but wide cathodic waves evolved at 1V, 0.6V and 0.2V in addition to a well defined cathodic peak at -0.75V. Suarez's investigations demonstrated that the reduction of  $[\text{AuCl}_4]^-$  in DMSO was a two step process [108]. During the cathodic

sweep,  $[\text{AuCl}_4]^-$  was first reduced to  $[\text{AuCl}_2]^-$  and then  $[\text{AuCl}_2]^-$  was further reduced to Au. We ascribe at least one of the cathodic peaks at relatively positive potentials, probably the peak at 0.2V (see section 4.1.3), to the reduction of  $[\text{AuCl}_4]^-$  to  $[\text{AuCl}_2]^-$  and the well defined cathodic peak at -0.75V to the reduction of  $[\text{AuCl}_2]^-$  to Au. DMSO would slightly decompose when the potential extended beyond 1.2V. Hence, the cathodic waves at positive potentials may also partly correspond to the reduction of decomposition products of the solvent.

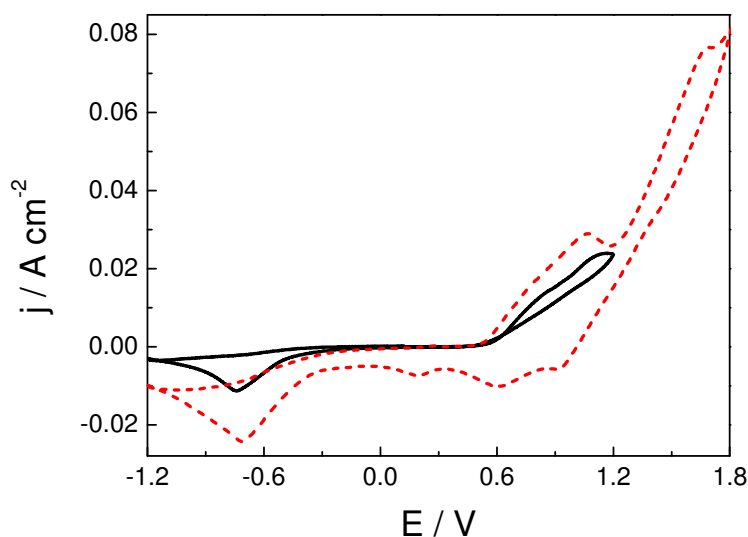


Fig. 4.2 Cyclic voltammograms of gold in 1M LiCl/DMSO. The parameters: RE: aqueous  $\text{Cl}^-/\text{AgCl}/\text{Ag}$  (sat. KCl); scan:  $\text{OCP} = 0.2\text{V} \rightarrow 1.2\text{V}$  or  $1.8\text{V} \rightarrow -1.2\text{V} \rightarrow \text{OCP}$ , scan rate: 50mV/s. This figure was adopted from our recent publication<sup>[102]</sup>.

### 4.1.3 Gold in LiCl/DMSO-water mixtures

The different electrochemical behavior of gold in LiCl/DMSO in comparison with that in aqueous chloride solutions, e.g., the different dissolved species, the varying cathodic peak position and the different number of the cathodic peaks, was observed and discussed in previous section. Physical properties such as viscosity, specific conductivity of LiCl in DMSO-water mixtures and in DMSO-methanol mixtures as well as the electrochemical stability of DMSO-water mixtures at a platinum electrode were investigated by Miles and his co-workers<sup>[110]</sup>. The variation of viscosity with the

mixture composition and the heat of mixing reflect the strong intermolecular interactions between DMSO molecules and water molecules, mainly via the formation of hydrogen bonds<sup>[111]</sup>. Because most of our machining experiments are conducted in an apparatus where the cell is open to air for a few hours (see Fig. 3.1 in chapter 3), a small amount of water from the atmosphere would be absorbed by DMSO. Therefore we are interested in the effect of the composition of DMSO-water mixtures on the electrochemistry of gold, which was also mainly studied with cyclic voltammetry.

Fig. 4.3 shows CVs of a polycrystalline Au foil in LiCl/DMSO-water mixtures (given as volume %). The concentration of LiCl was kept constant at 1M for all mixtures. The potential was cycled between 1.2V to -1.2V, starting from OCP towards 1.2V and then reversed. In order to exhibit the details of the cathodic part of the CVs, anodic current densities exceeding 30mA/cm<sup>2</sup> are not displayed in Fig. 4.3. Such high current densities were obtained in the mixtures containing more than 60% water. Though the effect of the solvent mixtures on the potential of the reference electrode can not be completely excluded, it can be noticed that the onset potentials of the dissolution shifted to more positive values with increasing water content, as shown in Fig. 4.3. The onset potential of dissolution was 0.5V in LiCl/DMSO and it was 0.85V in LiCl/H<sub>2</sub>O. The slope  $dj/dE$  of the dissolution current vs. potential steeply increased with increasing water content. In these experiments, the reference electrode was placed as close to the working electrode as possible. Although the specific electrolyte resistance of LiCl/DMSO is about 10 times of that of LiCl/H<sub>2</sub>O (see Fig. 4.6), the IR drop in the solutions is not expected to play a significant role. Hence, the observation, i.e., the slope  $dj/dE$  of the dissolution current increased with increasing water content indicates an increase of the exchange current density for gold dissolution with increasing water content.

The cathodic part of the CVs also shows strong solvent effects. In the mixture containing 10% water, only one cathodic peak was observed at -0.6V, which was about 150mV more positive than the cathodic current peak of [AuCl<sub>2</sub>]<sup>-</sup> in pure DMSO. Obviously, [AuCl<sub>2</sub>]<sup>-</sup> became less stable upon the addition of 10% water. The stability of [AuCl<sub>2</sub>]<sup>-</sup> was further decreased upon addition of 30% water, which is reflected by

the cathodic peak which shifted further positively to  $-0.3\text{V}$ . In addition, a small cathodic peak at  $0.2\text{V}$  was observed in a mixture with 30% water. Upon dissolution of gold at  $1.2\text{V}$ , 1.5 electrons were transferred per dissolved Au atom in a 30% water mixture, which points out that both, Au(I) and Au(III) chloro complexes were formed in a single anodic current wave. However it is hard to clarify the formation mechanisms of Au(III) chloro complexes. They might directly form from Au and dissolved as Au(III) chloro complex, or from the decomposition of unstable Au(I) complexes like in aqueous chloride solutions. We ascribe the small cathodic peak at  $0.2\text{V}$  to the reduction of  $[\text{AuCl}_4]^-$  to  $[\text{AuCl}_2]^-$  and the well defined cathodic peak at  $-0.3\text{V}$  to the reduction of  $[\text{AuCl}_2]^-$  to Au. Upon increasing the water content beyond 30%, the cathodic peaks further shifted positively and finally they combined into one well defined cathodic peak in water rich mixtures (water content  $>70\%$ ). This cathodic peak just shifted positively only about  $100\text{mV}$  from 70% water content mixture to pure water solutions.

Obviously, in DMSO rich mixtures (DMSO $>80\%$ ), gold exhibits a similar electrochemical behavior like that in pure DMSO; in water rich mixtures (water  $>70\%$ ), gold exhibits a similar electrochemical behavior as in aqueous chloride solutions. A gradual transition from the characteristic behavior in DMSO to the characteristic behavior in aqueous solution was shown for the electrochemistry of gold in intermediate mixtures. Two cathodic peaks were observed in the intermediate mixtures (30%-60% water), indicating that both  $[\text{AuCl}_2]^-$  and  $[\text{AuCl}_4]^-$  (probably) were formed and coexisted. The shifts of the peak positions of the cathodic peaks directly indicate that the relative stability of  $[\text{AuCl}_2]^-$  and of  $[\text{AuCl}_4]^-$  varied with the mixture composition. Since DMSO itself is a weak ligand for Au(I) and Au(III) ions and the activity of  $\text{Cl}^-$  is relatively low in water rich mixtures (see the following discussion), the existent of a very small fraction of Au(III)-DMSO complexes can not be completely excluded. Similarly,  $[\text{CuDMSO}_6]^{2+}$  was found in water-DMSO mixtures<sup>[112]</sup>.

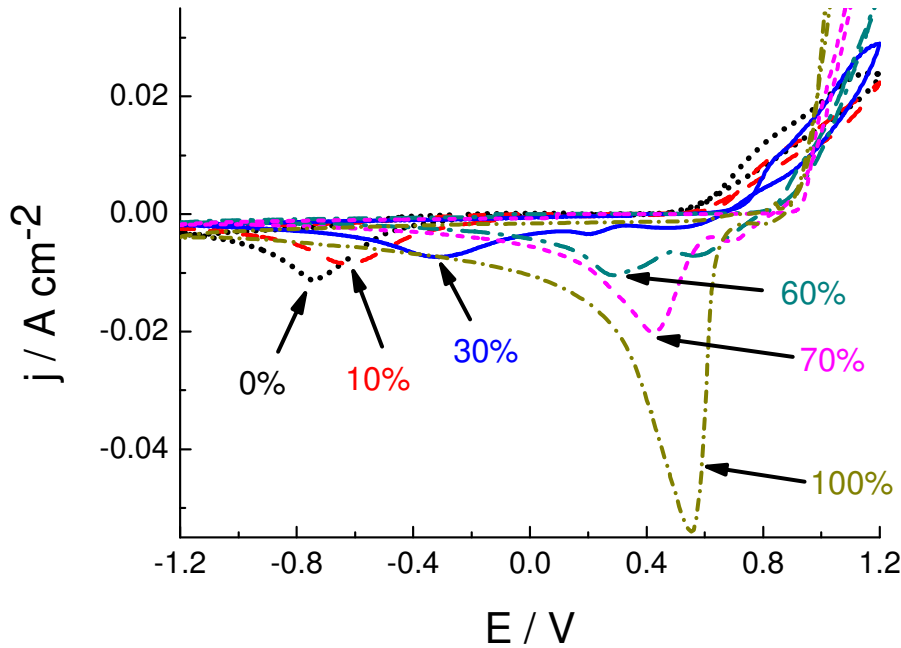


Fig. 4.3 Cyclic voltammograms of gold in 1M LiCl in (100-x)% DMSO + x% H<sub>2</sub>O mixtures. RE: aqueous Cl<sup>-</sup>/AgCl/Ag (sat. KCl), scan rate: 50mV/s. The figure was adopted from our recent publication<sup>[102]</sup>.

#### 4.1.4 Thermodynamic considerations

The different electrochemical behavior of gold in water, DMSO and DMSO-water mixtures, containing 1M LiCl, can be understood through the variation of the activity of the Cl<sup>-</sup> in those solvents as well as the stability of the dissolved species. The relative activity of a species in two solvents can be indicated by standard Gibbs energy of transfer, i.e.,  $\Delta G_t^0(i, R \rightarrow S)$ , from a reference solvent R (typically water) to the solvent S of interest. The standard Gibbs energy of transfer for a species i is equal to its different solvation energies  $\Delta G_{sv}^0(i)$  in two solvents, as expressed by equation 4.3<sup>[103]</sup>:

$$\Delta G_t^0(i, R \rightarrow S) = \Delta G_{sv}^0(i, S) - \Delta G_{sv}^0(i, R), \quad (4.3)$$

where  $\Delta G_{sv}^0(i, S)$  is the solvation energy of the species i in solvent S and  $\Delta G_{sv}^0(i, R)$  is the solvation energy of the species i in solvent R. The species i can be an ion or an



electrical neutral molecule or an atom.

Using a solvent independent reference electrode, e.g.,  $\text{Fc}^+/\text{Fc}$ , the standard Gibbs energy of transfer for a metal ion  $\text{M}^{z+}$ , can be obtained by separated measurements of the standard electrode potentials of a  $\text{M}^{z+}/\text{M}$  couple in two solvents S and R, as expressed by equation 4.4<sup>[103, 113]</sup>:

$$\Delta G_t^0(\text{M}^{z+}, \text{R} \rightarrow \text{S}) = zF(E_{\text{S},\text{M}^{z+}}^0 - E_{\text{R},\text{M}^{z+}}^0). \quad (4.4)$$

Where F is the Faraday constant of 96485 C/mol, z is the charge of the metal ion  $\text{M}^{z+}$ ,  $E_{\text{S},\text{M}^{z+}}^0$  is the standard electrode potential of  $\text{M}^{z+}/\text{M}$  in solvent S and  $E_{\text{R},\text{M}^{z+}}^0$  is the standard electrode potential of  $\text{M}^{z+}/\text{M}$  in solvent R.

Similarly, the standard Gibbs energy of transfer for an anion  $\text{X}^-$  can be obtained by separated measurements of the different standard electrode potentials of  $\text{X}^-/\text{AgX}/\text{Ag}$  in two solvents S and R with respect to a solvent independent reference electrode, as expressed by equation 4.5<sup>[113]</sup>:

$$\Delta G_t^0(\text{X}^-, \text{R} \rightarrow \text{S}) = F(E_{\text{R},\text{X}^-}^0 - E_{\text{S},\text{X}^-}^0). \quad (4.5)$$

$E_{\text{S},\text{X}^-}^0$  is the standard electrode potential of  $\text{X}^-/\text{AgX}/\text{Ag}$  in solvent S and  $E_{\text{R},\text{X}^-}^0$  is the standard electrode potential of  $\text{X}^-/\text{AgX}/\text{Ag}$  in solvent R. However, the direct measurement of the standard electrode potential of an  $\text{X}^-/\text{AgX}/\text{Ag}$  electrode is impossible if the  $\text{AgX}$  is soluble in the solvents. For example, due to the high solubility of  $\text{AgCl}$ , direct measurement of the electrode potential of  $\text{Cl}^-/\text{AgCl}/\text{Ag}$  electrode is impossible in acetonitrile with high concentration of  $\text{Cl}^-$ <sup>[103]</sup>.

The difference of the standard electrode potentials of  $\text{Cl}^-/\text{AgCl}/\text{Ag}$  in water and in DMSO is 0.42V at 25°C<sup>[113]</sup> and then the standard Gibbs energy of transfer for  $\text{Cl}^-$  from water to DMSO is about 40 kJ/mol at 25°C<sup>[103, 114]</sup>. The positive value of the standard Gibbs energy of transfer for  $\text{Cl}^-$  indicates the poor solvation of  $\text{Cl}^-$  ions in DMSO.

The different activity of a species i in two solvents R and S can be more directly reflected by a transfer activity coefficient,  $\log \gamma_t(i, \text{R} \rightarrow \text{S})$ , which is related to the standard Gibbs energy of transfer by equation 4.6<sup>[103]</sup>:

$$\Delta G_t^0(i, R \rightarrow S) = 2.303RT \times \log \gamma_t(i, R \rightarrow S). \quad (4.6)$$

Where R is the molar gas constant of  $8.31 \text{ J mol}^{-1} \text{ K}^{-1}$ , T is temperature in Kelvin.

Calculating from the standard Gibbs energy of transfer for  $\text{Cl}^-$  from water to DMSO of about  $40 \text{ kJ/mol}$ , the activity of  $\text{Cl}^-$  in DMSO is about  $10^7$  times of that in water at  $25^\circ\text{C}$ . We ascribe the increased activity of  $\text{Cl}^-$  in DMSO to be one of the reasons for the easy formation and the difficult reduction of  $[\text{AuCl}_2]^-$  in DMSO, as observed in the CVs (see Fig. 4.2 and 4.3). More straightforward, the standard Gibbs energy of transfer for  $[\text{AuCl}_2]^-$  from water to DMSO can be calculated by equation 4.7<sup>[112]</sup>:

$$\begin{aligned} \Delta G_t^0([\text{AuCl}_2]^- , \text{H}_2\text{O} \rightarrow \text{DMSO}) &= 2.303RT(\log \beta_2^{\text{H}_2\text{O}} - \log \beta_2^{\text{DMSO}}) \\ &+ \Delta G_t^0(\text{Au}^+ , \text{H}_2\text{O} \rightarrow \text{DMSO}) \\ &+ 2\Delta G_t^0(\text{Cl}^- , \text{H}_2\text{O} \rightarrow \text{DMSO}), \end{aligned} \quad (4.7)$$

where  $\log \beta_2$  is the stability constants of  $[\text{AuCl}_2]^-$  in water and in DMSO ( $\log \beta_2^{\text{H}_2\text{O}} = 11$ <sup>[99]</sup>,  $\log \beta_2^{\text{DMSO}} = 16.6$ <sup>[108]</sup>). The first term  $2.303RT(\log \beta_2^{\text{H}_2\text{O}} - \log \beta_2^{\text{DMSO}})$  is determined to be  $-32 \text{ kJ/mol}$  at  $25^\circ\text{C}$  from the different stability constants of  $[\text{AuCl}_2]^-$  in water and in DMSO. The standard Gibbs energy of transfer for  $\text{Au}^+$  from water to DMSO,  $\Delta G_t^0(\text{Au}^+ , \text{H}_2\text{O} \rightarrow \text{DMSO})$ , can be determined to be  $-57.9 \text{ kJ/mol}$  from the difference of the standard electrode potential of  $\text{Au}^+/\text{Au}$  in the two solvents of about  $600 \text{ mV}$ , as mentioned above. A negative value of  $\Delta G_t^0(\text{Au}^+ , \text{H}_2\text{O} \rightarrow \text{DMSO})$  is expected since the free  $\text{Au}^+$  is more stable in DMSO. The term  $\Delta G_t^0(\text{Cl}^- , \text{H}_2\text{O} \rightarrow \text{DMSO})$  is  $40 \text{ kJ/mol}$ <sup>[103, 114]</sup>. Then the standard Gibbs energy of transfer for  $[\text{AuCl}_2]^-$  from water to DMSO can be determined to be about  $-10 \text{ kJ/mol}$  at  $25^\circ\text{C}$ . Obviously, the positive Gibbs energy of transfer for  $\text{Cl}^-$  is overcompensated by the negative Gibbs energy of transfer for  $\text{Au}^+$  and the strong stabilization of  $[\text{AuCl}_2]^-$  in DMSO.

By application of equation 4.4, the difference of the standard electrode potential of  $[\text{AuCl}_2]^-/\text{Au}$  in DMSO and in water can also be determined, as expressed by equation 4.8:

$$(E_{\text{H}_2\text{O}}^0([\text{AuCl}_2]^-/\text{Au}) - E_{\text{DMSO}}^0([\text{AuCl}_2]^-/\text{Au})) = -\Delta G_t^0([\text{AuCl}_2]^- , \text{H}_2\text{O} \rightarrow \text{DMSO})/F + 2\Delta G_t^0(\text{Cl}^- , \text{H}_2\text{O} \rightarrow \text{DMSO})/F. \quad (4.8)$$

This results in the standard electrode potential of  $[\text{AuCl}_2]^-/\text{Au}$  in DMSO of -930mV with respect to the standard electrode potential of  $[\text{AuCl}_2]^-/\text{Au}$  in water. Therefore, we can conclude that the thermodynamic calculations are in good agreement with the experimental observations, i.e., the reduction of  $[\text{AuCl}_2]^-$  requires a rather negative potential (see CVs in Fig. 4.3).

Considering the effects of water in DMSO-water mixtures, the standard Gibbs energy of transfer for  $[\text{AuCl}_2]^-$  from pure DMSO to pure water is just about 10kJ/mol, which is 1/4<sup>th</sup> of the standard Gibbs energy of transfer for  $\text{Cl}^-$  from pure water to pure DMSO. Hence for a simplification, here we only consider the influences of the water content on the activity of  $\text{Cl}^-$  ions and the subsequent electrochemical behavior of gold. The standard Gibbs energy of transfer for  $\text{Cl}^-$  ions from water to water-DMSO mixtures were measured by Kundu and Parker<sup>[115]</sup>. According to their results,  $\Delta G_t^0(\text{Cl}^-)$  is about -20 kJ/mol for transferring  $\text{Cl}^-$  from pure DMSO to 30% (volume ratio) water-DMSO mixture. Therefore, the activity of  $\text{Cl}^-$  would be lowered by a factor of  $10^{3.5}$  at 25°C upon addition of 30% water. On the other hand, in water rich mixtures, upon adding DMSO to pure water,  $\Delta G_t^0(\text{Cl}^-)$  is less sensitive to the fraction of DMSO. It is only 3.5 kJ for transfer of one mole of  $\text{Cl}^-$  ions from pure water to 70% water-DMSO mixture. The decreasing activity of  $\text{Cl}^-$  with increasing water content in mixtures results in the destabilization of  $[\text{AuCl}_2]^-$  and the formation of  $[\text{AuCl}_4]^-$ , indicated by the number of transferred electrons per dissolved Au atom of 1.3 in the 30% water containing mixture and the two cathodic peaks (see Fig. 4.3), similar to the destabilization of Cu(I) and Ag(I) chloro complexes in DMSO-water mixtures<sup>[112]</sup>. The activity of  $\text{Cl}^-$  is weakly dependent on the water content in water rich mixtures while strongly dependent on the water content in DMSO rich mixtures. This might be one of reasons for the small positive shifting of the cathodic peak by about 100mV in water rich mixtures from 70% water mixture to 100% water. In contrast, the cathodic peak was shifted positively about 450mV upon addition of 30% water to DMSO. In

summary, water affects the activity of the  $\text{Cl}^-$  ions, the dissolution species and their stability as well as the irreversibility of the gold dissolution/deposition in various mixtures. However, 10% water does not significantly affect the dissolution species and their stability, the electrochemical potential window of gold dissolution and deposition and hence the electrochemical micromachining (see section 4.2.2.4).

### 4.1.5 Differential capacitance of gold in LiCl/DMSO

Knowledge of the double layer capacitance of gold in LiCl/DMSO is very important for the estimation of the charging time constant of the double layer and hence for the estimation of the machining precision (defined in section 4.2.2) in electrochemical machining. Double layer capacitances of a polycrystalline gold electrode in  $\text{LiClO}_4/\text{DMSO}$  between  $7\mu\text{F}/\text{cm}^2$  and  $12\mu\text{F}/\text{cm}^2$  were reported over a wide potential range from  $-0.12\text{V}$  to  $0.57\text{V}$ <sup>[116]</sup>. The concentration of  $\text{LiClO}_4$  varied from  $0.003\text{M}$  to  $0.03\text{M}$ . Since the concentrations of  $\text{LiClO}_4$  were low, the contribution of the diffuse layer capacitance cannot be neglected. Furthermore, in highly concentrated LiCl/DMSO solutions, the specific ionic adsorption of  $\text{Cl}^-$  should be considered. Thus we can not use the double layer capacitances of gold in  $\text{LiClO}_4/\text{DMSO}$  to estimate the double layer charging constant of gold in highly concentrated LiCl/DMSO.

For measurements of the differential capacitance of gold in LiCl/DMSO, a  $\phi$  1mm gold wire (Wieland, 99.999%) was sealed into a PTFE tube to obtain a defined electrode area. The front face of the wire was polished with  $3\mu\text{m}$  and  $1\mu\text{m}$  diamond paste and then cleaned in an ultrasonic cleaner before each measurement. The active surface area of the  $\phi$  1mm gold planar electrode was determined by chronoamperometry in freshly prepared  $10.7\text{mM}$   $\text{K}_4\text{Fe}(\text{CN})_6 + 0.1\text{M}$   $\text{KCl}$  solutions. The  $[\text{Fe}(\text{CN})_6]^{4-}$  was oxidized to  $[\text{Fe}(\text{CN})_6]^{3-}$  under mass-transport controlled conditions by application of  $0.5\text{V}$  vs. a Pt wire quasi-reference electrode and the current vs. time curve was recorded for the first second soon after application of the  $0.5\text{V}$ . According to the Cottrell equation for a planar electrode under diffusion

controlled process, the current vs. time curve is given as  $i(t) = \frac{nFAD^{1/2}C_0}{\pi^{1/2}} t^{-1/2}$  [45] for a short recording time. Deviation due to radial current can be neglected for short recording time of a few seconds. This is because the thickness of the diffusion layer  $(Dt)^{1/2}$  for an active species with a typical diffusion coefficient  $D$  of  $10^{-5} \text{ cm}^2/\text{s}$  [45] in a few seconds is much smaller than the radius of the planar electrode of 0.5mm. Hence the current is linearly dependent on  $t^{-1/2}$  for the planar gold electrode with 1mm diameter, as shown in Fig. 4.4. There is one data point which deviates from the straight line, which was caused by the high charging current of the double layer (nonfaradic current) soon after the application of the 0.5V potential step. The slope of the plot is about  $2.10 \times 10^{-5} \text{ A}\cdot\text{s}^{1/2}$ . The diffusion coefficient of  $\text{K}_4\text{Fe}(\text{CN})_6$  is  $6.61 \times 10^{-6} \text{ cm}^2/\text{s}$  at room temperature [117]. Hence the active surface area of the gold electrode was determined to be  $0.014 \text{ cm}^2$ , which is 1.78 times of the geometrical surface area of the gold electrode. The active surface area is bigger than the geometrical surface area, which might be due to surface roughness upon polishing and bad insulation.

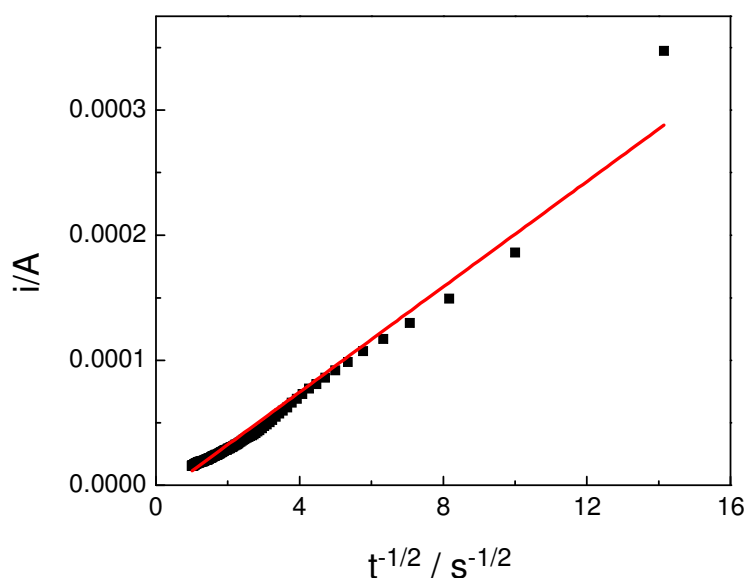


Fig. 4.4 Plot of current versus  $t^{-1/2}$  of a  $\phi$  1mm gold planar electrode in 10.7mM  $\text{K}_4\text{Fe}(\text{CN})_6$  + 0.1M KCl solution by application of 0.5V.

The method and the set-up for the measurement of the differential capacitance of solid electrodes have already been described in chapter 3. Fig. 4.5 shows the capacitance vs. potential curves of the  $\phi$  1mm gold planar electrode in LiCl/DMSO solutions. The concentrations of LiCl varied from 0.005M to 1M, as indicated in the caption of Fig. 4.5. The potential of the gold electrode was varied from -0.55V to 0.2V with a scan rate of 20mV/s. The double layer capacitances of the gold electrode in low concentration LiCl/DMSO are between  $10\mu\text{F}\cdot\text{cm}^{-2}$  and  $15\mu\text{F}\cdot\text{cm}^{-2}$  over the wide potential window and the capacitance vs. potential curves are relatively flat. In highly concentrated solutions, capacitances between  $30\mu\text{F}\cdot\text{cm}^{-2}$  and  $60\mu\text{F}\cdot\text{cm}^{-2}$  were found, which are comparable to the values of the double layer capacitances of a Au(111) electrode in 1M HClO<sub>4</sub> aqueous solution<sup>[118]</sup>. Since the contribution of the diffuse layer capacitance can be neglected in 1M LiCl/DMSO solution, the capacitance vs. potential curve reflects the variation of the Helmholtz plane capacitance with potential. The double layer capacitance of gold in high concentration LiCl/DMSO is strongly dependent on the electrode potential or electrode charge density. At -0.55V, where the specific adsorption of Cl<sup>-</sup> can be excluded, the capacitance changed by only  $15\mu\text{F}\cdot\text{cm}^{-2}$  from 0.005M LiCl/DMSO to 1M LiCl/DMSO solutions due to the influence of the diffuse layer capacitance. In contrast, at 0.2V, the capacitance changed by about  $45\mu\text{F}\cdot\text{cm}^{-2}$  from 0.005M LiCl/DMSO to 1M LiCl/DMSO solutions. This indicates the specific adsorption of Cl<sup>-</sup> at more positive potentials in concentrated solutions, which plays an important role on the double layer capacitance. However, here we do not go into the structure of Au/DMSO double layer and the interactions between solvent and solute with the electrode surface. For example, the adsorption of DMSO on gold surface was already studied by Si and Gewirth<sup>[119]</sup>. We are more interested in the value of the double layer capacitance of the polycrystalline gold electrode in 1M LiCl/DMSO for estimation of the charging time constant of the double layer at Au/DMSO interface. The double layer capacitance of gold in 1M LiCl/DMSO was determined to be about  $50 \pm 5\mu\text{F}\cdot\text{cm}^{-2}$  in the potential region between -100mV and 100mV, which is the rest potential range of the gold workpieces during electrochemical micromachining. The double layer capacitance of gold in 80%

DMSO+20% H<sub>2</sub>O mixture containing 1M LiCl is about 10 $\mu\text{F}\cdot\text{cm}^{-2}$  lower than that in 1M LiCl/DMSO, as indicated by the curve (e) in Fig. 4.5.

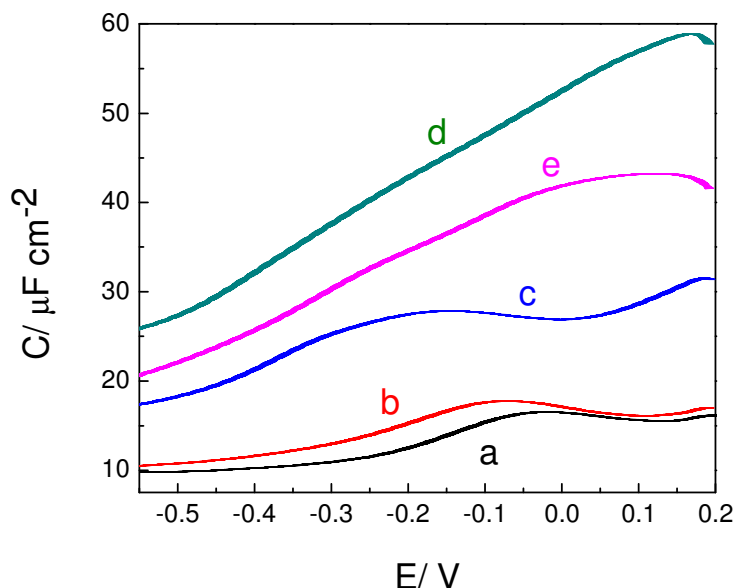


Fig. 4.5 Capacitance vs. potential curves of a  $\phi$  1mm gold planar electrode in (a) 0.005M LiCl/DMSO; (b) 0.01M LiCl/DMSO; (c) 0.1M LiCl/DMSO; (d) 1M LiCl/DMSO and (e) 1M LiCl in 80% DMSO+20% H<sub>2</sub>O mixture.

#### 4.1.6 Specific resistance of LiCl in DMSO-water mixtures

Specific conductivity and specific resistance of 1M LiCl in DMSO-water mixtures were measured with a HP 4275A LCR meter. The modulation was a 10mV, 25kHz sine wave. Fig. 4.6 shows the mixture composition depended specific conductivity and the specific resistance of 1M LiCl in DMSO-water mixtures at room temperature. The tendency of the specific conductivity versus water content is in accordance with Miles' measurements<sup>[110]</sup>. The specific conductivities almost remain constant in DMSO rich mixtures with water content less than 20%. The specific conductivity only slowly increases with increasing water content up to about 50% water fraction. In water rich mixtures, the conductivity increases rapidly with increasing water content. Although the conductivity is inversely proportional to the viscosity of the solvent, the lowest conductivity does not occur at the mixture with the highest viscosity, which

contains 50% of water in mole fraction<sup>[110]</sup>. This is because only about 40% of 1M LiCl is ionized in pure DMSO<sup>[110]</sup>. The specific resistances of 1M LiCl also remain constant at about 150 $\Omega$ -cm in DMSO rich mixtures with water content less than 20% and reach about 15 $\Omega$ -cm in water rich mixtures with water content more than 80%. In the intermediate mixtures, the specific resistances of 1M LiCl are strongly dependent on the composition of the mixtures. Generally, the specific resistance of 1M LiCl increases by a factor of 10 from water to DMSO, which makes the LiCl/DMSO electrolytes possible to achieve high machining precision using relatively long duration voltage pulses in electrochemical micromachining.

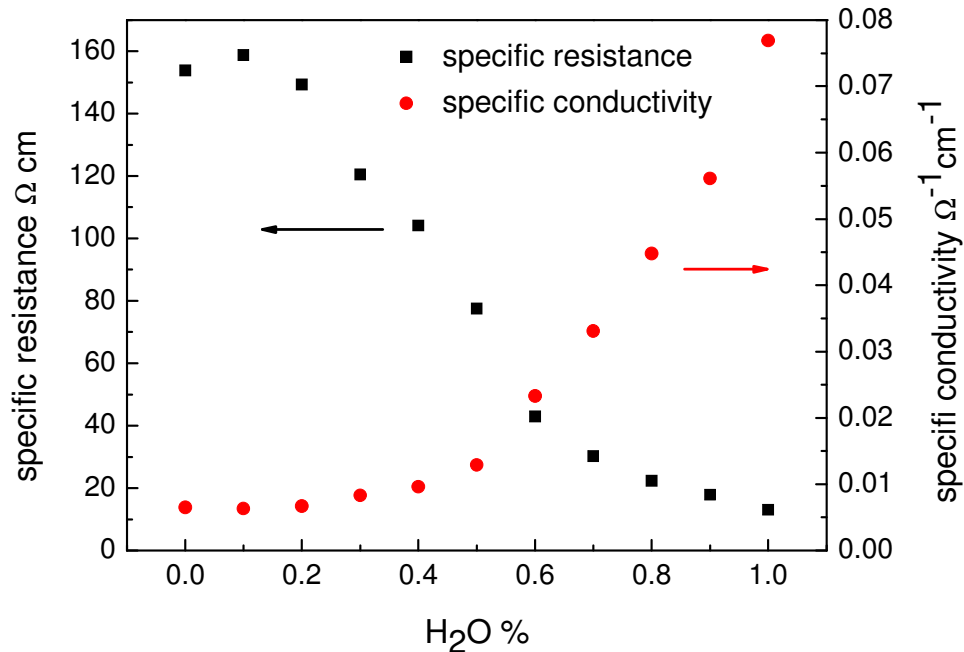


Fig. 4.6 Plots of specific conductivity (red circle) and specific resistance (black square) of 1M LiCl in DMSO-water mixtures as a function of water content at room temperature.

#### 4.1.7 Electrochemistry of LiCl/DMSO at carbon fibers

In the process of electrochemical micromachining, the potential of the tools is set to relatively positive versus the workpiece to avoid the re-deposition of dissolved materials on the tools. The stability of the electrolyte at the tools and of the tools



themselves is also important when high positive potentials are applied. For machining of gold, in order to avoid re-deposition of dissolved gold at the tools, the tool materials have to be electrochemically stable in LiCl/DMSO up to potentials of about 1V vs. the potential of the gold workpiece. It turns out that even Ir, which is one of the electrochemically most stable metals, is slowly dissolved. We therefore employed commercially available carbon fibers with a diameter of 7 $\mu$ m (Goodfellow) as tool electrodes for machining. Fig. 4.7 shows the CV of a  $\phi$  7 $\mu$ m carbon fiber in 1M LiCl/DMSO. Since the active surface area of the carbon fiber was not determined, the current is given rather than the current density. The potential was initially scanned in positive direction to 2.5 V and then reversed to -2.5V. Anodic current was observed when the potential exceeded 1.05V, which we ascribe to the oxidation of Cl<sup>-</sup> due to the high activity of Cl<sup>-</sup> in DMSO. No cathodic current was observed during the reversal scan to -2.5V. As indicated by the CV, the tool potential should not strongly exceed 1.05V vs. Cl<sup>-</sup>/AgCl/Ag during the machining process. Otherwise, the concentration of Cl<sup>-</sup> in the gap between the carbon fiber and the gold workpiece would be decreased due to the electrochemical oxidation of Cl<sup>-</sup>, which would occur in the pause period of the pulse train. In our machining experiments, a Pt wire pseudo-reference electrode was used. Its potential in DMSO was about -200mV with respect to the aqueous Cl<sup>-</sup>/AgCl/Ag electrode. Hence, in most of machining experiments, the potential of the tools was chosen in the range between 0.8V and 1.0V versus the Pt pseudo-reference electrode and no remarkable effect on micromachining was observed. When the potentials of carbon fibers were too high, e.g., 1.3V, decreasing machining speed was observed, which pointed to the oxidation of Cl<sup>-</sup>. Gold deposition on the carbon fiber tool was observed when the potentials were chosen too low, e.g., 0.6V.

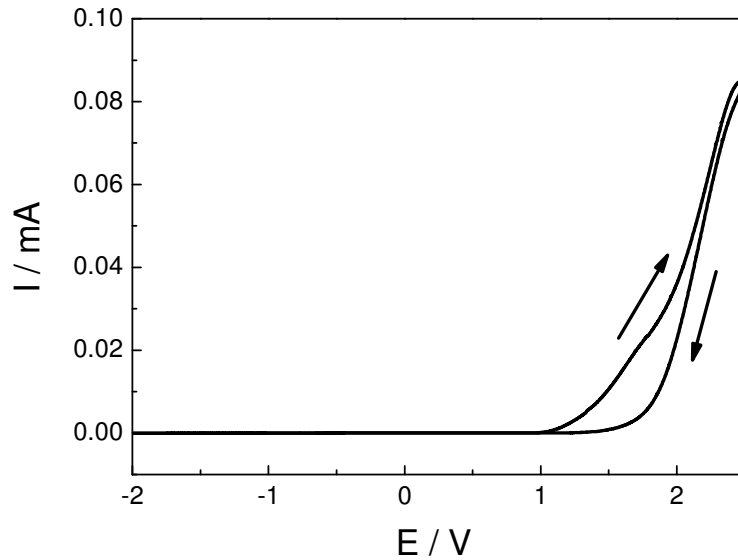


Fig. 4.7 Cyclic voltammogram of 1M LiCl/DMSO at a  $\phi$  7 $\mu$ m carbon fiber electrode; RE: aqueous Cl<sup>-</sup>/AgCl/Ag (sat. KCl), scan rate: 50mV/s.

## 4.2 Electrochemical machining of gold nanostructures

### 4.2.1 Preparation of carbon fiber tools

The carbon fibers with a diameter of 7 $\mu$ m are too small to be conveniently handled and to be directly mounted at the micromachining set-up. In order to manipulate the fibers easily, each fiber is usually fixed to a steel needle with an outer diameter of 0.4mm. The processes for mounting the fibers are as following: the steel needle is connected to a vacuum pump to draw one carbon fiber into its 150 $\mu$ m diameter capillary. Then the fiber is electrically connected to the steel needle with silver paint. In order to avoid the silver paint to dissolve in the DMSO solutions during machining, it is insulated by Apiezon wax which can resist water and most organic solvents. Finally the mounted fiber is cut to the desired length. Since the front face of the fiber is not flat after the mechanical cutting, it is flattened by vertically approaching to a rotating disk covered with an Al<sub>2</sub>O<sub>3</sub> polishing paper. SEM images of a flattened carbon fiber are shown in Fig. 4.8. The contamination on the top of the fiber (see Fig. 4.8) probably originated from the polishing paper and can be easily removed in an

ultrasonic cleaner before machining.

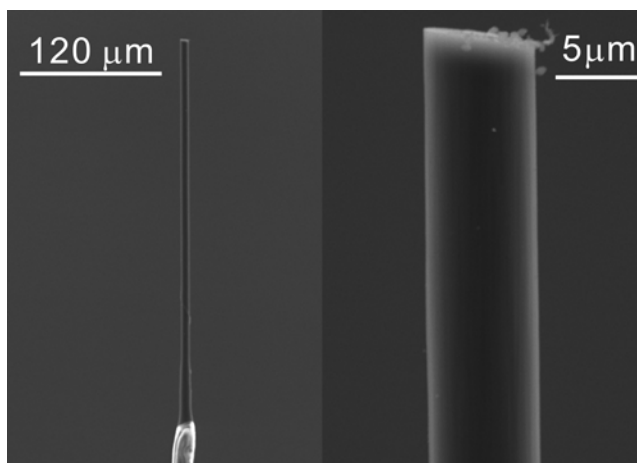


Fig. 4.8 SEM images of a mechanically flattened carbon fiber.

In order to obtain nanometer-sized tools for machining of nanostructures, three methods have been tried to sharpen the carbon fibers. In the first approach (introduced by Dr. Andreas Bán), the carbon fibers were sharpened by approaching a rotating polishing paper with an angle typically between  $15^\circ$  and  $60^\circ$ . The fibers were also rotating during sharpening. However, it was very difficult to place the fibers at the rotation axis of the motor which controlled the rotation of the fibers. The asymmetrical contact angles of the fibers with the polishing paper resulted in asymmetrical cones of sharpened fibers. Fig. 4.9 (a) shows an SEM image of a typical carbon fiber tip obtained by mechanical sharpening, whose radius of curvature is about 500nm. The relatively big size of sharpened tips as well as the poorly reproducible shape limits the application of this approach.

Burning of carbon fibers by a heated metal wire coil was the second method to reduce the size of the carbon fibers. Briefly, a 5 turn coil of a  $\phi$  0.2mm Pt wire was heated up by application of a few volts. The exact temperature inside the wire coil was not measured. The temperature was estimated by the colour of the coil. When the coil was heated up and became red, the carbon fiber was moved into the centre of the coil from beneath using a micrometer screw. The fiber was kept inside the glowing coil for a few seconds before it was moved out. Fig. 4.9 (b) shows an SEM image of a burned carbon

fiber tip, whose diameter is about 600nm. The carbon fibers became brittle after burning. Additionally, the surface of the fibers was porous. These disadvantages limit the application of this approach to produce the nanometer-sized carbon fiber tools.

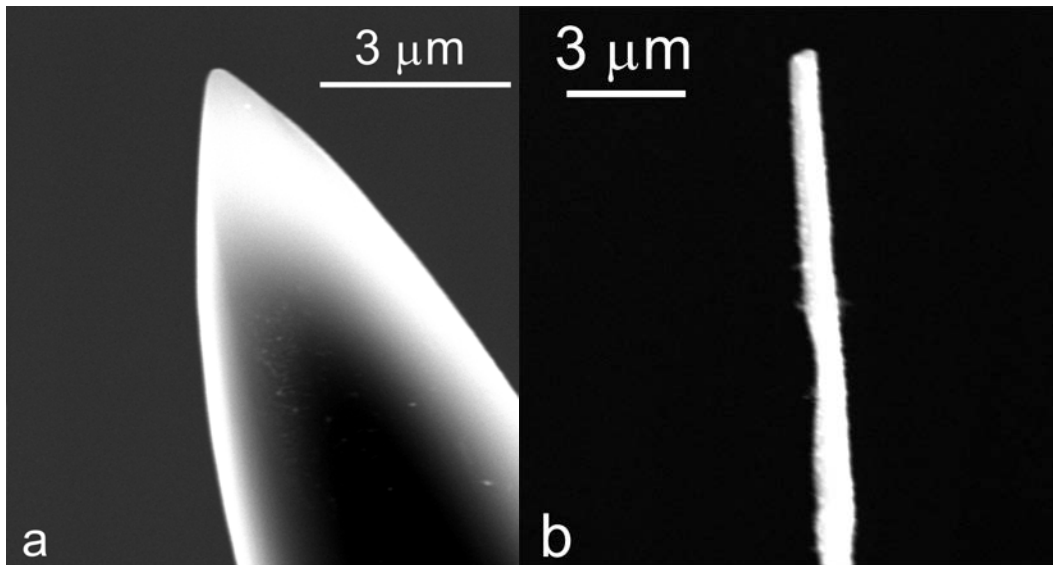
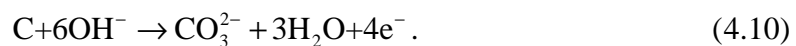


Fig. 4.9 SEM images of (a) a mechanically sharpened carbon fiber and (b) a burned carbon fiber.

Electrochemical etching is a common method for producing metal tips. Nanometer-sized carbon fibers can also be obtained by electrochemical etching<sup>[120, 121]</sup>. Electrochemical etching in 1M NaOH solutions was the third method we tried for the preparation of the carbon fiber tips.

The main electrochemical oxidation product of carbon in basic solutions is carbonate. The overall reaction of electrochemical oxidation of carbon is following<sup>[122]</sup>:



The set-up we used for the electrochemical etching of carbon fibers is sketched in Fig. 4.10 (a). A sine wave ( $3.1\text{V}_{\text{p-p}}$ , 50Hz) generated by a HP 3310A function generator was applied between the carbon fiber and the Pt ring counter electrode. The etching process was monitored via the cell current. The electrochemical etching current was relatively low because of the small surface area of the carbon fiber. An I-U amplifier was used to convert the current into voltage. Since a 680 k $\Omega$  resistor was connected in

the feedback loop of the amplifier, 1mA of current corresponded to 0.68V output voltage. The initial current indicated the immersed depth of the carbon fiber. Current in the range between 2.6mA and 3mA indicated that the carbon fiber was immersed about 100 $\mu\text{m}$  into the solution. When the etching current decreased to 1/10<sup>th</sup> of the initial value after several minutes, a sharpened carbon fiber tip was obtained. One of the electrochemically sharpened carbon fiber tips with a diameter of 100nm is shown in Fig. 4.10 (b). Thus, the electrochemical etching can reproducibly produce nanometer-sized carbon fiber tips for the purpose of nanomachining.

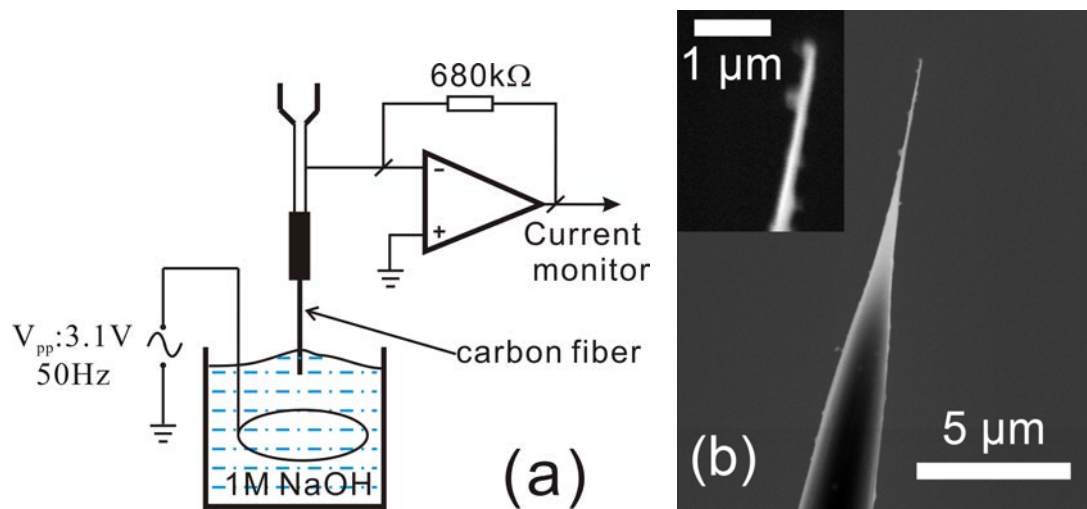


Fig. 4.10 (a) Schematic diagram of the set-up for electrochemical etching of carbon fibers; (b) SEM image of an electrochemically sharpened carbon fiber, adopted from our recent publication<sup>[102]</sup>.

With respect to the machining parameters, another important property of the carbon fibers is its resistance. The specific resistance of the carbon fibers we use is 1500 $\mu\Omega\cdot\text{cm}$  (obtained from Goodfellow), which is about 150 times of the specific resistance of metals, e.g., Pt. Therefore, the effect of the resistance of the carbon fibers on micromachining should be considered. The specific electrolyte resistance of 1M LiCl/DMSO is about 150 $\Omega\cdot\text{cm}$  (see Fig. 4.6), which is in accordance with Parker et al.' measurements<sup>[109]</sup>. Assuming a distance between the carbon fiber and the workpiece of 1 $\mu\text{m}$ , an electrolyte resistance along the gap of about  $1.5 \times 10^{-2} \Omega\cdot\text{cm}^2$

would be resulted. For a  $\phi 7\mu\text{m}$  carbon fiber with a specific resistance of about  $1500\mu\Omega\text{-cm}$ , a 1mm long carbon fiber as typically used in our experiments results in a resistance of about  $1.5\times 10^{-4}\ \Omega\text{-cm}^2$ . This is only  $1/100^{\text{th}}$  of the electrolyte resistance of the  $1\mu\text{m}$  workpiece-tool gap. Therefore, the resistance of the  $\phi 7\mu\text{m}$  carbon fibers can be neglected in comparison with the electrolyte resistance. However, sometimes influence of the sharpened carbon fiber tips on the machining parameters was observed and the machining parameters had to be slightly adjusted from tip to tip. We attribute these differences rather to the electrical connection between fibers and the steel capillary and the increased resistance of the sharpened part of the fibers due to its nanometer-sized diameter than to the resistance of the  $\phi 7\mu\text{m}$  shaft of the carbon tips. Therefore, the length of the sharpened part also needs to be considered. The diameter of the carbon fibers is usually reduced to less than 100nm and the sharpened part is typically about  $10\mu\text{m}$  long (see Fig. 4.10 b). It is therefore very flexible and can be easily bended. Trouble might arise from mechanical contact of the flexible sharpened part with the workpiece during approaching the workpiece. The approaching of the tip towards the workpiece is monitored via measuring the electric contact. After detecting the electric contact, the tip is withdrawn to typically  $2\mu\text{m}$  above the workpiece. This position is used as starting position for machining. Since the carbon fiber tip is very flexible and can be bended easily by a very small force when it contacts the workpiece, the detection of the electric contact is very critical. If the detection of the electrical contact is not sufficiently sensitive, strong anodic corrosion at the contact position would occur. Therefore, i) the electric contact measurement must be very sensitive; ii) the electric connection between the carbon fiber and the steel capillary must be well conducting; iii) the sharpened part of the fibers should be as short as possible; and vi) the surface of the workpiece must be fresh and not covered by an oxide film. Generally, the electrochemical sharpening is the best method to reproducibly prepare nanometer-sized carbon fiber tips. However, attention should be paid in every step of the preparation of the tips to minimize the influence of tip-preparation on electrochemical machining.

## 4.2.2 Electrochemical micromachining of gold

Most of electrochemically active materials ranging from metals to semiconductors can be machined by the electrochemical machining method upon application of short voltage pulses<sup>[43]</sup>. In this chapter, we investigate electrochemical micromachining of gold in LiCl/DMSO. The influence of machining parameters like pulse duration, pulse amplitude, rest potentials of gold workpiece and the effect of water content in DMSO-water mixtures are thoroughly discussed. As a test structure, 10 $\mu$ m deep holes were drilled using a 7 $\mu$ m diameter cylindrical carbon fiber tool with varying machining parameters. The machining precision was estimated by the gap width between the tool and the hole, defined by  $(\phi_{\text{hole}} - \phi_{\text{tool}})/2$ .

### 4.2.2.1 Influence of pulse duration

Fig. 4.11 (a) shows SEM images of a series of 10 $\mu$ m deep holes drilled into an Au foil in 1M LiCl/DMSO with varying pulse durations from 20ns to 100ns. Other parameters were kept constant. In all experiments pulse trains with a pulse-to-pause ratio of 1:9 were employed. The long pause time allowed the double layers to relax to their rest potentials and enabled sufficient mass transport. The carbon fiber tool was slowly fed into the Au foil with a rate of 1 $\mu$ m/10min which corresponded to 100min/hole. This feed rate corresponded to the maximum feed rate for the slowest etching process, i.e., upon application of 3.0V, 20ns pulses. This ensured that all holes could be drilled with the same feed rate of the tool. The holes appear slightly elongated, since the tool was tilted a few degrees off the surface normal. The diameter of the holes was measured along the shortest axes. The diameter of the holes increased from 8.1 $\mu$ m to 10.1 $\mu$ m with increasing pulse duration from 20ns to 100ns. Fig. 4.11 (b) shows the experimentally obtained gap width between the carbon fiber and the wall of the holes versus the pulse duration. The error of the gap width was estimated to be about 200nm by drilling a few holes with the same parameters. There is an exception of the data point at 10 ns pulse duration, which was derived from the gap

width of the triangle shown in Fig. 4.15 (a). The figure indicates that the gap width is almost linearly dependent on the pulse duration, as expected from the simple approximation of the charging time constant of the double layer, as discussed in chapter 2.

The specific electrolyte resistance of 1M LiCl/DMSO is about  $150\Omega\cdot\text{cm}$  (see Fig. 4.6) and the double layer capacitance of gold in 1M LiCl/DMSO is about  $50\mu\text{F}\cdot\text{cm}^{-2}$  at 0.1V (see Fig. 4.5). Base on these parameters, a charging time constant  $\tau$  of the double layer at Au/DMSO interface can be estimated to be 750ns for a separation of  $1\mu\text{m}$  between the gold and the carbon fiber. The employed pulse durations between 20ns and 100ns are much shorter than the charging time constant of 750ns. This is why the sub-micrometer gap widths can be achieved with a few 10ns long voltage pulses. In contrast, the specific electrolyte resistance of 1M LiCl in water is about  $13\Omega\cdot\text{cm}$  (see Fig. 4.6). The double layer capacitance of Au(111) in 0.1M KCl aqueous electrolyte is about  $40\mu\text{F}\cdot\text{cm}^{-2}$  at 0.4V vs. SCE (saturated calomel electrode)<sup>[118]</sup>. To achieve a charging time constant of 750ns for a double layer at Au/aqueous chloride solutions, a separation of  $14\mu\text{m}$  between the tool and the gold is required. Therefore, the machining precision is improved roughly by one order of magnitude due to the high specific electrolyte resistance of 1M LiCl/DMSO.



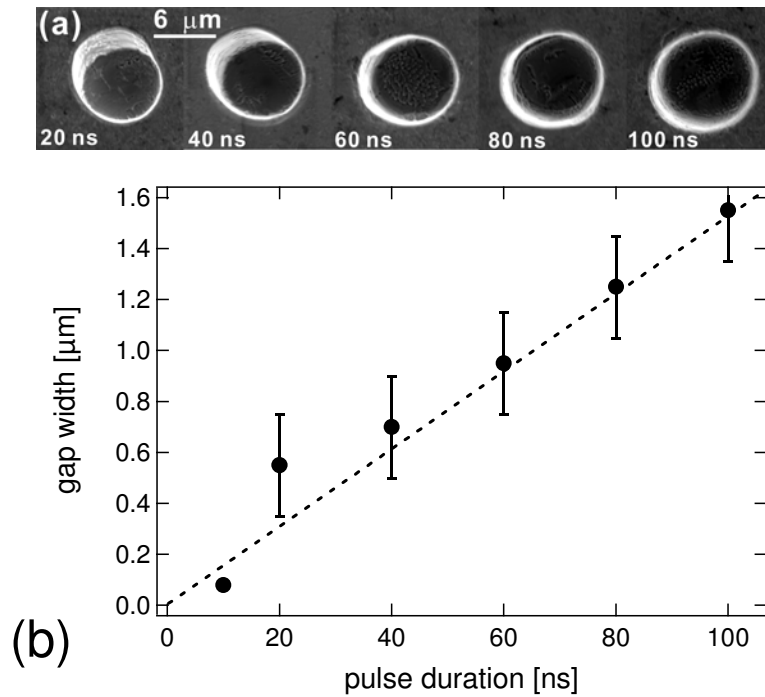


Fig. 4.11. (a) SEM images of 10 $\mu$ m deep holes drilled in Au in 1M LiCl/DMSO with varying pulse duration. Other parameters:  $\Phi_{\text{Au}}=0.1\text{V}$ ,  $\Phi_{\text{tool}}=0.8\text{V}$ , pulse amplitude: 3V, machining time: 100min per hole, were kept unchanged; (b) Plot of gap width between the tool and the workpiece, i.e., machining precision vs. pulse duration. With the exception of the data point at 10ns pulse duration, the data was derived from the hole in Fig. 4.15 (a). This figure was adopted from our recent publication<sup>[102]</sup>.

#### 4.2.2.2 Influence of pulse amplitude

Fig. 4.12 (a) shows SEM images of a series of 10 $\mu$ m deep holes drilled in an Au foil in 1M LiCl/DMSO with varying pulse amplitudes from 3.0V to 5.6V. The rest of the machining parameters remained constant. The bottom of the holes shown in Fig. 4.12 (a) is very flat. The diameter of the holes increased from 8.1 $\mu$ m to 10.2 $\mu$ m with increasing pulse amplitude from 3.0V to 5.6V. As shown in Fig. 4.12 (b), the gap width almost linearly varies with the pulse amplitude. Thus both pulse duration and amplitude determine the localized polarization amplitude of the double layer of gold and the consequent machining precision. As described in chapter 2, both double layers, at workpiece/electrolyte interface and tool/electrolyte interface, which are connected

in series via the electrolyte resistance, are charged by the pulses. The charging amplitude of the double layers upon application of voltage pulses is inversely proportional to the respective capacitances. The double layer capacitance of a polycrystalline gold electrode in 1M LiCl/DMSO was determined to be about  $50\mu\text{F}/\text{cm}^2$  at 0V (see Fig. 4.5). However, we did not succeed in measuring the double layer capacitance of a single carbon fiber, since its surface area was quite small and it was difficult to measure the small ac components in ac voltammetry. Double layer capacitances of graphite and carbon between  $3\mu\text{F}\cdot\text{cm}^{-2}$  and a few  $10\mu\text{F}\cdot\text{cm}^{-2}$  were reported, dependent on the surface state of electrodes and the composition of electrolytes<sup>[122, 123]</sup>. Most reported double layer capacitances of carbon, e.g., the double layer capacitances of glassy carbon of about  $15\mu\text{F}\cdot\text{cm}^{-2}$  in various concentrated electrolytes<sup>[122]</sup>, are significantly lower than the double layer capacitance of gold of  $50\mu\text{F}\cdot\text{cm}^{-2}$  in 1M LiCl/DMSO. Hence the double layer at Au/DMSO interface is expected to be polarized only by a small fraction of the applied pulse amplitude. This is the reason that relatively high pulse amplitudes (typically  $\geq 3.0\text{V}$ ) are necessary for successful machining of gold.

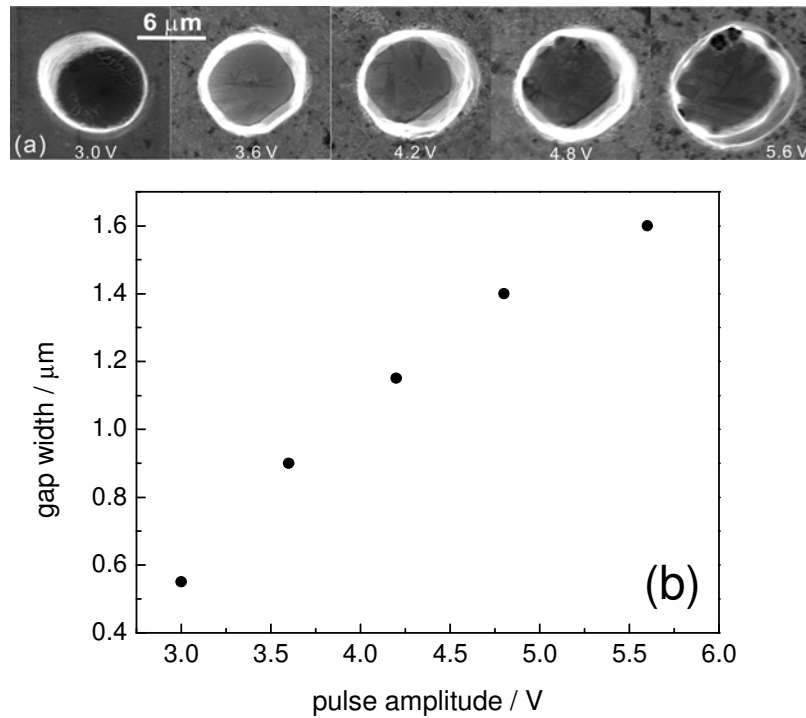


Fig. 4.12. (a) SEM images of 10 $\mu$ m deep holes drilled in Au in 1M LiCl/DMSO with varying pulse amplitudes. Other parameters:  $\Phi_{Au}=0.1V$ ,  $\Phi_{tool}=0.8V$ , pulse duration: 20ns, machining time: 100min per hole, remained constant; (b) Plot of gap width between the tool and the wall of the holes versus the pulse amplitude.

### 4.2.2.3 Influence of rest potential of gold

Since the double layer capacitance of the carbon fibers is unknown, we can not calculate the polarization amplitude of the double layer at gold surface exactly. Additionally, the polarization of the double layer of gold upon application of the pulses is relative to its rest potential. Hence, the maximum polarization of the gold workpiece during the pulses on an absolute scale with respect to the reference electrode, are coupled to the rest potential. Hence, in addition to the pulse parameters (duration and amplitude), the rest potential of gold is a critical parameter. In order to estimate the polarization amplitude of gold surface upon voltage pulses and the influence of the rest potentials, a series of 10 $\mu$ m deep holes were drilled by application of 4.2V, 100ns pulses with varying rest potentials from -50mV to 150mV versus a Pt wire quasi-reference electrode. The drilling rate was kept constant (45min

for 10 $\mu$ m depth). In order to avoid the slow corrosion of the gold substrates in solutions, the rest potential of gold should be adjusted to the lowest possible potential, before gold re-deposition would occur. This is why we set the rest potentials of gold range between -50mV and 150mV. SEM images of the holes are shown in Fig. 4.13 (a) as well as a plot of the gap width versus the rest potentials (Fig. 4.13 b). It should be noted that upon drilling the hole with the lowest rest potential (-50mV, left hole of Fig. 4.13 a), the feed rate of the carbon fiber was slightly higher than the dissolution rate of the gold substrate, which resulted in frequent electric contact between the tool and the gold substrate. To avoid a wide-range anodic corrosion, the carbon fiber tool was slightly retracted by a few micrometers upon such a contact, before the drilling process was continued. The frequent contacts signaled that the dissolution of gold was very slow under those machining condition and the polarization of the gold workpiece by the pulses with respect to -50mV rest potential was only slightly exceeding the onset potential of gold dissolution. After slightly increasing the rest potential to 0 mV, no contact was detected in the process of drilling, which indicated that the dissolution of gold was faster than the drilling speed. This is because, under charge transfer controlled conditions, the dissolution rate of the gold is exponentially dependent on the overpotential (according to the Butler-Volmer equation<sup>[45]</sup>), and the dissolution rate rapidly increased with the positive shift of the rest potential and the effective increase of the overpotential. At 0V rest potential, a gap width of about 0.25 $\mu$ m was achieved even by application of the 4.2V, 100ns voltage pulse train, since the polarization of the gold during the pulse train, adding to the rest potential of 0V, just slightly exceeded the onset potential of dissolution. This also demonstrates that the maximum polarization amplitude of the gold surface by a 4.2V, 100ns voltage pulse is in the order of a few 100mV. The gap width rapidly increased from 0.25 $\mu$ m to 1.8 $\mu$ m with increasing rest potential from 0mV to 150mV. This indicates that the machining precision is very sensitive to the rest potential of the gold substrate. Thus, to achieve high machining precision and to suppress the significant corrosion of gold as well as the re-deposition of the dissolved gold, the rest potential of gold is usually chosen between 0 and 100mV for achieving considerable machining rates.

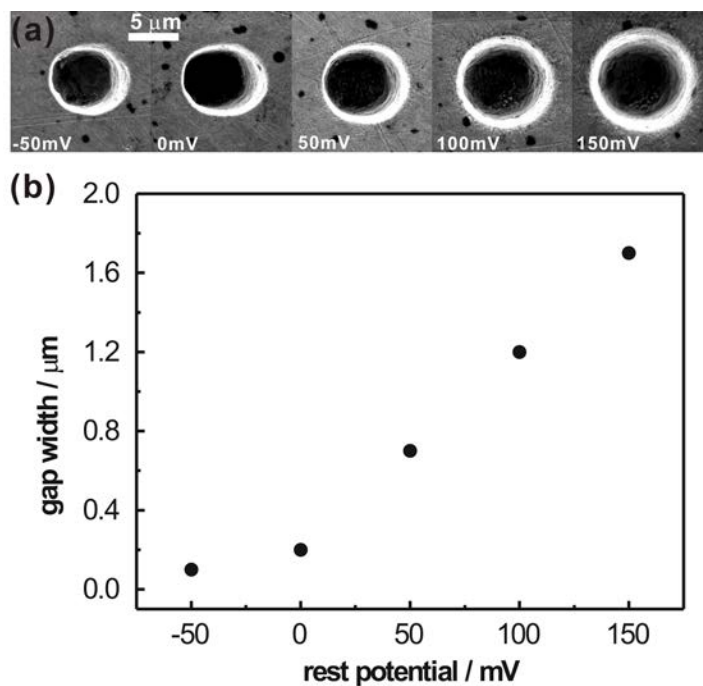


Fig. 4.13 (a) SEM images of 10µm deep holes drilled in an Au foil in 1 M LiCl/DMSO with 4.2V, 100ns pulses. The rest potential of the Au workpiece varied between -50mV and 150mV; (b) Dependence of the gap width between the tool and the hole versus the rest potentials. This figure was adopted from our recent publication<sup>[124]</sup>.

#### 4.2.2.4 Influence of water content

The effects of water content in the water-DMSO mixtures on the electrochemistry of gold have already been discussed in detail in section 4.1. Herein, the influence of the water content on the electrochemical machining of gold is studied also by drilling a series of 10µm deep holes in 1M LiCl/DMSO-water with varying water content from 0% to 50%, as shown in Fig. 4.14. The holes were drilled with 3V, 50ns pulses. The machining time for each hole was 40min and the other machining parameters were kept constant. The diameter of the holes changes with the water content in the mixtures. The hole drilled in a mixture containing 10% water is slightly smaller than the hole drilled in pure DMSO solution. Since the specific electrolyte resistance and the double layer capacitance remain approximately constant in DMSO rich mixtures, the decreasing diameter of the hole is attributed to the positive shift of the dissolution

onset potential in 10% water containing mixture in comparison with pure DMSO (see Fig. 4.3). From the above discussion, it follows that, the pulses polarize the double layer of gold by a few 100mV and the machining precision is very sensitive to the rest potential of gold, i.e., the resulting effective overpotential. Even a small positive shift of the onset potential of dissolution would considerably lower the effective overpotential and reduce the gap width. However, the decreasing specific electrolyte resistance and the slightly decreasing capacitance of the double layer for water contents exceeding 20% resulted in smooth increase of the diameter of the holes, as shown in Fig. 4.14.

As indicated in Fig. 4.3, the electrochemical potential window of gold dissolution/deposition decreases with increasing water content. With 20% water, the cathodic peak shifted positively by about 250mV to -0.5V. However, no significant effect on the drilling process and no re-deposition of the dissolved gold at the bottom of the hole were observed. In the solutions with more than 30% water content, the influence of the further narrowed electrochemical potential window upon increasing water content is indicated by the gold particles deposited at the bottom of the holes (see Fig. 4.14). In 50% water content solution, strong re-deposition of gold was observed at the wall and the bottom of the hole. Two factors contributed to the deposition of spongy gold inside the hole drilled in 50% water mixture. One was the easy reduction of dissolved gold and the other was the high dissolution rate of gold in 50% water mixture. The deposition of the spongy gold in the gap led to frequent contacts during the drilling process.

In our experiments, the LiCl was not further dried before use. Additionally, during the machining experiments, the electrochemical cell was exposed to air for a few hours and a small amount of water from environment would be absorbed by pure DMSO. However, no significant influence of this probably small amount of water on machining process was observed. Actually, we can be benefit from the improvement of the machining precision upon addition of 10%-20% water, though this is at expense of a slightly decreasing electrochemical potential window in those solutions, which renders the choice of the rest potential of gold to avoid the corrosion and re-deposition.

An equivalent but more conveniently way to achieve an improvement of the machining precision is by direct adjustment of the rest potential of the gold.

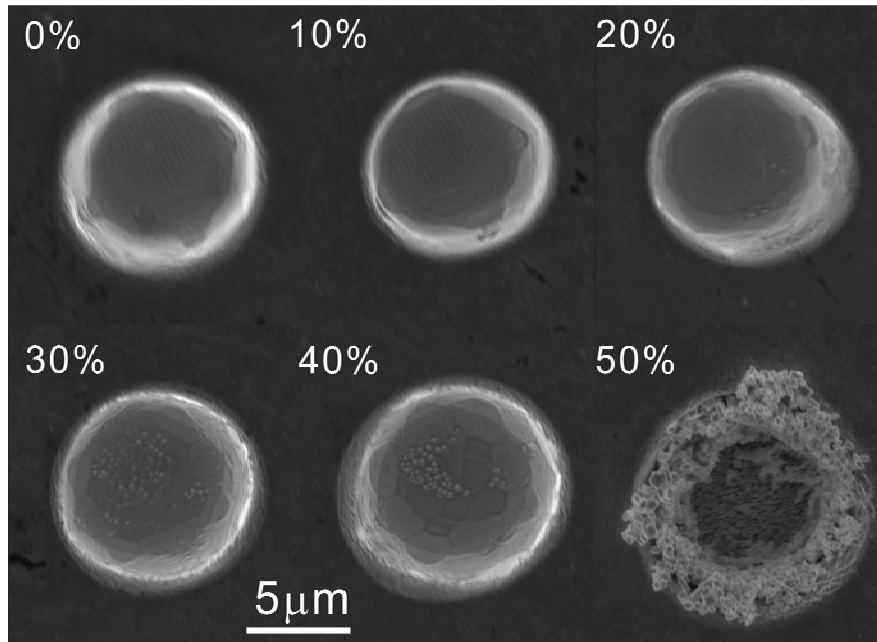


Fig. 4.14 SEM images of 10 $\mu$ m deep holes drilled in Au in 1M LiCl in (100-x)% DMSO + x% H<sub>2</sub>O solution. Pulse duration: 50ns, amplitude: 3.0V,  $\Phi_{Au}=0V$ ,  $\Phi_{tool}=1.0V$ , machining time: 40min per hole. This figure was adopted from our publication<sup>[102]</sup>.

#### 4.2.2.5 Fabrication of gold micro- and nanostructures

The machining parameters for machining of gold micro- and nanostructures like pulse duration, pulse amplitude, rest potentials of gold and carbon fiber were adopted with help of the above experiments, i.e., the investigations of “standardized” drilling of holes with a  $\phi 7\mu$ m carbon fiber. Many gold micro- and nanostructures were fabricated in the course of this work (see chapter 5). Here two typical structures are presented as examples to demonstrate the capability for fabrication of gold nanostructures. Fig. 4.15 (a) shows two 500nm deep triangles which were machined with 4.2V, 10ns and 3.6V, 15ns pulses, respectively. In analogy to a miniature milling cutter in conventional milling, firstly, a 500nm deep hole was vertically drilled into a gold foil,

then followed a lateral movement of the tool along a triangular path. The machining time for each triangle was about 45min. The width of the trough of the triangle, fabricated using 4.2V, 10ns pulses, was about 260nm and the gap was about 80nm wide. The width of the trough machined with 4.2V, 10ns was slightly smaller than that machined with 3.6V, 15ns. High amplitude short duration pulse trains achieve a high machining precision. As a benefit from the high specific resistance of 1M LiCl in DMSO, pulses with duration of the order of 10ns are sufficient to achieve a 100nm machining precision, i.e., gap width. To obtain a similar machining precision for Ni in 0.2M HCl aqueous solutions, much shorter pulses of the order of 500ps were required<sup>[43]</sup>, which is far from routine. The capabilities for machining three dimensional, high aspect ratio nanostructures are demonstrated by a 2x2 array of Au pillars, as shown in Fig. 4.15 (b). The pillar array was machined with 4.2V, 20ns pulses. In order to achieve a considerable machining rate, the rest potential of the gold was set to 0.1V, at the expense of a wider gap width. The machining rate was about 0.6 $\mu$ m/min and it took about 1 hour to complete the structure. Similar to the machining of the triangles, a 4.5 $\mu$ m deep hole was first vertically drilled into a gold foil, and then followed a lateral movement of the tool to obtain the pillar array. The trough is about 1 $\mu$ m wide and about 4.5 $\mu$ m deep. The aspect ratio is about 4.5. The side walls of the troughs are remarkable flat and also the edges of the pillars are sharp with radii of curvature below 100nm. Since the rest potential of gold was 0.1V, minor corrosion of surface was observed. However, the corrosion can be effectively avoided by proper choice of the rest potential of gold.



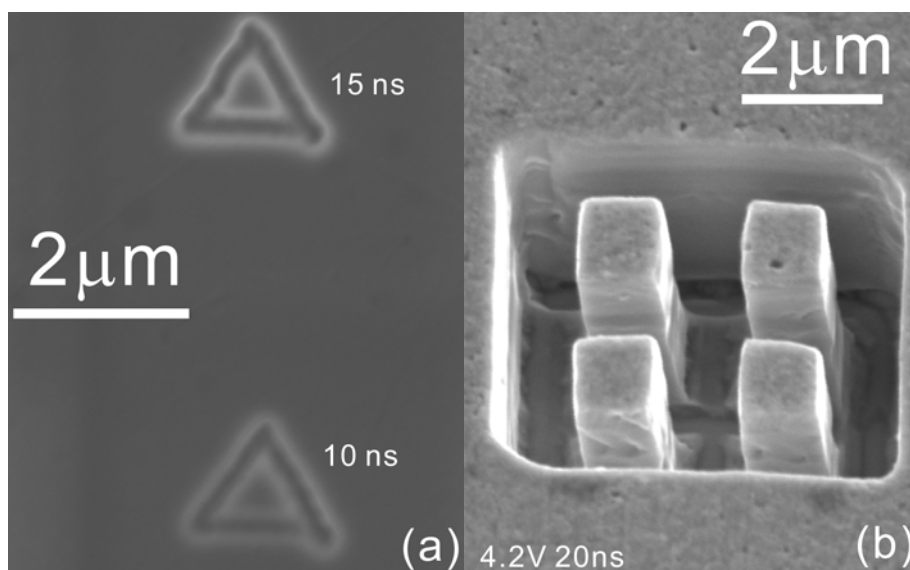


Fig. 4.15 SEM images of the microstructures machined in an Au foil in 1M LiCl/DMSO solution, (a) Triangles, 500nm deep, machined with 4.2V, 10ns pulses and 3.6V, 15ns pulses,  $\Phi_{\text{Au}}=0\text{V}$ ,  $\Phi_{\text{tool}}=0.8\text{V}$ , machining time: 45 min; (b) Au-pillars, 4.5 $\mu\text{m}$  high, machined with 4.2V, 20ns pulses,  $\Phi_{\text{Au}}=0.1\text{V}$ ,  $\Phi_{\text{tool}}=1\text{V}$ , machining time: 60 min. The images were adopted from our recent publication<sup>[102]</sup>.

### 4.3 Conclusions

Nonaqueous solution, here LiCl/DMSO, was successfully employed for the electrochemical micromachining of gold. In the electrochemical studies, no passivation layer on gold surface was observed even with applied potentials as high as 1.8V. Because of the high activity of  $\text{Cl}^-$  and the high stability of  $[\text{AuCl}_2]^-$  in DMSO,  $[\text{AuCl}_2]^-$  is the predominant dissolution product of gold in LiCl/DMSO and the reduction of  $[\text{AuCl}_2]^-$  requires rather negative potentials as observed. Therefore, the gold dissolution/deposition exhibits a strongly irreversible behavior in LiCl/DMSO and the electrochemical potential window of gold dissolution/deposition in LiCl/DMSO is as wide as 800mV. As a benefit from the considerably wide electrochemical window, the rest potentials of gold in machining experiments, ranging between 0 and 100mV, are easily determined to effectively avoid the strong corrosion of gold workpiece and the re-deposition of dissolved gold. The stability of  $[\text{AuCl}_2]^-$

and the electrochemical potential window of gold dissolution/deposition decrease with increasing water content in DMSO-water mixtures.

The machining parameters like pulse duration, pulse amplitude, rest potential of gold workpiece and the water content in the mixtures, were investigated in detail by fabrication of holes with a  $\phi$  7 $\mu$ m carbon fiber. Linearly increasing gap width with increasing pulse duration was observed, as theoretically expected. Due to the low specific conductivity of 1M LiCl in DMSO, about 1/10<sup>th</sup> of that of 1M LiCl in water, sub-micrometer machining precisions were achieved with moderate pulse durations of the order of 10ns. No significant influence of up to 20% water in DMSO on the machining of gold was observed, signalling that the small amount of water absorbed from the environment due to the exposure of the electrochemical cell to air for a few hours was acceptable. Electrochemically etched carbon fiber tips are suitable tools for reproducible fabrication of high aspect ratio three dimensional structures. A 2x2 array of Au pillars with 4.5 aspect ratios milled into a gold foil demonstrates the capabilities of fabrication of three dimensional gold microstructures.

# Chapter 5 Cathodoluminescence of gold nanostructures

By using a highly focused electron beam, surface plasmons can be locally excited with very high spatial resolutions. If momentum conservation is fulfilled, the de-excitation of the surface plasmons would lead to radiation of light. Hence the spatial distribution and resonant frequencies of surface plasmons, excited e.g., at metallic nanostructures, can be revealed from their radiation in far field. In this chapter, we use cathodoluminescence, i.e., the radiation of light upon irradiation with electrons, to investigate the optical properties of the electrochemically machined gold micro- and nanostructures as well as of silver particles. The spatial intensity distribution of light emitted from the electrochemically machined gold structures is studied by photon maps, in addition to the spectral measurements. The emission angles of the emitted light are revealed by angularly resolved measurements.

## 5.1 Electron-specimen interactions

Characterization of carbon fiber tools, fabricated Au structures, Au and Ag tips, as well as the subsequent optical characterization of Au and Ag nanostructures, is carried out in a Hitachi model S570 scanning electron microscope (SEM), which is equipped with a LaB<sub>6</sub> electron gun with a maximum operation voltage of 30kV. Therefore, here a brief introduction of the possible electron-specimen interactions is necessary. Many signals, e.g., secondary electrons, backscattered electrons, Auger electrons, x-Ray, cathodoluminescence and heat, are generated in the process of elastic and inelastic scattering of primary electrons by a specimen<sup>[125]</sup>. The penetration range of the primary electrons into the specimen  $R$  ( $\mu\text{m}$ ) is dependent on the energy of the primary electrons and the properties of the specimen, which can be estimated by equation 5.1<sup>[126]</sup>:

$$R(\mu\text{m}) = 2.76 \times 10^{-2} AE^{1.67} / (\rho Z^{0.89}). \quad (5.1)$$

In equation 5.1,  $A$  is the atomic weight of the specimen in g/mol,  $\rho$  is the density of the specimen in g/cm<sup>3</sup>,  $Z$  is the atomic number of the specimen and  $E$  is the energy of the primary electrons in keV. Equation 5.1 is valid from a few keV up to 1000keV. The formation of secondary electrons, i.e., the generation of low energy electrons leaving the specimen surface with energy less than 50eV<sup>[125]</sup>, is important to provide surface topographical information, since the secondary electron yield is dependent on the surface tilt angle and the surface composition. Compared to optical microscope, the secondary electron (SE) images provide higher spatial resolution and higher depth of field due to the small spot size of the primary electron beam and the small aperture of the scanning electron microscope. Thus, most of our fabricated structures are characterized with SE images. Another kind of signal produced by the primary electrons, in which we are interested, is cathodoluminescence (CL).

## 5.2 Cathodoluminescence

Generation of light by bombardment with electrons, generally called cathodoluminescence, is the working principle of the cathode ray tubes in televisions and traditional computer monitors, in which intensive light is generated by electron irradiation of phosphorescent materials<sup>[127]</sup>. In the field of material science and geology, cathodoluminescence is widely used to study the physical properties of semiconductors and minerals<sup>[128, 129]</sup>. The basic mechanism of cathodoluminescence for semiconductors and insulators is the recombination of electron-hole pairs, which are generated by impinging electrons. However in metals, the nonradiative relaxation channels for hot electrons are much faster than the radiative relaxation and light emission due to the recombination of electron-hole pairs is only a minor contribution to the overall intensity of cathodoluminescence for metals<sup>[74]</sup>. For example, photoluminescence efficiency of the order of  $10^{-10}$  was observed from smooth gold surfaces<sup>[130, 131]</sup>, due to the very fast nonradiative channels for the hot electrons<sup>[130-132]</sup>. In contrast to the main luminescence mechanism of most semiconductors, i.e., the recombination of electron-hole pairs, there are several possible radiation mechanisms

for metals which all would contribute to the overall light intensity upon bombardment with electrons. There are Cherenkov radiation, Bremsstrahlung (braking radiation), transition radiation and radiative decay of excited surface plasmons and bulk plasmons<sup>[74, 125]</sup>.

### 5.2.1 Cherenkov radiation<sup>[133]</sup>

A charged particle which moves with a uniform velocity along a straight trajectory in vacuum does not radiate. However, radiation would occur when the high energy charged particles, e.g., electrons, travel through a dielectric medium with a velocity greater than the phase velocity  $c/n(\omega)$  of light in such a dielectric medium, ( $c$  is velocity of light in vacuum and  $n(\omega)$  is frequency dependent refractive index of the medium). This type of radiation was first discovered by Cherenkov in 1934 and then named after him. The Cherenkov radiation is emitted at a specific angle which is dependent on the velocity of the charged particles and the phase velocity of light. Since the characteristic emission angle of Cherenkov radiation is related to the velocity of the charges, it is usually used for measuring the velocities of high energy particles in particle physics. The spectrum of Cherenkov radiation is continuous without any characteristic peak, which is given by Frank-Tamm formula<sup>[133, 134]</sup>:

$$\left(\frac{dE}{dx}\right)_{\text{rad}} = \frac{(ze)^2}{c^2} \int_{v > (c/\sqrt{\epsilon(\omega)})} \omega \left(1 - \frac{c^2}{v^2 \epsilon(\omega)}\right) d\omega, \quad (5.2)$$

where  $\left(\frac{dE}{dx}\right)_{\text{rad}}$  represents the emitted energy per unit length the charged particle traveled;  $ze$  is the electric charge of the particle;  $v$  is the velocity of the charged particle and  $c$  is the velocity of light in vacuum;  $\epsilon(\omega)$  represents the frequency dependent dielectric constant of the dielectric medium.

In our measurements, a 15keV electron beam is usually used. The velocity of an electron with energy of 15keV is about  $0.237c$ , where  $c$  is the velocity of light in vacuum. The frequency dependent refractive index  $n(\omega)$  of gold is less than 1.7 between near ultra violet (UV) and near infrared spectral regime<sup>[83]</sup>. Hence, the

velocity of the electrons with energy of 15keV is much lower than the phase velocity of light in gold in this spectral regime. Therefore, Cherenkov radiation gives no contribution to the observed light in our experiments.

## 5.2.2 Bremsstrahlung and Transition Radiation

Charged particles, e.g., electrons, impact on a specimen and undergo acceleration by the coulomb interaction with the nuclei. The accelerated charged particles radiate light<sup>[133]</sup>. Since such radiation was first observed in the process of deceleration of high energy electrons by a metal target, it is called Bremsstrahlung or braking radiation<sup>[135]</sup>. Bremsstrahlung appears as x-Ray continuum<sup>[125]</sup>. The intensity of Bremsstrahlung can be estimated by Kramers' equation<sup>[135]</sup>:

$$I(E) = KZ \frac{E_0 - E}{E}, \quad (5.3)$$

where K is the Kramers' constant of  $2 \times 10^{-9}$  photons  $s^{-1}$   $eV^{-1}$  electron<sup>-1</sup><sup>[136]</sup>; Z is the atomic number of the target material;  $E_0$  is the energy of primary electrons and E is the energy of the emitted photons.

According to Kramers' equation, the emission intensity diverges as the photon energy vanishes. However, the intensity of the experimentally observed x-Ray continuum is close to 0 in the long wavelength range. Kramers' equation is invalid at low energies<sup>[135]</sup>. The penetration range of the primary electrons increases with increasing initial energy of the primary electrons. Radiation would be induced in each collision in the process of multiple collisions between the primary electrons and the medium. However the optical attenuation depth of light decreases with increasing wavelength and becomes much smaller than the penetration range of the electrons. The optical absorption and the reflection of the emitted light by the medium before it escapes from the medium surface lead to very low emission intensity of Bremsstrahlung at long wavelengths<sup>[137, 138]</sup>, i.e., for the visible light. Generally, grazing incidence of electrons produces much higher photon intensity than normal incidence, since a larger number of photons can escape from the medium surfaces for the grazing incidence<sup>[88]</sup>.

When electron passes across an interface between two dielectric media with different dielectric permittivities, a dipole is formed at the interface between the two dielectric media by the incident electron and its corresponding image charge. Radiation due to the annihilation of the incoming electron and its induced image charge is called transition radiation<sup>[139]</sup>. In addition to Bremsstrahlung, transition radiation is simultaneously generated upon high energy electron irradiation of metals. Transition radiation is expected to be transverse magnetic (TM or P) polarized, was first described by Frank and Ginzburg in theory<sup>[139]</sup>. The angular spectral intensity distribution of transition radiation on a medium 1 side upon normally incident electrons was given by Ter-Mikaelian by solving the radiation field<sup>[140]</sup>, as expressed by equation 5.4:

$$\frac{dI_1(\mathbf{n}, \omega)}{d\omega d\Omega} = \frac{e^2 v^2 \epsilon_1^{1/2} \sin^2 \theta \cos^2 \theta}{\pi^2 c^3} \times \left| \frac{(\epsilon_2 - \epsilon_1)(1 - \beta^2 \epsilon_1 + \beta \sqrt{\epsilon_2 - \epsilon_1 \sin^2 \theta})}{(1 - \beta^2 \epsilon_1 \cos^2 \theta)(1 + \beta \sqrt{\epsilon_2 - \epsilon_1 \sin^2 \theta})(\epsilon_2 \cos \theta + \sqrt{\epsilon_1 \epsilon_2 - \epsilon_1^2 \sin^2 \theta})} \right|^2. \quad (5.4)$$

$\beta=v/c$  is the ratio of the velocity of electron to the velocity of light in vacuum;  $\epsilon_1$  and  $\epsilon_2$  are the frequency dependent dielectric constant of the two media;  $\theta$  is the light emission zenith angle. The radiated energy of transition radiation is dependent on the velocity of the electrons and the dielectric properties of the two media. High energy electrons passing across the interface of two media with large dielectric difference will produce high intensity transition radiation<sup>[140]</sup>. According to the equation 5.4, the angular spectral distribution of transition radiation can be plotted if the dielectric properties of the two media are known. For the angular distribution of transition radiation with a wavelength of 600nm from an Au surface, produced by a 200keV electron beam was plotted, see Fig. 22 in a recent review<sup>[74]</sup>. Generally, the angular intensity distribution of transition radiation shows a butterfly shape, which is approximately given by  $\sin^2 \theta \cos^2 \theta$ <sup>[141]</sup>, neglecting the dielectric properties of the two media. The angular distribution of transition radiation given by  $\sin^2 \theta \cos^2 \theta$  was also sketched in reference<sup>[141]</sup>.

Both, Bremsstrahlung and transition radiation would contribute to the observed light upon the irradiation of flat metal surfaces with electrons. Transition radiation is p-polarized and Bremsstrahlung is unpolarized<sup>[142]</sup>. Therefore, measurements of the polarization of the emitted light can separate transition radiation from Bremsstrahlung<sup>[142]</sup>. Alternatively, grazing incidence of electrons can decrease the ratio of transition radiation to the overall emission intensity<sup>[88]</sup>. Thirdly, the optical yield due to Bremsstrahlung and due to transition radiation is dependent on electron energy. As mentioned above, due to the large optical absorption efficiency of metals for long wavelength light, through Bremsstrahlung could be induced during electron penetration (volume effect), its contribution to the observed light just comes from the skin of metal surfaces, dependent on the optical attenuation depth of the light. The penetration range of the electrons increases with increasing electron energy, in the case when the electron penetration range is much larger than the optical attenuation depth of light, the intensity of Bremsstrahlung is approximately proportional to the  $(1-\beta^2)/\beta^2$ , where  $\beta = v/c$ , the ratio between the velocity of the electrons and the velocity of light in vacuum<sup>[88, 142]</sup>. If the energy  $E$  of the incident electrons is much smaller than the rest mass electron energy  $E_0$  ( $E_0=511\text{keV}$ <sup>[125]</sup>), Bremsstrahlung is approximately proportional to  $1/E$ <sup>[88]</sup>. In contrast, transition radiation is nearly proportional to the primary electron energy<sup>[140]</sup>. By exploring these properties, the contribution of transition radiation and the contribution of Bremsstrahlung to the overall emission intensity can be separated (see also section 5.3).

### 5.2.3 Radiative plasmons<sup>[1]</sup>

The excitation of bulk plasmons and surface plasmons by electrons has been described in detail in chapter 2. Excited bulk plasmons could be radiative. However, the light upon radiative decay of bulk plasmons is in the UV spectral regime for most metals<sup>[69]</sup>. Surface plasmons excited on smooth metal surfaces are nonradiative, due to impossible conservation of momentum between light and propagating surface plasmons. Under specific conditions, e.g., scattering by surface defects or a grating,



the momentum conservation is fulfilled and the propagating surface plasmons become radiative. In contrast, localized surface plasmons excited on the metallic nanoparticles, voids, and nanostructures are efficiently radiative<sup>[74]</sup>.

### 5.3 Cathodoluminescence of smooth silver and gold surfaces

From the above discussion, the possible contributions to cathodoluminescence upon irradiation of metals with relatively low energy electrons (less than 50keV) are Bremsstrahlung, transition radiation, radiative bulk plasmons, radiative localized surface plasmons, and radiative propagating surface plasmons when the momentum conservation is fulfilled. Silver is an important material for plasmonic applications in the near UV, visible and near-infrared spectral regimes, due to the low internal damping of excited plasmons in these spectral regimes (see chapter 2) and its relatively inert chemical properties. Although the cathodoluminescence of Ag upon electron irradiation with normal and non-normal incidence was studied in detail during the last five decades<sup>[86, 88, 143-146]</sup> and it is well understood, in order to clarify the various possible contributions to the observed light and to estimate the validity of our optical system, we also studied the cathodoluminescence of Ag as a reference. Fig. 5.1 shows the cathodoluminescence spectra from a thick Ag foil upon a 15keV, 3nA electron beam bombardment. A narrow and intense peak at 330nm is shown in the spectrum (black curve) obtained from the mechanically polished Ag surface. The peak position is in accordance with Ag bulk plasmon energy of 3.75eV<sup>[86]</sup>. The optical properties of silver and gold in the wavelength range between 200nm and 1000nm have been described in chapter 2. The imaginary component  $\epsilon''(\omega)$  of the complex dielectric constants is responsible for the internal absorption of plasmons, e.g., damping via generation of electron-hole pairs<sup>[84]</sup>. The small imaginary component  $\epsilon''_{\text{Ag}}(\omega)$  of the complex dielectric constants at the 330nm indicates the low internal absorption of excited bulk plasmons of Ag, which mainly radiated light peaking at

330nm. The intensity rapidly decreases for the light with wavelength longer than 400nm. This indicates that Bremsstrahlung and transition radiation have minor contributions to the observed light for the case of Ag, compared to the radiative bulk plasmons. The surface of the investigated Ag-sample was not perfect due to the minor roughness produced by mechanical polishing. In order to identify the role of surface roughness and surface plasmons, a scratch was made by an operation knife on the mechanically polished Ag surface. Surface defects inside the scratch were micrometer-sized, which were much bigger than the surface roughness on the mechanically polished surface. The spectrum shown in Fig. 5.1 (red curve), was obtained from the electron beam irradiated surface defects inside the scratch. The peak at 330nm is also present in the spectrum recorded from the spot with the surface defects. The peak intensity is just slightly affected by the surface defects and the peak position is independent of the surface defects. This demonstrates that the radiation of the excited bulk plasmons is almost independent of the surface defects. In addition, intense light in the visible was observed, which directly reflected the contribution of surface plasmons due to the micrometer-sized surface defects. In contrast, the minor surface roughness after polishing did not result in considerable light in the visible, indicating the minor role of the surface roughness upon polishing on the radiation of the surface plasmons. Therefore on the mechanically polished Ag surface no other contributions to cathodoluminescence beside radiation from bulk plasmons was observed; in particular no significant contribution from Bremsstrahlung and transition radiation and from surface plasmons upon the minor surface roughness.

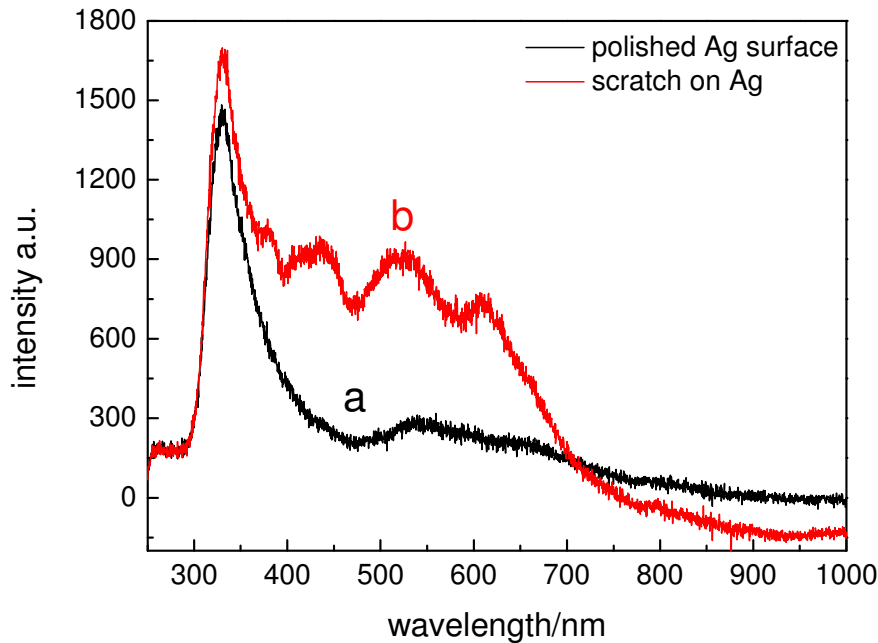


Fig. 5.1 Cathodoluminescence spectra (not normalized to the frequency response of the CCD of the monochromator) obtained from (a) mechanically polished Ag foil surface and (b) from a scratch on the same Ag foil, upon the bombardment with a 15keV, 3nA electron beam. The integration time was 50s for each spectrum.

Gold is another widely used material for plasmonics due to its very good oxidation resistance. Cathodoluminescence (CL) spectra from a 200nm thick Au film evaporated onto a quartz substrate upon 15keV, 20keV and 25keV electron beam bombardment (normal incidence) are shown in Fig. 5.2. The bulk plasmon energy of gold is expected to be between 4.4eV and 9eV<sup>[84]</sup>, which is beyond the spectral region of our monochromator. Therefore the radiation due to the excited bulk plasmons of gold could not be observed. Furthermore, compared to silver, the relatively high imaginary component of the complex dielectric constants of gold  $\epsilon''_{Au}(\omega)$  at the bulk plasmon frequency indicates the strong internal damping of bulk plasmons via, e.g., excitation of interband transitions and the radiative decay of excited bulk plasmons would be strongly suppressed<sup>[84]</sup>. Besides the excitation of bulk plasmons, surface plasmons propagating along the Au/vacuum interface would be also excited by

electrons<sup>[147]</sup>. However, as mentioned above, the propagating surface plasmons have no contribution to the observed light at smooth Au/vacuum interfaces. Therefore, the contributions from bulk and surface plasmons to the spectra in Fig. 5.2 are excluded in the case of Au films.

Transition radiation and Bremsstrahlung were hence the possible contributions to the observed light from the gold film. Comparison of Bremsstrahlung and transition radiation by bombardment of gold films with various energies electrons was studied by Arakawa et al.<sup>[148]</sup>. Since transition radiation is p-polarized and Bremsstrahlung is unpolarized, the contributions of them to CL were separated by polarization dependent measurement of the emitted light. Their results showed that transition radiation played a predominant role upon 100keV electron bombardment and the contribution of Bremsstrahlung became comparable to transition radiation upon the bombardment of low energy electrons with 25keV energy. For a general discussion, the thickness of the gold films should be taken into consideration since the contribution of Bremsstrahlung is dependent on the optical attenuation depth. The thicknesses of the gold films, Arakawa et al. used, were 34nm and 53nm, which were of the order of the optical attenuation depth of gold of about 17nm in the visible<sup>[142]</sup>. In our experiments, the gold structures are typically milled into 100 $\mu$ m thick gold foils whose thickness is much larger than the optical attenuation depth of gold in the visible. In order to clarify the contribution of transition radiation and Bremsstrahlung upon electron beam irradiation of relatively thick samples, spectra of light from a 200nm thick gold film were hence recorded and shown in Fig. 5.2. The intensity of the spectra increases with increasing electron energy. This is contradictory with the prediction of the Bremsstrahlung theory, i.e., the intensity of Bremsstrahlung is inversely proportional to the energy of incident electrons<sup>[88, 138, 140]</sup>. In contrast, the observed spectra nearly follow the energy dependent intensity of transition radiation, i.e., the intensity of transition radiation is proportional to electron energy<sup>[140]</sup>. Therefore, we identify transition radiation as main contribution to the observed cathodoluminescence from the 200nm thick gold film and Bremsstrahlung has just a minor contribution. This conclusion seems to be contradictory to Arakawa et al.'s

results mentioned above, i.e., the contribution of Bremsstrahlung was comparable to the contribution of transition radiation upon 25keV electron irradiation. The contradiction might be due to the different observation angles in the two experiments. Arakawa et al.'s results were recorded at a specific angle of  $30^\circ$  with respect to the surface normal<sup>[148]</sup>. As known from the angular distribution of transition radiation (discussed in detail in chapter 5.6),  $30^\circ$  with respect to the surface normal is not the main emission angle of transition radiation. Hence, the intensity of transition radiation emitted at  $30^\circ$  is relatively low. In contrast, the spectra shown in Fig. 5.2 were collected over a wide opening angle range between  $7^\circ$  and  $85^\circ$ , which included the main emission angle of transition radiation. Beside this, the thickness the gold films Arakawa et al. used was comparable to the optical attenuation depth of visible light, which might increase the contribution of Bremsstrahlung. In conclusion, our results are in accordance with Abajo's statement<sup>[74]</sup>: 'Bremsstrahlung just has a minor contribution to the total photon yield under the normal TEM and SEM operation conditions produced by a normally incident electron beam'.

Furthermore, the spectra shown in Fig. 5.2 in the short wavelength range between 300nm and 550nm are similar to i) theoretically predicted transition radiation spectra<sup>[148]</sup> and ii) experimentally measured spectra obtained by subtraction of the p-polarized light from the s-polarized light<sup>[142]</sup>, though they used impinging electrons with energy higher than 25keV. In the long wavelength range, the spectra shown in Fig. 5.2 are in accordance with van Wijngaarden's measurements<sup>[149]</sup>, i.e., a broad peak between 500nm and 700nm with maximum at around 550nm was observed. According to equation 5.4, the spectrum of transition radiation is related to the frequency dependent dielectric properties of gold, as given by the second term of equation 5.4. The theoretical spectrum of transition radiation of gold between 300nm and 1500nm was plotted in Fig. 23 in a recent review<sup>[74]</sup>, which also shows a minimum at about 480nm and a broad peak at about 550nm, as we observed. In conclusion, transition radiation is ascribed to the main contribution to the emitted light from smooth gold surface irradiated with a few 10keV electrons. Transition radiation is regarded as background in the panchromatic cathodoluminescence images.

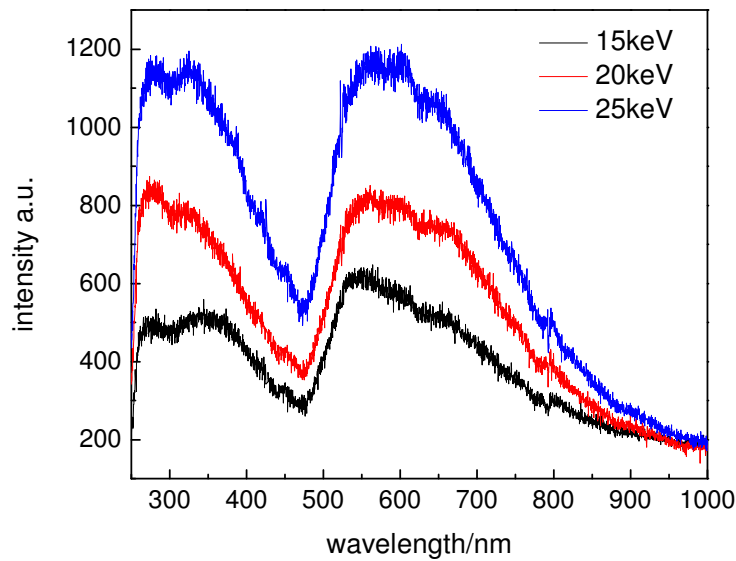


Fig. 5.2 Cathodoluminescence spectra (not normalized to the frequency response of the CCD of the monochromator) obtained from a 200nm thick gold film, evaporated onto a quartz substrate, upon the bombardment with 15keV, 20keV and 25keV, 9nA electron beams. The integration time was 50s.

## 5.4 Panchromatic CL maps of gold structures<sup>[124]</sup>

In surface enhanced spectroscopy<sup>[25]</sup>, surface electromagnetic near field plays a dominant role for the amplification mechanism. Therefore, reproducible preparation of surface electromagnetic field amplification substrates is very attractive for application of surface enhanced spectroscopy<sup>[29]</sup>. The local electromagnetic field distribution can for example be imaged by scanning near field optical microscopy where localized surface plasmons are excited by illumination of light. A resolution of a few 10nm can be achieved, mainly limited by the diameter of the tips. In order to avoid the perturbation of the metal coated tip on the field distribution in scanning near field optical microscopy, in our experiments, surface plasmons are locally excited by a highly focused electron beam. The surface plasmons and the distribution of the accompanying surface electromagnetic field are imaged via the resulting radiation. The light originating from the radiative decay of the locally excited surface plasmons,

adds to the background CL, which is mainly due to transition radiation, as discussed above, resulting in the enhanced emission. Therefore, the intensity of the emitted light is dependent on the electron beam irradiation position, which reflects the spatial distribution of the excited surface plasmons. The resolution is slightly poorer than the diameter of the exciting electron beam, due to the extension of the electric field produced by the electron beam<sup>[74]</sup>.

Cathodoluminescence from metallic nanostructures became a very active research field recently. The surface plasmons modes sustained on various gold nanostructures have been studied via cathodoluminescence<sup>[37-41]</sup>. Most of the investigated gold nanostructures were milled into gold substrates by focused ion beam milling. This technique is quite expensive for nanofabrication and is not universally available. In this thesis, gold micro- and nanostructures were fabricated by ultra-short voltage pulse based electrochemical micromachining method, which is a relatively low cost, mask-less and one step method. The electrochemical micromachining of gold nanostructures was described in detail in chapter 4. Four electrochemically fabricated gold structures and their corresponding panchromatic cathodoluminescence images upon irradiation with a 15keV, 9nA electron beam are shown in Fig. 5.3. The size of the CL images is 256 pixel x 256 pixel. The CL images were recorded with the electron beam slowly scanning across the surface with a residing time of 10ms/pixel. The photons emitted during this period were counted by a photomultiplier whose spectral sensitivity extends from about 300nm to 850nm. The relative intensity distribution for each panchromatic CL image was normalized to the maximum intensity (the maximum counts per 10ms for the images in Fig. 5.3 were between 500 and 1000). As mentioned in chapter 3, shifting the light source, i.e., the area close to the electron irradiated spot, a few 10 $\mu$ m off from the focal point of the parabolic mirror, would lead to a few degrees off-axis tilt of the output beam. This might reduce light intensity due to the blockage of the emitted light along the optical path. In our cases, the electron beam scanning range is usually less than 10 $\mu$ m, thus no significant intensity decrease occurs upon scanning the electron beam.

In comparison with the emission intensity from the flat gold surfaces, strongly

enhanced emission was observed when the electron beam bombarded the gold structures, for example, from the machined Au-structures shown in Fig. 5.3. For an array of Au column, the largest column is about  $3 \times 3 \mu\text{m}^2$  and the smallest is about  $1 \times 1 \mu\text{m}^2$ . The height of the columns is about  $4 \mu\text{m}$ . When the electron beam scanned across the column array, enhanced emission was found upon irradiation of the edges of the columns. The closer the irradiated spot to the edges, the more intense light was emitted. The strongest enhancement of the light emission was found for irradiation positions in close proximity to the edges and the corners. The emission intensity rapidly decreased if the electron beam was located a few 100nm away from the edges. This demonstrates that the ‘sources’ for the enhanced emission are locally confined at the edges of the columns. Although the intensity rapidly decreased from the edges toward the center of the columns, the emission intensity recorded when electron beam rested at the center of the columns, was still slightly higher (10%-20%) than the emission intensity obtained at the unstructured gold surface. As discussed above, there are several possible contributions to the observed light upon electron irradiation of the metals, i.e., transition radiation and radiative decay of plasmons (bulk plasmons and surface plasmons). The bulk plasmons of gold have minor (or no) contribution to the overall intensity due to the strongly internal damping. Therefore, the enhanced emission on the gold structures, in comparison with that from the unstructured gold surfaces, can be attributed to radiative surface plasmons, including radiative propagating surface plasmons and radiative localized surface plasmons. Localized surface plasmons are typically excited on curved metal surfaces, e.g., metallic nanoparticles and voids, and are strongly confined to a small volume<sup>[12]</sup>. In contrast, propagating surface plasmons are typically excited at flat metal/dielectric interfaces and can extend up to about  $10 \mu\text{m}$  from the excitation location, dependent on the wavelength<sup>[12]</sup>. The propagation length of surface plasmon with 550nm wavelength, excited on gold films by a 30keV electron beam, was determined to be a few 100nm, while the propagation length of surface plasmon with 600nm wavelength was determined to be about  $3 \mu\text{m}$ <sup>[150]</sup>. The peak position of the emitted light upon the electron beam irradiation of the center of the column was around 600nm (spectrum is



not shown here, refer to the color of the emitted light in Fig. 5.9). Thus, the propagating length of the surface plasmons excited at the center of the column is comparable to the size of the column. Additionally, edges are very good light emitters due to scattering of propagating surface plasmons into the far field rather than good surface plasmons reflectors<sup>[151, 152]</sup>. Therefore, we ascribe the slightly enhanced emission upon electron irradiation at the center of the rectangular columns to the scattering of propagating surface plasmons at the edges. This is further supported by the grazing emission angle of the red light from an electron beam irradiated Au-bar, as will be discussed later (see Fig. 5.9). Since propagating surface plasmons have a propagation length larger than the size of the columns, the light emitted due to surface plasmons scattered at the edges of the columns should only weakly dependent on the electron irradiation position on the column. Thus, we attribute the strongly enhanced emission upon irradiation near the column edges and corners rather to the effective excitation of localized surface plasmons than to the scattering of the propagating surface plasmons. Similarly, Yamamoto and Suzuki observed enhanced light emission when an electron beam scanned across the edge of a rectangular pad of an Ag film<sup>[153]</sup>. They also ascribed this observation to the excitation of localized surface plasmons at the edge of the Ag film.

When the sizes of the structures were reduced, stronger light emission was found when the beam hit the submicron size structures. The light emitted from a finger like structure (Fig. 5.3 b), where each finger has a size of about  $5\mu\text{m} \times 1\mu\text{m}$ , was enhanced by a factor of 2, compared to the light emitted from the flat surface. The intensity at the end of the fingers was slightly higher than at the other side, where the finger was connected to the flat surface. Further reducing the sizes of the structures, e.g., with the enclosed ridge and triangle shown in Fig. 5.3 (c) and (d), led to enhancement factors up to 2.5. On the other hand, when the electron beam hit the outer edges of the trough forming of the ridge and triangle, the emitted light intensity was just slightly higher than the light from the flat surface. The sub-micrometer gold structures are attributed to be optical antennas<sup>[16]</sup>. Via excitation of localized surface plasmons, the electromagnetic field is strongly 'focused' on the structures which then in turn

efficiently radiate light due to the decay of the excited localized surface plasmons, which resulted in the strongly enhanced emission.

Therefore, the CL images reflect the spatial intensity distribution of the emitted light. The enhanced emission in comparison with the emission from flat gold surfaces, originating from excited surface plasmons, indicates the distribution of the excited surface plasmons and the resulting surface electromagnetic field on the electrochemically fabricated gold structures.

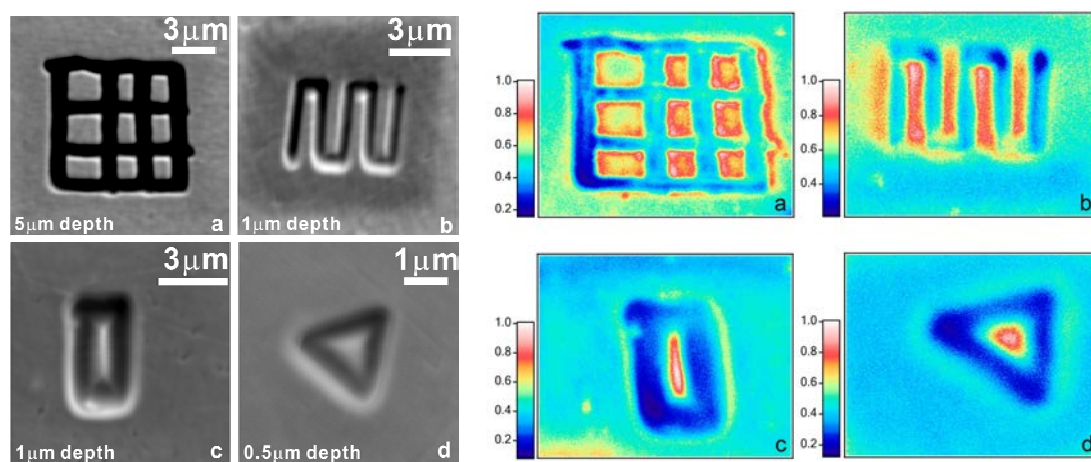


Fig. 5.3 SEM images (left) of gold microstructures machined into a polycrystalline gold foil, (applied machining parameters: (a) 4.2V, 20ns, (b) 5.6V, 10ns, (c) 5.6V, 20ns, (d) 5.6V, 11ns) and their corresponding panchromatic cathodoluminescence (CL) images (right). The maximum intensity of each image was normalized to 1. A 15keV, 9nA electron beam was used to irradiate the structures and the dwell time of the electron beam was 10ms/pixel.

In Fig. 5.4 (a), a 2 x 2 pyramid array is shown. It was obtained by accidentally bending the Au-foil with the 2 x 2 pillar array shown in chapter 4. A 15keV, 9nA electron beam scanned across the pyramid array with a rate of 10ms/pixel to record the CL map (Fig. 5.4 b). The enhancement occurred at the edges of the faces of the pyramids and the apexes of the pyramids. We ascribe the strongly enhanced emission at the apexes to the radiation of the excited localized surface plasmons. Though the troughs of this pyramid array are about 4 $\mu$ m deep and the aspect ratio achieves 3, light

emission when the electron beam hit the bottom of the troughs was even higher than the light emitted from the flat surface. This demonstrates that the light generated at the bottom of the troughs can escape from the troughs, despite the relatively small opening angle. However, it can not be completely excluded that the light was generated at the walls of the pyramids upon bombardment with backscattered electrons from the bottom of the troughs, although the intensity of the backscattered electrons is expected to be small upon the normal incidence of electron beam. Fig. 5.4 (c) shows the spectra of the light emitted from 4 selected locations at the pyramids upon irradiation with the 15keV, 9nA electron beam. The integration time for each spectrum was 50s. As a reference, spectrum 1 (black curve) was obtained from an electron beam irradiated flat gold surface about 5 $\mu\text{m}$  away from the structure. As mentioned above, the propagation length of the surface plasmon with 550nm wavelength was about a few 100nm<sup>[150]</sup>. Hence, 5 $\mu\text{m}$  distance of the irradiation position away from the edge of the structure was sufficient to eliminate contributions of propagating surface plasmons scattered at the structure. As expected, spectrum 1 is almost identical with the spectrum obtained from the 200nm thick gold film (see Fig. 5.2), which has already been discussed in the previous section. A broad peak with maximum around 550nm was observed. The surface roughness of the gold foil upon polishing and electrochemical micromachining has only minor influence on the spectrum. The spectra 2-5 were obtained from the electron beam irradiated apexes of the four pyramids. A broad peak from 480nm to 800nm, peaking at 630nm for each spectrum was observed. For gold, in the visible spectral range with wavelength longer than 550nm, the nonradiative damping of excited surface plasmons, e.g., decay via electronic excitations of electron-hole pairs<sup>[74]</sup>, is small, which is reflected by the imaginary component of the wavelength dependent complex dielectric constants. Therefore, the light originated from localized surface plasmons excited on gold nanostructures usually has wavelengths longer than 550nm. For example, emission peak positions between 550nm to 750nm were observed from gold tips, depending on the geometry of the gold tips<sup>[154]</sup>. Therefore, akin to the apex of gold tips, it is reasonable for the observed light from the apexes of the pyramids peaking at 630nm.

The main difference of the four spectra in Fig. 5.4 (c) is the emission intensity, which is in accordance with the observation of the CL map in Fig. 5.4 (b).

In addition to the precise wavelength distribution measurements with a monochromator, the real color of the pyramids under the irradiation of electrons can be viewed with a color CCD chip, e.g., of a Pentax k100D digital camera. Light emitted from the unstructured gold surface was focused onto the color CCD chip and the recorded image is shown on the left in Fig. 5.4 (d) (for detailed discussion, see chapter 5.6). Light emitted upon irradiation of the apex of one of pyramids was also focused onto the color CCD chip. The recorded image is shown on the right in Fig. 5.4 (d). The unstructured gold surface is green, whereas the apexes of the pyramids are yellow under the electron irradiation. These results are in accordance with the spectral measurements.

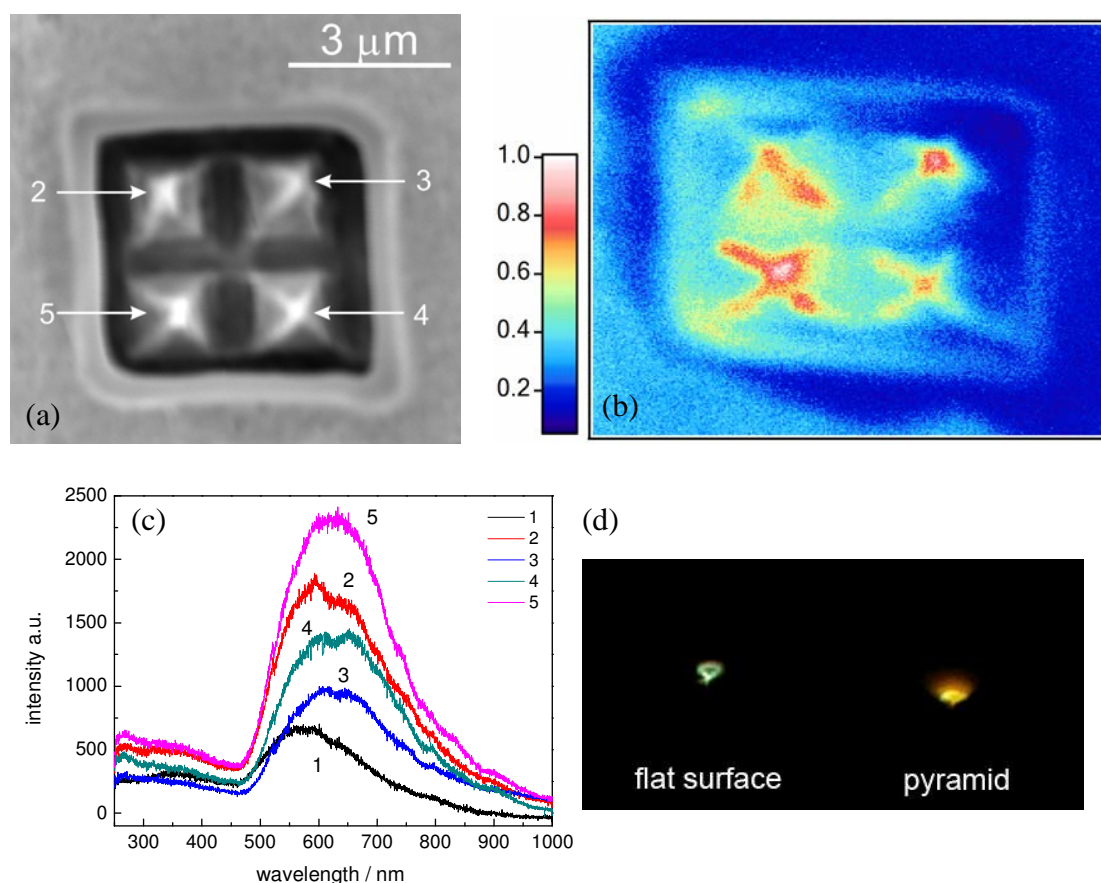


Fig. 5.4 (a) SEM image of an array of Au pyramids; (b) corresponding panchromatic CL image obtained with a 15keV, 9nA electron beam irradiation with a dwell time of 10ms/pxel; (c) spectra 2-5 were obtained from the selected positions indicated in (a) and spectrum 1 was obtained from the flat surface about 5μm away from the structure; (d) Color of the emitted light from the flat gold surface (left) and from the apex of one pyramid (right).

## 5.5 Cathodoluminescence of silver particles

Excitation of localized surface plasmons on Ag particles was investigated by electron energy loss spectroscopy<sup>[34]</sup> as well as by cathodoluminescence<sup>[37, 87]</sup>, where the Ag particles usually had dimensions much smaller than the wavelength of light. The Ag particles we studied had dimensions comparable to the wavelength of the visible light. Triangular Ag particle shown in Fig. 5.5 (a) was deposited on a Si substrate from a molten AgNO<sub>3</sub> film by electron beam irradiation. The sample was provided by Dr.

Halka of our group. The details of the preparation of the Ag particles can be found in reference<sup>[155]</sup>. Si is a perfect substrate for supporting the Ag particles in cathodoluminescence investigations due to its very low optical yield in the visible and near-UV spectral region upon electron irradiation. The corresponding CL image of the Ag triangle upon a 15keV, 3nA electron beam irradiation is shown in Fig. 5.5 (b). The photons were counted with a rate of 5ms/pixel. A strongly enhanced emission spot with a diameter of about 150nm was observed and the emission intensity at this area was about two times higher than that of the rest of the triangle. This non-homogeneous intensity distribution across the triangular Ag particle indicates the non-homogeneous distribution of the excited localized surface plasmons. Fig. 5.5 (c) gives the wavelength distribution of the emitted light upon irradiation of different positions on the Ag triangle. As a reference, the well understood spectrum from flat Ag surface was included in Fig. 5.5 (c). The light emitted from the most intensive position (position 1, indicated in Fig. 5.5 a) also shows the contribution of radiative bulk plasmons, peaking at around 330nm. In addition to this narrow bulk plasmon peak, three broad peaks in the near-UV to visible spectral region, peaking at 365nm, 560nm and 650nm were observed. When the irradiation position shifted a few 100nm away from the intensive spot, e.g., the irradiated position 2 and position 3, the intensities of the peaks at 560nm and 650nm were much lower. This indicates that the emission of the visible light was strongly confined at the most intensive spot. Thus, we ascribe this light to the de-excitation of localized surface plasmons excited by electron beam irradiation of the Ag triangle.

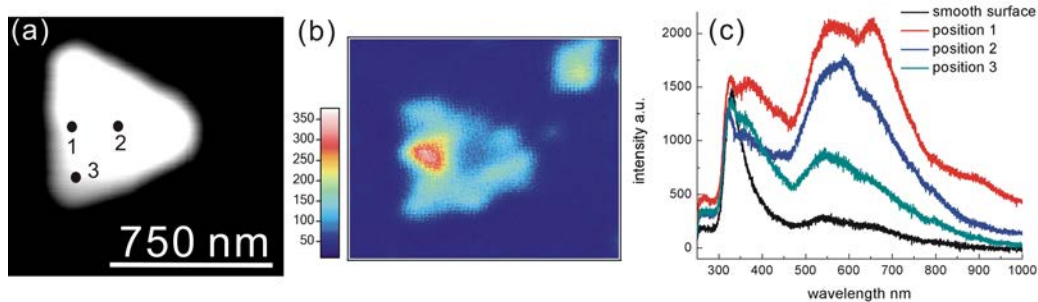


Fig. 5.5 (a) SEM image of an triangular Ag particle; (b) panchromatic CL image, obtained from the Ag particle upon irradiation with a 15keV, 3nA electron beam with a 5ms/pixel scanning rate; (c) the spectra were obtained from the positions indicated in (a), in addition to a spectrum obtained from flat Ag surface.

## 5.6 Angular distribution of emitted light

The emission angle of light upon bombardment of electrons on metal films is interesting and was studied in order to experimentally measure the angular distribution of transition radiation<sup>[140, 156]</sup>. At that time, a light detector system with a very small aperture was used to allow light accessing from a narrow emission cone into the detector. In such cases, a high beam current up to a few  $\mu\text{A}$  was necessary to generate intensive light for recording of spectra, due to the very small acceptance angle of the detector system. The high power electrons might destroy the substrates and might contaminate the sample surfaces upon electron induced deposition of a carbon film from residual gases. Carbon contamination would reduce the optical yield and the spatial resolution of secondary electron images. Furthermore, it is difficult to mount a movable detector inside an SEM.

Alternatively, the angular intensity distribution can be obtained from the cross section of the emitted light, which is reflected by the parabolic mirror into a parallel beam and then is projected onto a CCD chip. Similar angularly resolved methods were recently described by Coenen et al.<sup>[96]</sup> and by Yamamoto et al.<sup>[97, 98]</sup>. Yamamoto et al. used a small movable aperture to reveal angular distribution of the light reflected by a parabolic mirror. In our experiments, the parallel light beam reflected by the parabolic mirror is projected onto an un-cooled color CCD chip of a digital camera (Pentax

k100d), where the recorded image of the emitted light is saved as JPEG picture and the color is represented by sRGB standard. The detailed description of the experimental set-up for this purpose can be found in chapter 3. In order to obtain a perfectly parallel beam along the optical axis, the light output from the parabolic mirror is first focused via a convex lens into a bright spot by adjustment of the position of the parabolic mirror, which is in-situ monitored with a CCD camera (Watec, model WAT-525EX2), mounted in the focal plane of the convex lens ( $f=100\text{mm}$ ). The brightest spot indicates that the electron beam irradiated area is at the focal point of the parabolic mirror and consequently the output beam of the parabolic mirror is parallel to the optical axis. It should be mentioned that, although the excitation of surface plasmons by an electron beam can be confined at a very small spot, the emission of light would originate from an extended area, due to the spatially extended de-excitation of the excited plasmons. Thus the focused brightest spot is not a very perfect circle. After obtaining the parallel beam, the CCD camera is replaced by the digital camera (Pentax k100D), which is placed about 35mm behind the focal plane of the convex lens to record the cross section of the parallel beam. In order to obtain intense emission profile of the beam, the exposure time of the digital camera is usually as long as 2 minutes for each image and the beam current is as high as 10nA. Due to the very long exposure time and using the un-cooled CCD, a few noise sparks could be observed in the projected light images. However such noise is acceptable in this case.

Light collection efficiency per unit surface area on the parabolic mirror surface is a function of both, zenith angle  $\theta$  and azimuthal angle  $\phi$ , since the distance from the focal point of the parabolic mirror to its surface is varying with these angles. The recorded cross section of the parallel beam therefore does not directly reflect the real angular intensity distribution. In order to normalize the recorded images to the collection efficiency and to reveal the light emission directions, i.e., the zenith emission angle  $\theta$  and the azimuthal emission angle  $\phi$ , the angularly dependent collection efficiency and the correlation of emission directions with the positions on the projected images need to be calculated. Similar calculations have been done for a



parabolic mirror by Dana and Wang for the bidirectional reflectance investigations<sup>[157]</sup>. Their calculation method was adopted to our parabolic mirror. Only a brief discussion is following. The detailed calculation can be found in appendix.

In our experiments, considering the small space between the SEM objective and a specimen, a compact parabolic mirror with 2mm focal length is used. In order to correctly describe the surface of the parabolic mirror, the Cartesian coordinates of the coordinate system are defined in Fig. 5.6. The surface of our parabolic mirror is described by equation 5.5. Since the mirror is 0.5mm above the specimen, the height of the mirror ranges from 0.5mm to 8mm in the z direction and the width ranges from -7.5mm to 7.5mm in the x direction. A half circle with a diameter of 15mm is the cross section of the parabolic mirror in the x-z plane. The azimuthal angle  $\varphi$  as a function of position (x, z) in the x-z plane is given by equation 5.6 and zenith angle  $\theta$  as a function of position (x, z) in the x-z plane is given by equation 5.7:

$$(y+2) = \frac{x^2 + z^2}{8} \quad (-7.5 \leq x \leq 7.5, 0.5 \leq z \leq 8) \quad (5.5)$$

$$\varphi(x,z) = \arctan\left(\frac{x^2 + z^2 - 16}{8x}\right) \quad (5.6)$$

$$\theta(x,z) = \arcsin\left[\left(\frac{x^2 + z^2 - 16}{x^2 + z^2 + 16}\right) \cdot \frac{1}{\sin \varphi(x,z)}\right]. \quad (5.7)$$

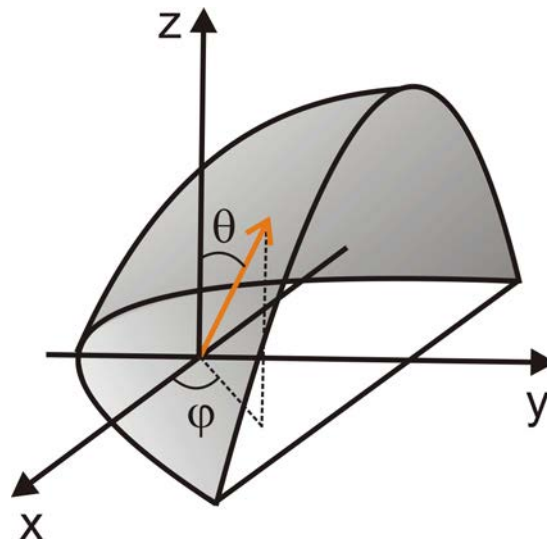


Fig. 5.6 Cartesian coordinates of the parabolic mirror.

Fig. 5.7 (a) shows the curves of constant  $\theta$  and constant  $\varphi$  in the  $x$ - $z$  plane calculated with equation 5.7 and equation 5.6. The dashed elliptical curves in Fig. 5.7 (a) represent the contour plots at constant zenith angle  $\theta$ . The values of  $\theta$  are marked with red numbers. The solid radial curves represent the contour plots at constant azimuthal angle  $\varphi$ . The values of  $\varphi$  are indicated with black numbers. The points  $(x, z)$  of the intersection of radial curves and elliptical curves in the  $x$ - $z$  plane give the emission directions  $(\theta, \varphi)$  of light. Since the parabolic mirror is symmetrical about the  $y$ - $z$  plane, All contour plots are symmetrical about the line  $x=0$  in the  $x$ - $z$  plane. Since the radius  $r$  from the origin to the surface of the parabolic mirror is small in the quadrants with  $y < 0$ , strong changes of  $\theta$  and  $\varphi$  just lead to small changes of  $x$  and  $z$  in the  $x$ - $z$  plane. Thus, the contour plots are dense in this zone. In contrast, the radius from the origin to the surface is large in the quadrants with  $y > 0$ . Small changes of  $\theta$  and  $\varphi$  result in large changes of  $x$  and  $z$  in the  $x$ - $z$  plane. Thus, the contour plots are less dense in this zone. To characterize the emission direction of the light from the nanostructures, we are interested in the intensity per solid angle  $dI/d\Omega$ . In order to obtain this quantity, the intensity in the projection plane, i.e., at the CCD-chip, has to be normalized by multiplication with  $\frac{dA(x,z)}{d\Omega}$ , which is the relationship of the surface area in the image plane per unit solid angle of the diverging beam. It can be calculated by equation 5.8:

$$\frac{dA(x,z)}{d\Omega} = \left( \frac{x^2 + z^2}{8} - 2 \right)^2 + x^2 + z^2 = r^2(x,z). \quad (5.8)$$

Fig. 5.7 (b) shows the collection efficiency per unit surface area in image plane ( $x$ - $z$  plane) with  $\frac{d\Omega}{dA(x,z)} = \frac{1}{r^2(x,z)}$ , where the maximum collection efficiency was normalized to 1. The collection efficiency is constant at circles centered at the origin. The inner half circles represent high collection efficiency due to the small values of  $r^2(x,z)$  and the outer half circles represent low collection efficiency for the larger values of  $r^2(x,z)$ . The collection efficiency changes about 25 times from the most inner circle to the most outer circle on the cross section of our mirror.

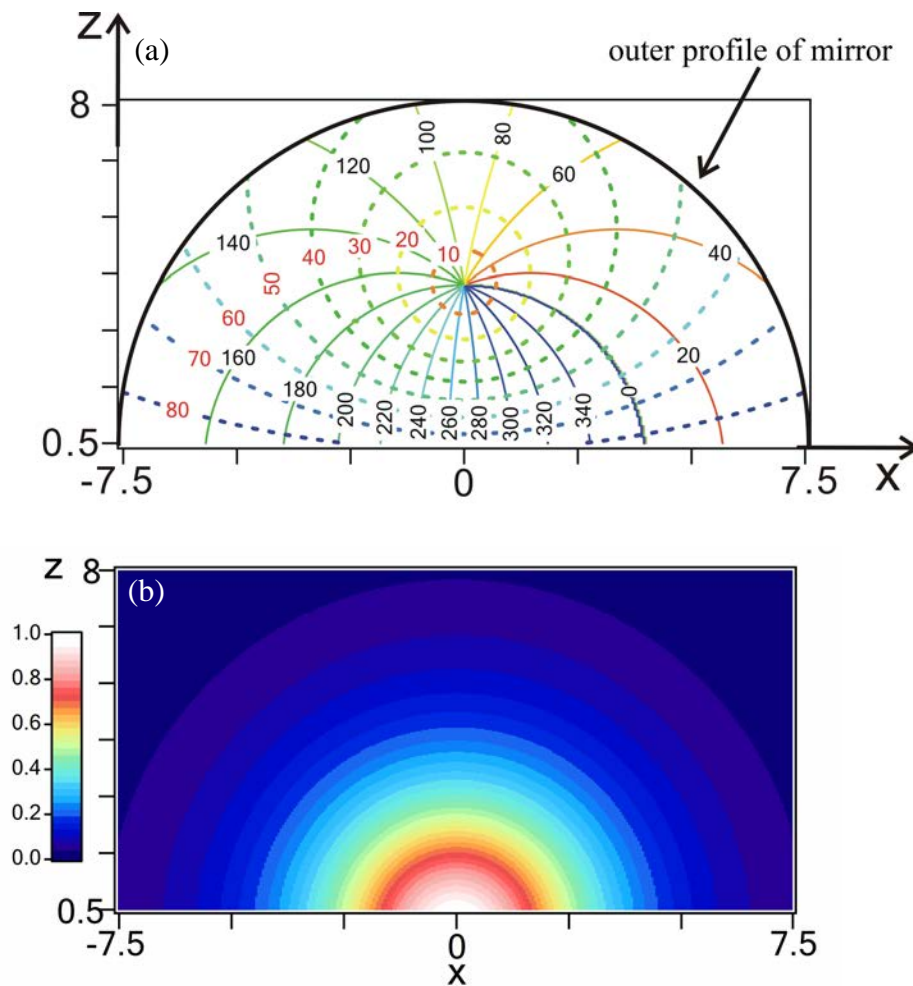


Fig. 5.7 (a) The contour plots of zenith angle  $\theta$  and azimuthal angle  $\phi$  in the  $x$ - $z$  plane, the dashed ellipse curves represent contour plots of the zenith angle  $\theta$  and the solid radial curves represent the contour plots of the azimuthal angle  $\phi$ ; (b) Calculation of the collection efficiency per unit surface area in the  $x$ - $z$  plane.

In order to estimate the validity of our experimental approach for the measurement of the angular intensity distribution, a simple case was studied, where light was emitted upon bombardment of a 200nm thick gold film with 25keV electrons. The measured color emission profile of the parallel light from the 200nm thick gold film is shown in Fig. 5.8 (a). The exposure time for this image was 30s. Each recorded color image contains three color layers, i.e., red light layer, green light layer and blue light layer. Each color layer presents the emission profile of the emitted light in a relatively narrow wavelength interval. The three color layers contained in Fig. 5.8 (a) are separately shown in Fig. 5.8 (b) to (d). The maximum intensity of each layer was

normalized to 1 and the relative intensity is indicated by a color scale. In these layers (Fig. 5.8 b-d) which were not corrected yet for the collection efficiency, the high intensity patterns are located in the small area where the collection efficiency of the parabolic mirror is high. In order to obtain the actual angular intensity distribution, the measured images were normalized to the angular dependent collection efficiency of the parabolic mirror as discussed above. The corresponding normalized emission patterns for these three layers are shown in Fig. 5.8 (f)-(h). Contour plots of zenith angle  $\theta$  were added to the normalized images. There is a black circle in every projected image due to the missing reflection of light at the 1mm diameter hole drilled through the mirror. The hole of the mirror for the passage of electrons cuts off the zenith angle below  $7^\circ$ . Therefore, the black circle in each image is an important reference to correctly locate the contour plots of zenith angle  $\theta$  and of azimuthal angle  $\phi$  in the normalized images to reveal the angular distribution.

From the previous discussion, it follows that, transition radiation is the main contribution to the observed light which is emitted from smooth gold surfaces upon bombardment with electrons. Thus the emitted light from the smooth gold surface should have an angular intensity distribution that agrees with transition radiation. According to the theory of transition radiation (equation 5.4), the angular distribution of transition radiation is approximately determined by  $\sin^2\theta\cos^2\theta$ <sup>[141]</sup>. Fig. 5.8 (e) shows the corresponding calculated angular intensity distribution of transition radiation in the image plane according to the geometry of our parabolic mirror. The contour plots of zenith angle  $\theta$  were also appended for clarity. The maximum value of  $\sin^2\theta\cos^2\theta$  was normalized to 1 and the relative value of  $\sin^2\theta\cos^2\theta$  is represented by a color scale. Fig. 5.8 (e) indicates that transition radiation is mainly emitted with zenith angles  $\theta$  in the range between  $35^\circ$  and  $60^\circ$  with maximum at  $45^\circ$ .

The CL spectra from the gold film reveal that the green light is predominant (Fig. 5.2). Therefore, in Fig. 5.8 (i), contour plots of  $\sin^2\theta\cos^2\theta$  were appended to the normalized green light image. The green light pattern with high intensity overlaps with the contour plots of  $\sin^2\theta\cos^2\theta$  with high values ( $>0.7$ ), which corresponds to the zenith angles  $\theta$  between  $35^\circ$  and  $65^\circ$ . Although here the dielectric properties of gold were not

taken into account, the good accordance of the measured angular distribution of the emitted light with the theoretical angular distribution of transition radiation demonstrates the validity of our approach for the angular intensity distribution measurements. Our results are further confirmed by Hattendorff's measurements<sup>[156]</sup>, who found that, upon the irradiation of a 69nm thick gold film with 77keV electrons, light with wavelength of 428nm was emitted with zenith angles ranging between 35° and 65° with maximum at 50°.

The intensity of the green light in Fig. 5.8 (i) is rather constant over a wide azimuthal angle region of about  $4/3\pi$ . However, in the areas close to the edge of the mirror, the intensity is slightly lower. The intensity distribution of transition radiation is expected to be independent of the azimuthal angle upon normal electron irradiation. Indeed, Kuttge's calculations show that transition radiation with wavelength of 600nm upon irradiation of gold single crystal with 30keV electrons is isotropic in the azimuthal plane<sup>[147]</sup>. We attribute the intensity variations close to the edges of the mirror to eventual mechanical blocking along the optical path and the strong reflections of the outer parts of the parallel beam by the convex lens.

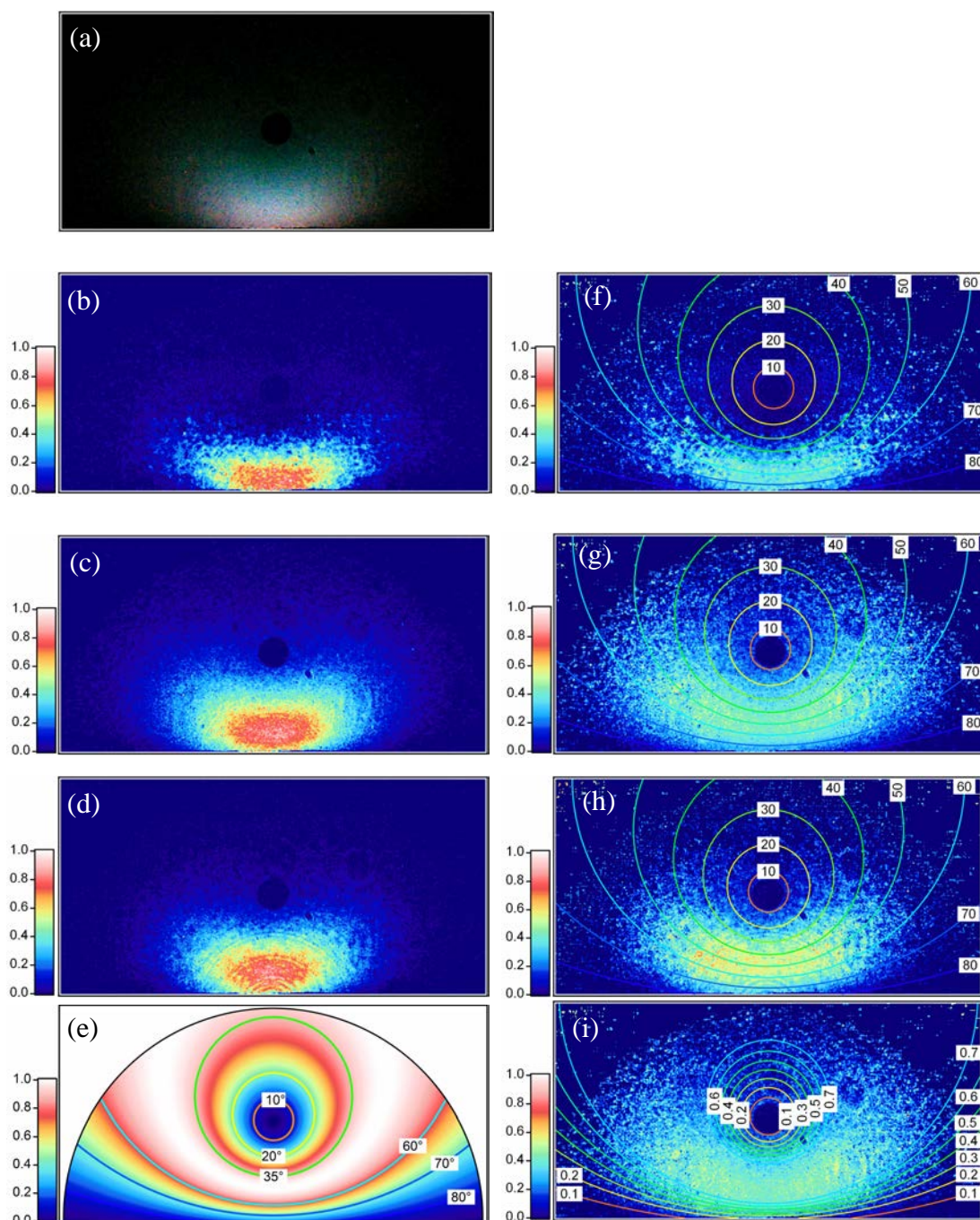


Fig. 5.8 (a) CCD image of light profile emitted from a 200nm thick gold film and its separated color layers images: (b) and (f) red light layer; (c) and (g) green light layer; (d) and (h) blue light layer; the left column images (b-d) give the raw intensity profile and the right column images (f-h) were corrected to the collection efficiency of the mirror; (e) theoretical angular distribution of transition radiation according the geometry of the mirror and (i) contour plots of  $\sin^2\theta\cos^2\theta$  were appended to the green light pattern of (g). The maximum intensity of the images was: f=118; g=118; h=103.

In order to study the angular distribution of light related to surface plasmons, a  $3\mu\text{m}$  wide bar was electrochemically milled into a mechanically polished gold foil (Fig. 5.9 a). The Au bar was placed with its long axis perpendicular to the x-z plane defined in Fig. 5.6 (the opening of the parabolic mirror). The roughness of the gold surface after polishing and immersion into the electrolyte for a few hours plays only a minor role for the radiative decay of surface plasmons. This was proven by the color, i.e., the spectra of light induced by electron irradiation of the polished gold surface. Details can be found in Fig. 5.4. However, when an electron beam (15keV, 7nA) irradiated the flat surface inside the  $3\mu\text{m}$  wide bar, an additional red pattern on the top of the green background was observed, as shown in Fig. 5.9 (b). The approximate position of the irradiated spot is indicated in Fig. 5.9 (a). To obtain more contrast red light pattern and to eliminate the green background, an OG570 filter was placed in the optical path to block the light with wavelength shorter than 570nm. Fig. 5.9 (c) shows the more clear emission pattern of red light. The three separated color layers of Fig. 5.9 (b) were normalized and are shown in Fig. 5.9 (d - f). Contour plots of zenith angle  $\theta$  were included on the red light layer to indicate the emission angles of the red light. Fig. 5.9 (d) indicates the red light emitted at a narrow range of zenith angle  $\theta$  between  $60^\circ$  and  $75^\circ$  with respect to the electron beam incidence. Most of green light emitted with zenith angle less than  $50^\circ$ . Fig. 5.9 (e) indicates that a small fraction of green light also emitted with zenith angle  $\theta$  between  $60^\circ$  and  $75^\circ$ . No light with short wavelength (blue light) emitted in zenith angle range between  $60^\circ$  and  $75^\circ$  was observed, as indicated by Fig. 5.9 (f).

As mentioned in chapter 2, electrons have the capability to excite surface plasmons, including propagating surface plasmons and localized surface plasmons. Localized surface plasmons are efficiently excited on curved surfaces, e.g., nanoparticles, and on roughened metal surfaces where multiple scattering of propagating surface plasmons occurs<sup>[12]</sup>. If we ignore the minor influence of the small surface roughness upon polishing, the distance of the surface defects (here the edges of the gold bar), is comparable to the propagation length of the surface plasmons on gold surface of a few micrometers in the visible<sup>[150]</sup>. Since the width of the bar is comparable to the decay

length of propagating surface plasmons, the localization of propagating surface plasmons by multiple scattering at the edges of the bar would not happen. Therefore, here the excitation of localized surface plasmons on the bar and their contribution to the observed red light seems improbable.

Propagating surface plasmons could be reflected or scattered by surface defects in addition to the process of transmission<sup>[12]</sup>. These interactions between the propagating surface plasmons and surface defects are dependent on the size of the defects. Sánchez-Gil's numerical calculations indicate that narrow surface defects are good reflectors for the propagating surface plasmons and wide surface defects are good scatters for propagating surface plasmons<sup>[158]</sup>. An edge is a very good light emitter due to scattering of propagating surface plasmons and more than 80% energy of propagating surface plasmons would be scattered into far field at an edge<sup>[152]</sup>. Therefore, the relatively intense emission pattern of red light in Fig. 5.9 (c) is attributed to the scattering of the excited propagating surface plasmons at the edges of the bar, surrounded by a 2 $\mu\text{m}$  wide trough.

The red light was emitted with a zenith angle in the range between 60° and 75°, as revealed by Fig. 5.9 (d), which is in accordance with numerical calculations<sup>[152, 159]</sup>, where grazing emission patterns of the emitted light upon scattering of surface plasmons at edges was shown. Furthermore, from theoretical calculation, propagating surface plasmons excited on Ag surfaces scattered by a big surface defect would emit light with a maximum emission angle of 70°<sup>[158]</sup> and of 74°<sup>[160]</sup>. The experimentally determined scattering angle of surface plasmons by a Ag protrusion into light with maximum emission at 70°<sup>[161]</sup> agrees with our measurement.

The wave vector of propagating surface plasmons with an energy of 2eV (615nm) at the Au/vacuum interface  $\mathbf{k}_{\text{spp}}$  is equal to about 1.05 $\mathbf{k}_0$ , as calculated from the optical constant of gold<sup>[85]</sup>, where  $\mathbf{k}_0$  is the wave vector of light in vacuum. According to the relationship of wave vector conservation for the coupling of propagating surface plasmons to light:  $\mathbf{k}_0 \cdot \sin\theta = \mathbf{k}_{\text{spp}} - \Delta\mathbf{k}_{\text{spp}}$ <sup>[1]</sup>, where  $\theta$  is the emission angle of light. The wave vector loss  $\Delta\mathbf{k}_{\text{spp}}$  of the propagating surface plasmons in the process of scattering is estimated to be between 0.08  $\mathbf{k}_0$  at  $\theta = 75^\circ$  and 0.18  $\mathbf{k}_0$  at  $\theta = 60^\circ$ .



For the gold bar in Fig. 5.9 (a), there are three edges surrounding the electron beam irradiated spot. Most of the red light was emitted with azimuthal angles in the range between 0 and 180°, as inferred from Fig. 5.7 (a). It fits to the theoretically predicted azimuthally anisotropic distribution of the light emitted from propagating surface plasmons scattered at a grating<sup>[147]</sup>. However, we did not find out the actual scattering edges for the observed emission images in Fig. 5.9. As an outlook, it is very interesting and meaningful to measure the angular distribution of the scattered propagating surface plasmons by various surface defects, in order to thoroughly understand the scattering process, for example, by a metallic or semiconductor single particle and a single line.

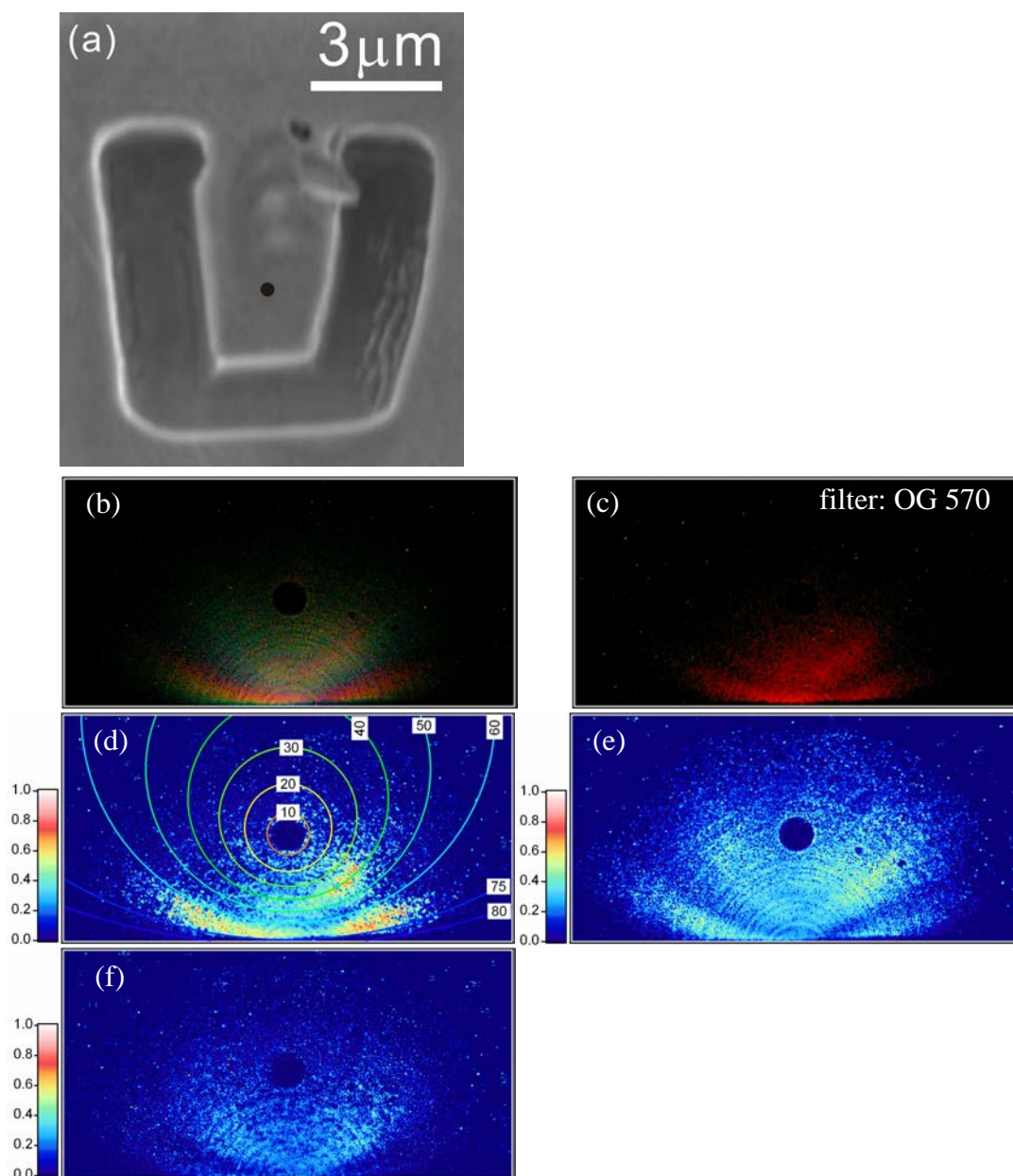


Fig. 5.9 (a) SEM image of a  $3\mu\text{m}$  wide gold bar (b) measured emission pattern of the emitted light with an electron beam ( $15\text{keV}$ ,  $7\text{nA}$ ) rested at the spot indicated in (a) for 2min; (c) measured emission pattern of the light with wavelength longer than  $570\text{nm}$ ; The normalized emission pattern of the separated layers: (d) red light layer; (e) green light layer and (f) blue light layer. The maximum intensity for the each normalized layer is 200.

We now turn to the emission characteristics of smaller, electrochemically fabricated Au-microstructures. The angular distributions shown in Fig. 5.10 and Fig. 5.11 were obtained from the apexes of gold pyramids. Fig. 5.10 (a) and (b) show the projected images without and with an OG570 filter in the optical path, recorded with an electron beam (15keV, 7nA) irradiating the apex of the pyramid (position 2, indicated in Fig. 5.4). Fig. 5.10 (c) shows the normalized angular distribution of the red light. In contrast to the nearly grazing emission of the light upon the scattering of the propagating surface plasmons at the 3 $\mu$ m wide bar in Fig. 5.9, red light (Fig. 5.10 c) was mainly emitted almost parallel to the surface normal with the zenith emission angle less than 30°. Light emitted with the zenith angle larger than 50° was rarely observed. The normalized red light image (Fig. 5.10 c) shows an azimuthally symmetrical pattern. This indicates that the azimuthal emission angle  $\phi$  ranges from 0 to  $2\pi$ . Similar angular intensity distribution was also observed for the light emitted from a similar structure, i.e., the pyramid in Fig. 5.11 (a), enclosed by a triangular trough. The measured emission patterns are shown in Fig. 5.11 (b, c). The normalized color layers are separately shown in Fig. 5.11 (e-f). The red light also shows an azimuthally symmetrical pattern located in the area with the zenith angle less than 35° in Fig. 5.11 (d).

The angular distribution of the light induced by electrons on gold pyramids is different from the angular distribution of light upon the scattering of propagating surface plasmons at the edges, indicating different emission mechanisms. Similar angular distribution of light emitted from an electron beam irradiated Ag nanoparticle, which was supported by a carbon film covered substrate, was observed by Yamamoto et al.<sup>[162]</sup>. They ascribed a dipolar Mie mode oscillating along the substrate surface excited on the Ag particle to the observed angular distribution of light, which is approximately given by  $\cos^2\theta$ <sup>[162]</sup>. Fig. 5.10 (f) shows the corresponding calculated pattern of  $\cos^2\theta$ , according to the geometry of our parabolic mirror. Contour plots of  $\theta$  were appended for clarity. The high value of  $\cos^2\theta$  (>0.7) are found inside the area with zenith angle  $\theta$  less than 30°. This is nearly identical to the angular distribution of the red light shown in Fig. 5.10 (c) and Fig. 5.11 (d). From the angular intensity

distribution, we therefore deduce that a dipole perpendicular to the electron beam incidence was probably excited at the apexes of pyramids. A more precise calculation, taking to the geometry of the gold structures into account would be desirable in the future.

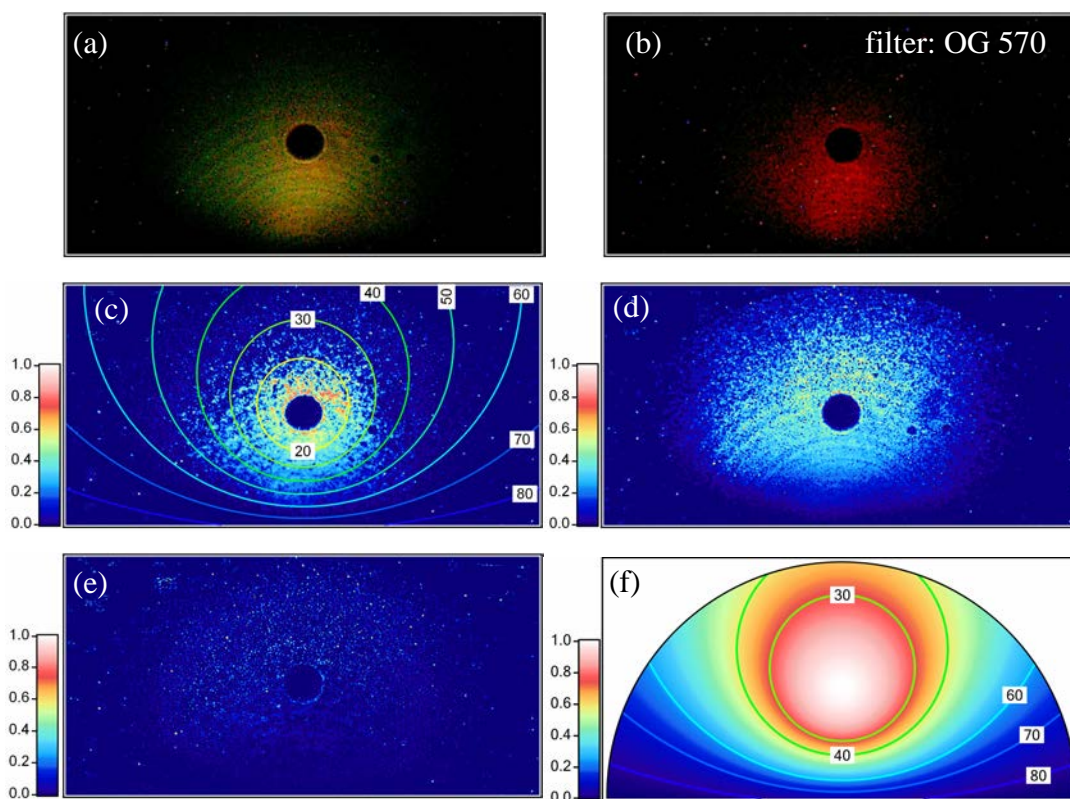


Fig. 5.10 (a) Measured emission pattern of the light emitted from the electron beam irradiated pyramid shown in Fig. 5.4, position 2, the integration time was 2min; (b) measured emission pattern of the light with wavelength longer than 570nm; The normalized emission pattern of the separated layers: (c) red light layer (maximum: 394); (d) green light layer (maximum: 398) and (e) blue light layer (maximum: 298); (f) calculated pattern of  $\cos^2\theta$ .

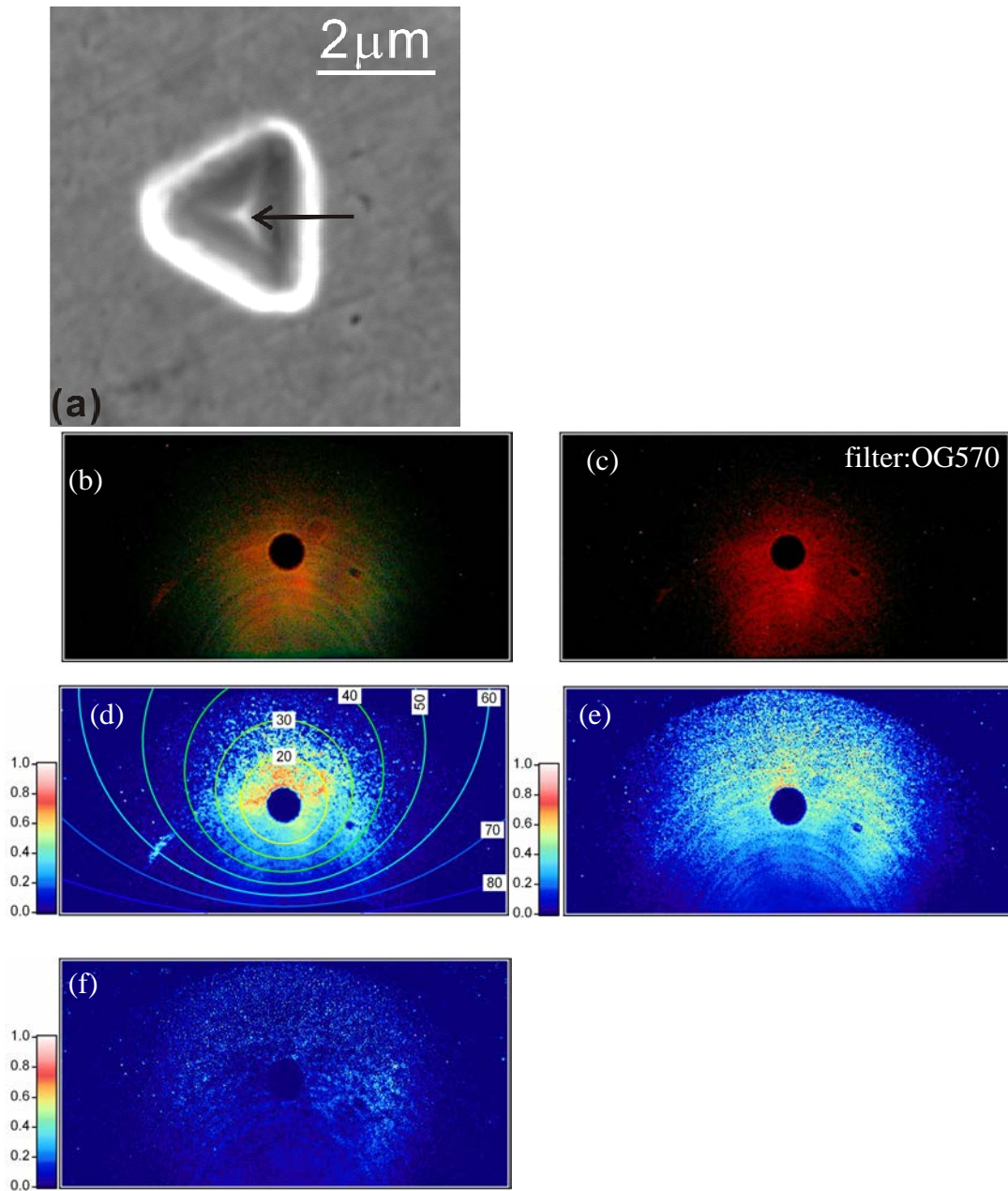


Fig. 5.11 (a) SEM image of a pyramid fabricated on a gold foil; (b) measured emission pattern of the light emitted from the pyramid and (c) measured emission pattern of the light with wavelength longer than 570nm; normalized images: (d) the red light layer (maximum: 583); (e) the green light layer (maximum: 349) and (f) the blue light layer (maximum: 296).

## 5.8 Conclusions and Outlook

In this chapter, optical properties of the electrochemically fabricated Au structures and Ag nanoparticles were investigated by cathodoluminescence upon local irradiation with 15keV electrons. The spatial emission intensity distribution on the Au and Ag structures was reflected by the photon maps. The spectra of the emitted light were also recorded. In order to reveal the emission direction of the emitted light, an angularly resolved method was developed, i.e., revealing the emission directions ( $\theta$ ,  $\phi$ ) from the projection positions of the emitted light on a color CCD-chip.

There are several possible contributions to the observed light from the electron irradiated Au and Ag structures, mainly transition radiation and radiative surface plasmons. As a reference, the cathodoluminescence of 200nm thick Au films as well as mechanically polished Au foils was studied. Both, the spectra of the emitted light peaking in the green spectral region and the angular distribution of the emitted light agreeing with the theoretical angular distribution of transition radiation, which demonstrates that transition radiation is the predominant contribution to the emitted light from electron beam irradiated flat Au surfaces. In comparison with the emission intensity from the flat Au surfaces, strongly enhanced emission was observed when the electron beam hit the Au structures, e.g., an Au ridge and Au pyramids. Spectral measurements revealed that enhanced emission was in the red spectral region. Similarly, an intense emission area with a diameter of about 150nm was observed on a triangular Ag nanoparticle. The enhanced emission is attributed to the radiative decay of excited surface plasmons.

The projection patterns of the emitted light on the color CCD-chip were strongly dependent on the electron beam irradiated Au-structures, e.g., the angular emission pattern changed significantly when going from an electron beam irradiated 3 $\mu$ m wide Au bar to the apexes of nanometer-sized Au pyramids. Grazing emission of red light with zenith angles between 60° and 75° with respect to surface normal was observed from the electron irradiated Au bar. Whereas for the electron irradiated Au pyramids, an azimuthally symmetrical pattern of red light with zenith angle less than 35° was

observed. Due to the irradiation of the flat surface on the relatively wide Au bar, the red light is ascribed to the effective scattering of propagating surface plasmons at the edges of the bar. In contrast, the red light emitted from the pyramid apexes is attributed localized surface plasmons, oscillating perpendicular to the electron beam incidence.

As an outlook, precise simulations should be carried out to understand the radiation of the surface plasmons, excited on various metallic nanostructures. It is also interesting to investigate the scattering angle of the propagating surface plasmons by various surface defects in order to understand the scattering process, e.g., scattering of propagating surface plasmons by the apex of a metallic tip, which is close to the surface, e.g., in an STM.

# Chapter 6 Cathodoluminescence of silver and gold tips

## 6.1 Nanometer-sized metal tip: an optical antenna

Optical antennas are devices which can efficiently concentrate energy of the freely propagating electromagnetic wave with optical frequency into the electromagnetic near field in their vicinity and vice versa<sup>[16, 163, 164]</sup>. Metallic nanostructures can act as optical antennas, which can efficiently focus light or radiate light via excitation of surface plasmons<sup>[163]</sup>. Nanometer-sized metal tips are one of easily fabricated nanostructures which can be used as optical antennas. A sharp metal tip serves as either a local scatterer to convert evanescent waves, which are confined on the irradiated metal surface, into freely propagating waves in far field or a light focusing element, such as in apertureless-type (or scattering-type) scanning near field optical microscopy<sup>[163, 165]</sup>. In addition to use the sharp metal tips as scatterers to perturb the evanescent waves<sup>[166]</sup>, the efficient light focusing and the strongly enhanced near field at the metal tips, originating from the quasi-static lightning-rod effect and the excitation of surface plasmons<sup>[163]</sup>, have attracted much interest for various phenomena and applications, such as tip-enhanced Raman spectroscopy<sup>[23, 24]</sup>, two-photon excited fluorescence<sup>[167]</sup> and the second-harmonic generation<sup>[168, 169]</sup>. In apertureless-type scanning near field optical microscopy, the spatial resolution and the local optical response of the substrates can be as high as 10nm, mainly limited by the apex radius of the sharp metal tips<sup>[170]</sup>. However, the reproducible preparation of the sharp metal tips by employing electrochemical etching is still challenging, whereas the performance of apertureless-type near field microscopy is strongly dependent on the optical response of the tips. For example, the scattering spectra of the evanescent waves by Au tips strongly varies from tip to tip<sup>[166]</sup>. This demonstrates that the optical response of the Au tips and the field enhancement near the Au tips are sensitive to the detailed properties of a given tip, i.e., the geometry (the apex radius and the cone



angle) and the length of the tips<sup>[171]</sup>. Thus, an important issue in tip-enhanced spectroscopy is to reveal the field enhancement and distribution near a metal tip as well as the coupling between the tip and the sample. Various theoretical methods, such as the multiple multipole method (MMP)<sup>[172]</sup>, the finite element method (FEM)<sup>[173]</sup> and the finite difference time domain calculations (FDTD)<sup>[154, 174, 175]</sup>, have been applied to calculate the field distribution near a free-standing tip and the field distribution inside a tip-sample nanocavity. Summary on the theoretical treatment of the near field of a metal tip can be found, e.g., in a recent review<sup>[28]</sup>. According to the calculations, the highest field enhancement for a free standing metal tip is achieved at the apex of the tip, irradiated with light polarized parallel to the tip axis<sup>[172]</sup>. However, even at the optimum excitation conditions, only moderate field enhancements (typically less than 100) were found near a free standing Au tip, as demonstrated by theoretical calculations<sup>[154]</sup> and experimental measurements<sup>[176]</sup>. The moderate field enhancements of the free standing tip is due to the opening geometry<sup>[165]</sup>. In contrast, in presence of a substrate in close proximity to the tip, the field can be one order of magnitude higher, compared to the free standing metal tip<sup>[154]</sup>. For example, the local field enhancement inside a tip-sample cavity is up to a factor of several hundred for a 2 nm distance between the tip and the sample<sup>[154]</sup>. The presence of the substrate modifies the field distribution of the free standing tip and hence the field enhancement, which is due to the influence of the image dipole when the tip and the sample are in very close proximity<sup>[165]</sup>.

So far, most theoretical calculations and experimental investigations of the field enhancement near a metal tip were based on light irradiation. In the experiments, the geometrical characterization of a given tip was typically carried out before or after the optical characterization. Furthermore, the scattered light from the tip had to be separated from an intensive irradiation background to gain a high signal to noise ratio<sup>[165]</sup>. Though the scattering is confined to near field zone and the tips dipped into the evanescent waves, the actually active spots at the apex were unknown. In this chapter, in order to characterize the optical properties of the metal tips and their response to the external electric field as well as the distribution of the electromagnetic

field near to the apex of the metal tips, for their application in the apertureless-type scanning near field optical microscopy, we use an electron beam to irradiate the metal tips in order to study the response of the tips to the external electric field with high spatial resolutions. The investigations concentrate on commonly used Ag tips and Au tips. The geometry of the tips and their local optical properties are simultaneously obtained by SE images and photon maps. The intensity distribution of emitted light upon local electron irradiation reveals the distribution of the excited surface plasmons, as described in chapter 5.

## 6.2 Preparation of gold and silver tips

### 6.2.1 Preparation of gold tips

Electrochemical etching of gold wires in aqueous chloride solutions is a widely used method for the preparation of Au tips<sup>[177]</sup>. Various preparation procedures for Au tips were summarized by Boyle et al.<sup>[178]</sup>. In order to remain their mechanical strength, gold wires are not flame annealed prior to electrochemical etching in our experiments. Since no additional cut-off circuit<sup>[28]</sup> and optical microscope for monitoring of the etching process<sup>[177]</sup> are required, our electrochemical cell for preparation of Au tips is very simple. As sketched in Fig. 6.1 (a), an electrolyte film (1:1 mixture of 37% HCl and H<sub>2</sub>O, approximately 6M) is formed across a  $\phi$  7mm Pt ring which was bent from a Pt wire with a diameter of 0.5mm. The Pt ring acts as a counter electrode. An Au wire with a diameter of 0.25mm is immersed into the electrolyte film from top with a micrometer screw and placed at the center of the Pt ring. A meniscus forms around the Au wire because of the surface tension of the electrolyte. After a stable electrolyte film is formed between the Au wire and the Pt ring counter electrode, a high frequency sine wave (50 kHz,  $V_{p-p}$ : 2.3V) adding to a 2.0V DC offset, generated by a HP 3310A function generator, is applied to the Au wire and the Pt ring. When the wire is etched through, the lower part is dropping into a holder, which is placed beneath the wire. The most important thing for successful tip preparation with the drop-off

configuration is the stability of the electrolyte film during the etching process. Renewal of the electrolyte film usually results in bad tips. The electrochemical etching is usually carried out in a fume hood to avoid HCl fumes. In order to protect the electrolyte films against draft, the electrochemical etching cell is isolated by a glass wall, as sketched in Fig. 6.1 (a). The position of the Au wire inside the Pt ring and the symmetry of the meniscus forming around the Au wire determine the geometry of the apex cone of the tips. Au wires are very soft and the etching neck is easily deformed by very small forces. Since the etching neck has to bear the weight of the lower part of the Au wires, the diameter of tips is slightly affected by the length of the lower part of the wires. Fig. 6.1 (b) shows an SEM image of an electrochemically etched Au tip with the parameters mentioned above.

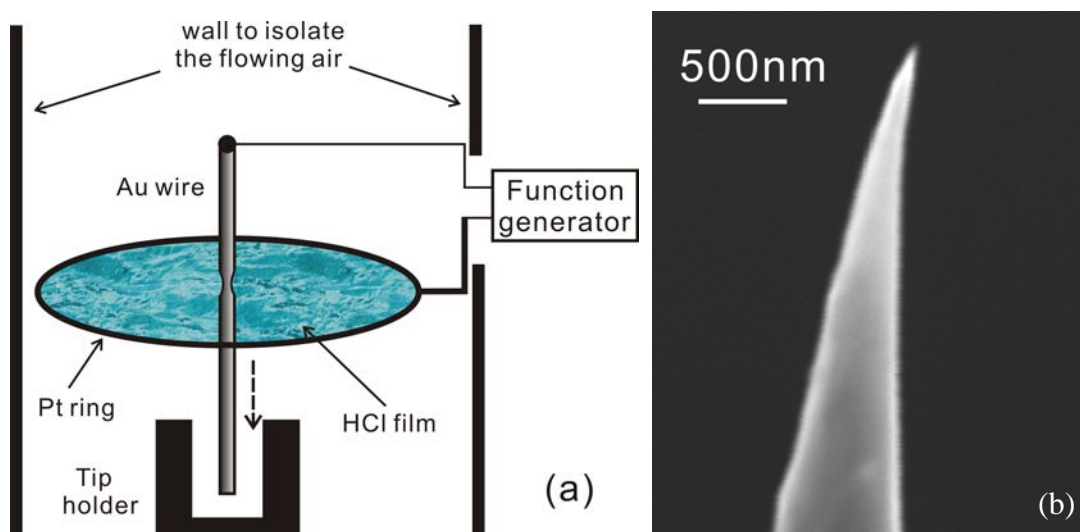


Fig. 6.1 (a) Scheme of electrochemical etching of Au tips; (b) SEM image of an electrochemically prepared Au tip.

## 6.2.2 Preparation of silver tips

Although the reproducible preparation of Ag tips with a few 10nm apex radius by electrochemical etching is more difficult than the preparation of Au tips<sup>[179]</sup>, it is still a common method for the preparation of Ag tips. Widely used electrolytes for electrochemical etching of Ag tips are perchloric acid/ethanol ( $\text{HClO}_4/\text{C}_2\text{H}_5\text{OH}$ )

solutions<sup>[90]</sup> and ammonia solutions ( $\text{NH}_3/\text{H}_2\text{O}$ )<sup>[180, 181]</sup>. In our experiments, the Ag tips are prepared by employing electrochemical etching in  $\text{HClO}_4/\text{C}_2\text{H}_5\text{OH}$  solutions. The volume ratio of  $\text{HClO}_4$  (70%) to  $\text{C}_2\text{H}_5\text{OH}$  is 1:4. Since no automatically cutoff control circuit exists to avoid the over etching of the tips, a drop-off configuration is used, similar to the configuration for the preparation of Au tips in Fig. 6.1 (a). Similarly, an electrolyte film is formed across a counter electrode, which is an Ir ring with a diameter of 7mm, bent from a 0.5mm diameter Ir wire. A 0.25mm diameter Ag wire (99.99%, Alfa) is immersed into the electrolyte film with a micrometer screw and is placed at the center of the counter electrode. A DC voltage of 2.5V is applied to the wire. The lower part of the wire would drop off in less than 1 minute, soon after the application of the voltage. The sharpened tip is obtained at the end of the lower part of the wire. The tip at the upper part is over-etched and useless. Though the etching time is less than 1 minute, the electrolyte film has to be refreshed at least once during the process of etching, due to the instability of the electrolyte film.

### 6.3 Cathodoluminescence of silver tips

As mentioned in chapter 2, silver has a very low imaginary part of the complex dielectric constants in the near UV and visible spectral ranges and therefore very low internal damping of surface plasmons is expected. Hence, roughened silver substrates usually can provide very high enhancement factors for Raman spectroscopy<sup>[89]</sup>, due to the resulting strong local electric field by surface plasmons. Similarly, in scanning tunneling microscope induced light emission experiments, high emission efficiencies are usually achieved by Ag tips<sup>[182]</sup>. This is why field enhancement and distribution near Ag tips are of interest. In this section, the cathodoluminescence of Ag tips is studied and discussed.

Fig. 6.2 (a) shows an SEM image of an electrochemically prepared Ag tip. The apex diameter of this Ag tip is about 200nm. The corresponding CL image of this Ag tip, irradiated with a 15keV, 1nA electron beam, is shown in Fig. 6.2 (b). The scan rate of the electron beam was 10ms/pixel. The most intensive emission occurred when the

electron beam irradiated the apex of the Ag tip within an area of about 300nm diameter. In order to find out the reasons for the enhanced emission at the apex of the Ag tip, spectra were recorded by placing the electron beam at three different positions along the tip, i.e., position 1 within the maximum emission spot, position 2, about 500nm away from position 1 and position 3, about 1000nm from position 1. The approximate irradiated positions are indicated in Fig. 6.2 (a). The spectra of the emitted light with the beam placed at these three electron beam positions are shown in Fig. 6.2 (c). A narrow peak at 330nm was observed for all three spectra, which demonstrates the contribution of the radiative bulk plasmon of Ag to the observed light. However, the intensity of the bulk plasmon peak varied with the irradiation positions. The intensity of the bulk plasmon peak obtained at position 3 is much lower than that obtained at position 1 and 2. According to my knowledge, the definite reasons for the decreasing intensity of the radiative bulk plasmon with increasing distance from the apex are unknown. The light emitted (spectrum 1) from the spot with high emission intensity at the apex of the tip has a similar wavelength distribution as the light emitted from an Ag particle (position 3, indicated in Fig. 5.5 in chapter 5). In contrast, the spectrum 3 is similar to the spectrum of light emitted from smooth Ag surfaces (also see Fig. 5.5 in chapter 5). An additional peak at about 360nm was observed in spectrum 1 in Fig. 6.2. The intensity of the peak at 360nm rapidly decreased when the irradiation position shifted about 500nm away from the maximum emission area. It only can be observed if we look at the spectrum 2 carefully (Fig. 6.2 c), which is indicated by an arrow. The emission of the 360nm light was strongly confined at the apex of the Ag tip. Therefore, we ascribe the enhanced emission at the tip apex to radiation of localized surface plasmons excited at the apex of the Ag tip. It is accordance with the theoretical calculations, i.e., electric field enhancement occurs at 350nm due to excitation of localized surface plasmons at the apexes of Ag tips<sup>[171]</sup>. On the shaft of the Ag tip in Fig. 6.2 (a), the propagating surface plasmons were probably excited by the electron beam, but they were not scattered into light due to the relatively smooth surface and the very short propagation length of the surface plasmons at short wavelengths, which is in the order of 100nm<sup>[150]</sup>.

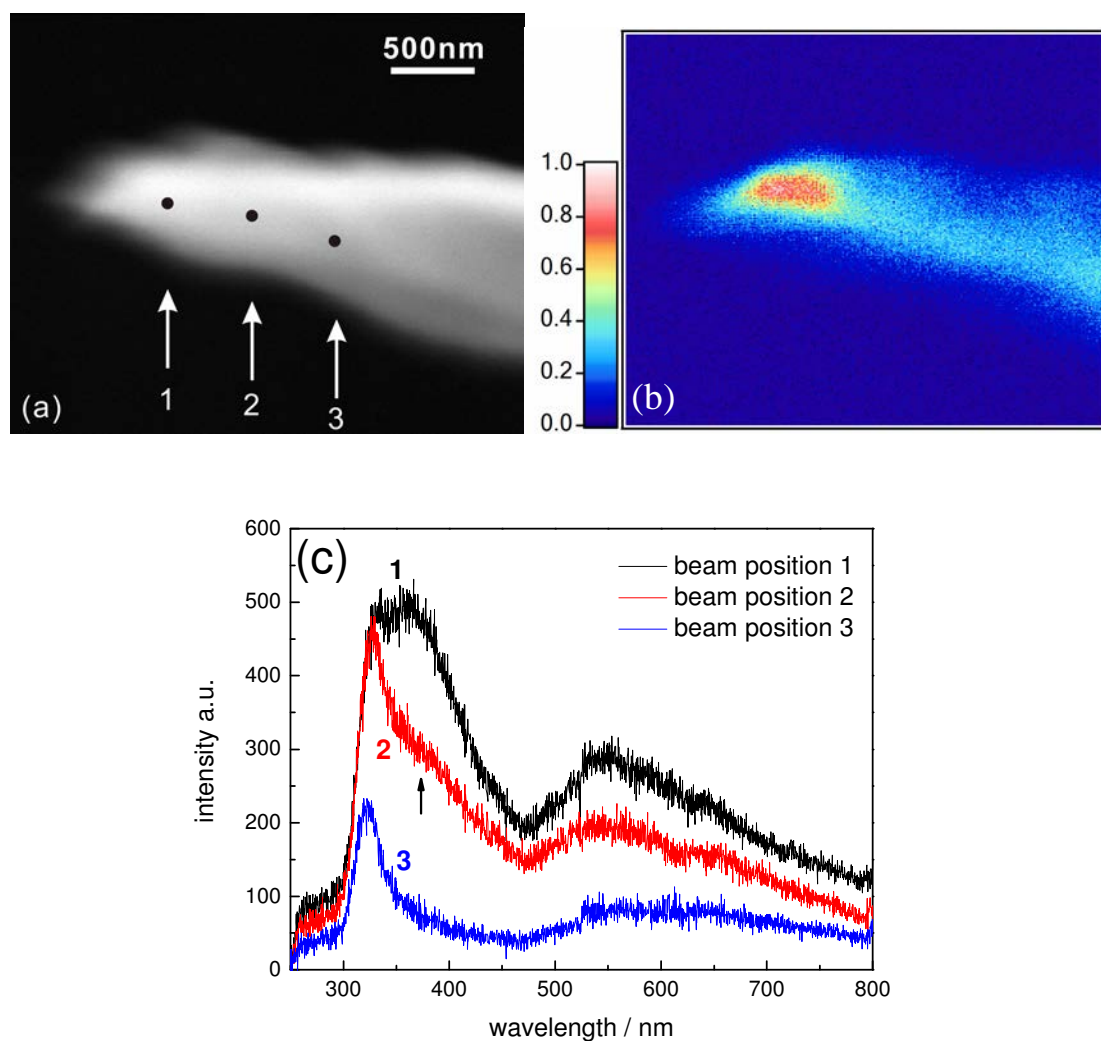


Fig. 6.2 (a) SEM image of an Ag tip and (b) its corresponding panchromatic cathodoluminescence image, irradiated with a 15keV, 1nA electron beam, the dwell time was 10ms/pixel, the maximum counting rate (127counts/10ms) was normalized to 1; (c) the spectra were obtained from three electron beam irradiated positions, as indicated in (a). The integration time was 50s for each spectrum.

A highly symmetrical Ag tip with an apex radius of about 50nm is shown in Fig. 6.3 (a). The highest emission intensity was found when a 15keV, 1nA electron beam scanned across the tip and irradiated the small particles on the roughened surface at the shaft of the tip. The maximum counting rate was 305 counts/10ms (Fig. 6.3 b). A slightly enhanced emission at the apex of the Ag tip was also observed, as indicated by an arrow in Fig. 6.3 (b). Hence, the small particles seem to be better optical

emitters than the apex of the tip. In order to get a more contrast CL image of the tip apex, the electron beam scanned across the square indicated area. The SEM image of the zoomed in part and the corresponding CL image are shown in Fig. 6.3 (c) and (d), respectively. In Fig. 6.3 (d), the maximum emission found at the right side is due to the surface roughness. Besides this, two enhanced emission areas on the smooth surface along the tip were observed. One was confined at the apex of the Ag tip with a diameter of about 200nm. Another enhanced emission area was confined at about 1.5 $\mu$ m away from the apex. Spectrum 1 was recorded when the electron beam irradiated the apex (Fig. 6.3 e). It indicates that, besides the radiative bulk plasmons, surface plasmons contributed to the observed light peaking at 360nm. A similar wavelength distribution of the emitted light was observed (spectrum 2), when the electron beam irradiated position 2, marked in Fig. 6.3 (c). In accordance with the CL map, the intensity of the spectrum 2 is higher. As discussed above, excitation of surface plasmons resulted in the enhanced emission at the apex of the tip.

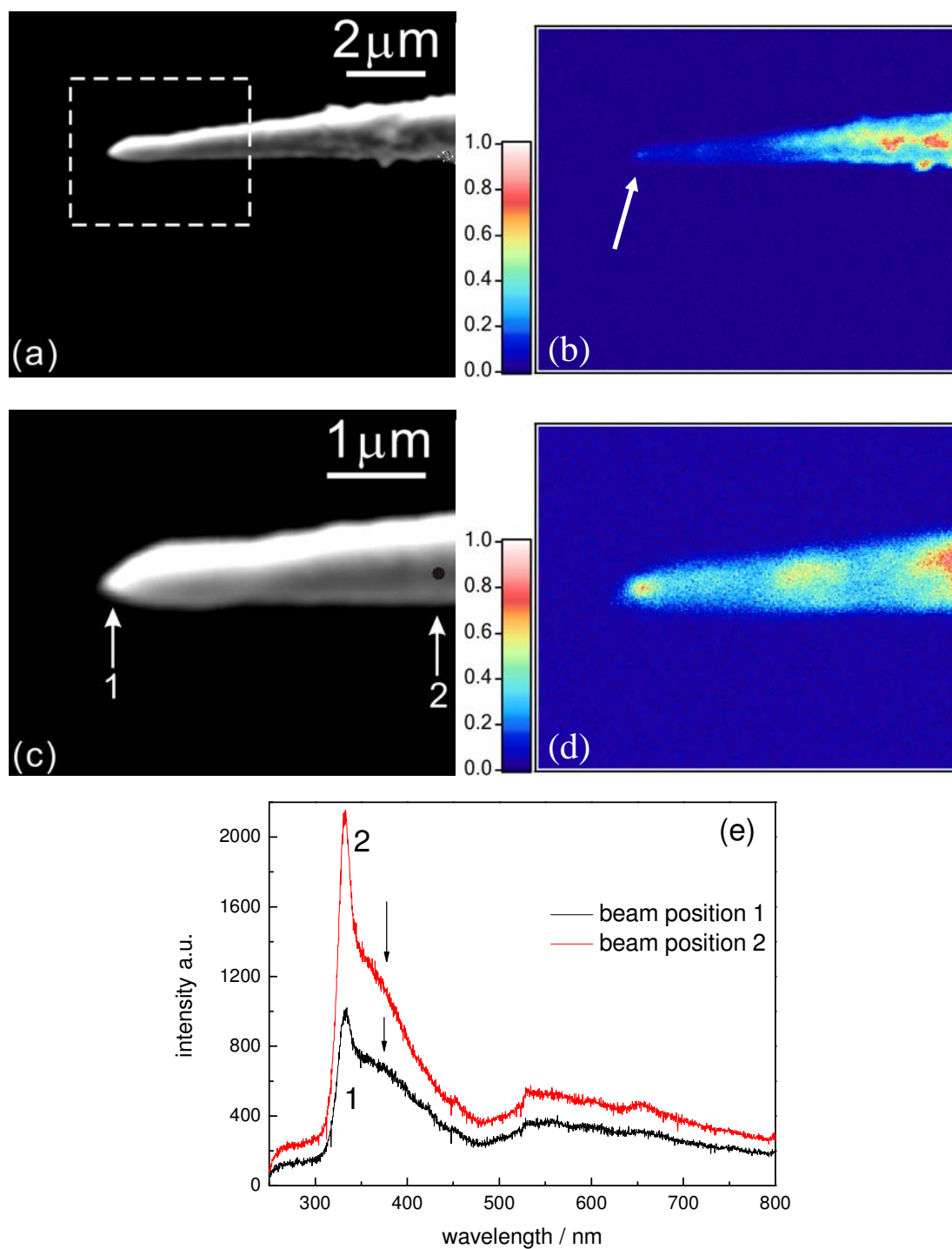


Fig. 6.3 (a) SEM image of an Ag tip and (c) SEM image of the tip with higher magnification, indicated by a dash line square in (a); (b) and (d) are the corresponding CL images of (a) and (c), irradiated with a 15keV, 1nA electron beam, the dwell time was 10ms/pixel, the maximum counting rates (b: 305counts/10ms, d: 114counts/10ms) were normalized to 1 for the CL images; (e) the spectra were obtained from two electron beam irradiated positions indicated in (c). The integration time was 50s.



## 6.4 Cathodoluminescence of gold tips

Au tips are commonly used in tip-enhanced Raman spectroscopy due to the relative easy preparation and their good oxidation resistance. Fig. 6.4 (a) and (c) show SEM images of two Au tips, both with an apex radius less than 50nm. A 15keV, 1nA electron beam scanned across the Au tips with a rate of 10ms/pixel and 5ms/pixel, respectively. The corresponding CL images are shown in Fig. 6.4 (b) and (d). No enhanced emission was observed at the apex of Au tips. The emission intensity was almost homogeneously distributed along the Au tip in Fig. 6.4 (b). As shown in Fig. 6.4 (d), the light emitted when the electron beam hit in the proximity of the sharp apex of the Au tip was lowest, even though the radius of the apex is only a few 10nm. However, spectrum 1 shown in Fig. 6.4 (e) reveals that the light emitted in the proximity of the apex is peaking at about 585nm, which is different from spectrum 2 obtained by electron irradiation of the position about 3 $\mu$ m away from the apex. Spectrum 2 is almost identical with the spectra obtained from smooth Au surfaces (see chapter 5). This demonstrates that the main contribution to the observed CL is transition radiation at this position at the shaft of the tip and the contribution from surface plasmons was not observed. As mentioned in chapter 2, the electron beam can directly excite propagating surface plasmons. The apex of Au tips was demonstrated to be a light emitter for scattering of propagating surface plasmons into far field<sup>[183]</sup>. However, only of the order of 0.1% - 1% of incident light was re-radiated into far field at the tip apex, even under optimized coupling conditions<sup>[183]</sup>. This demonstrates that the tip apex is not a very good scatter for propagating surface plasmons. Additionally, the propagation length of surface plasmons with wavelength of 550nm is very short, in the order of a few 100nm<sup>[150]</sup>. These might be the reasons that no contribution from propagating surface plasmons was observed at the irradiated position at the shaft of the tip. In contrast, upon irradiation in the proximity of the apex, the peak at 585nm points to weak deexcitation of surface plasmons. No significant enhancement was observed because of the weak de-excitation of surface plasmons at the apex. The integrated area of the two spectra in Fig. 6.4 (e) is almost

identical.

The strength of the excitation of surface plasmons and the field enhancement at the apex of the tip are dependent on the polarization of the exciting sources with respect to the axis of the tip<sup>[165, 172]</sup>. For example, light, with electric field polarized parallel to the tip axis, induces surface electrons (surface plasmons) oscillating along the tip axis with the external electric field, which generally results in a strongly enhanced field near the apex of the tip and the accumulated surface electrons at the apex; whereas, if the electric field is polarized perpendicularly to the axis of the tip, no field enhancement beneath the apex occurs and not net surface electron density accumulates at the apex<sup>[165, 172]</sup>. Here, an electron beam (a few 10keV) is usually used as an excitation source. An evanescent electric field is produced by the electrons<sup>[74]</sup>. The electric field produced by the electrons moving with a uniform velocity along a straight trajectory has a parallel component and a perpendicular component with respect to their motion direction. The perpendicular component of the electric field produced by the electrons in uniform motion is stronger than the parallel component of the electric field, with respect to the motion of the electrons. The polar distribution of the electric field is dependent on the velocity of the electrons<sup>[184]</sup>. For the cases discussed above, the electron beam perpendicularly irradiated the tips with respect to the axis of the tips. Therefore, the electric field produced by the electron beam had a component which polarized the Au tips along their axis (longitudinally). However for the Au tips, no obviously enhanced emission at the apex was observed, which demonstrates that surface plasmons are only weakly excited at the apex, in comparison with the strongly enhanced emission from the Au structures discussed in chapter 5. The weak excitation of surface plasmons at the apex of the Au tips can not just be ascribed to the polarization of the external electric field. The theoretical calculations predict that the local field enhancement near the apex of a free standing Au tip is typically in the range of 20-40<sup>[154]</sup>. The average electric field enhancement near an Au tip apex with a radius of 20nm was experimentally determined to be 8-25<sup>[176]</sup>. These are consistent with our observations, i.e., the spectra indicated the excitation of surface plasmons at the tip apex, but they were not reflected by the CL

images due to their weak excitation and the strong background due to transition radiation.

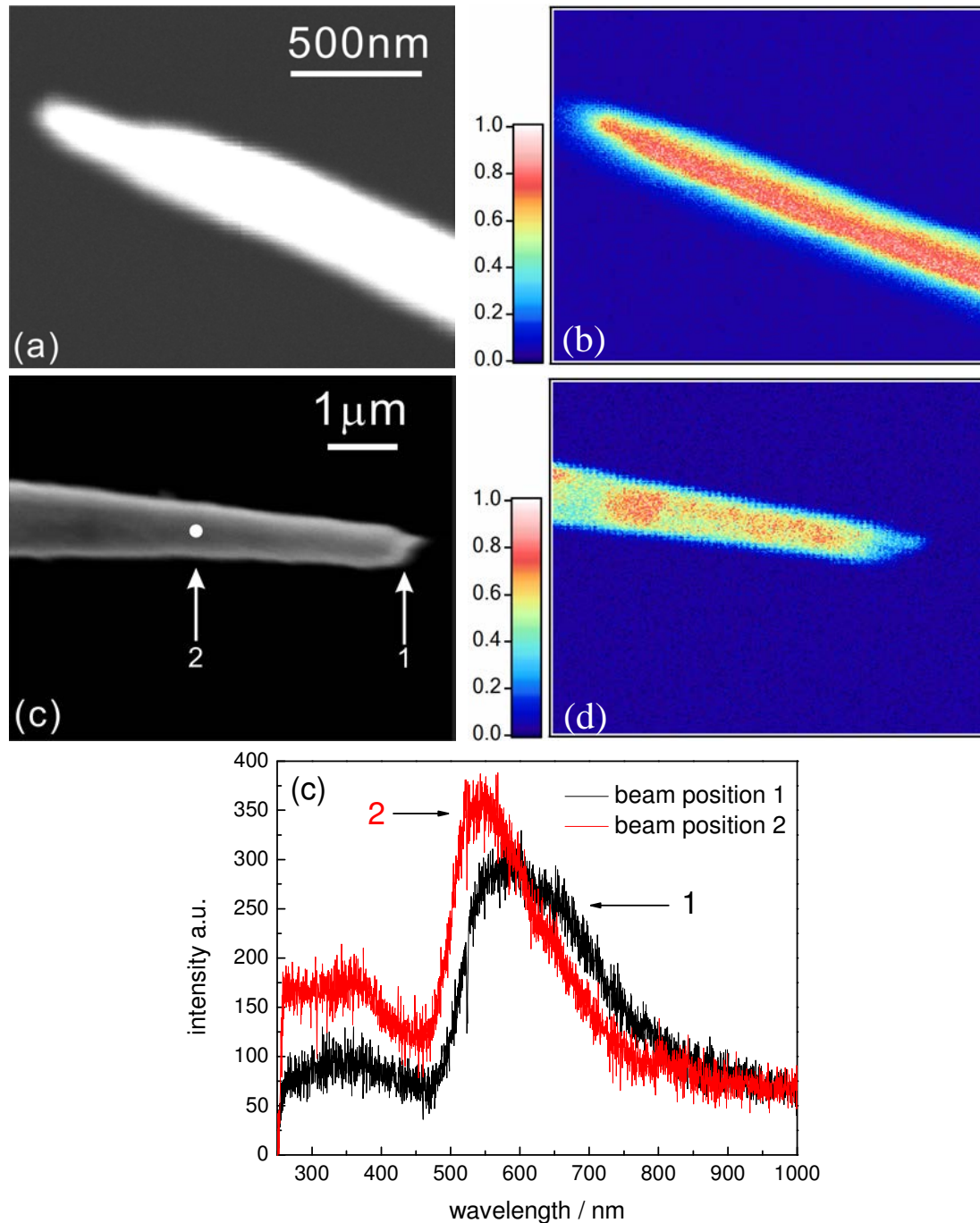


Fig. 6.4 (a) and (c) SEM images of Au tips; (b) and (d) their corresponding CL image, irradiated with a 15keV, 1nA electron beam, the dwell time was 10ms/pixel for (b) and 5ms/pixel for (d), the maximum counting rates (b: 225 counts/10ms and d: 98 counts/5ms) were normalized to 1; (e) the spectra were obtained from two electron beam irradiated positions indicated in (c). The integration time was 50s.

From some Au tips, e.g., that one shown in Fig. 6.5, slightly enhanced light emission at the apex was observed. The light emission from this Au tip was induced by a 20keV, 1nA electron beam with a scan rate of 10ms/pixel. A detailed intensity profile (Fig. 6.5 d) along the axis depicts this slightly enhanced emission at the apex more clearly. The intensity slowly decreased with increasing distance of the irradiated spot from the apex. If the tip apex acts as a scatterer for the propagating surface plasmons, the intensity is expected to exponentially decrease with the increasing distance of the irradiated spot from the apex<sup>[150]</sup>. However, the intensity variation with the distance long the tip does not exhibit an exponentially dependent behavior. The spectrum recorded near the apex of the tip shows two peaks, one at 600nm and the other at 685nm. In contrast, the spectrum recorded from the same Au tip at the position of about 3 $\mu$ m away from the apex is similar to the spectrum recorded from smooth Au surfaces. The difference of the two spectra demonstrates the excitation of the surface plasmons at the apex of the Au tip. Similarly, the slightly different integrated area of these two spectra is consistent with the only weakly enhanced emission at the apex. The two peaks of the spectrum 1 in Fig. 6.5 (c) indicate two distinct resonant frequencies of the surface plasmons. It may be due to both perpendicular and parallel collective oscillations of electrons which were excited with respect to the tip axis<sup>[166]</sup>. To prove this explanation, the polarization of the emitted light should be investigated in the future. The varying emission properties of these three Au tips demonstrate the excitation of surface plasmons and the consequent local field enhancement at the apex are very sensitive to the actual geometry of the Au tips. Similar phenomena were observed in scattering spectra of the evanescent waves by Au tips<sup>[166]</sup>.

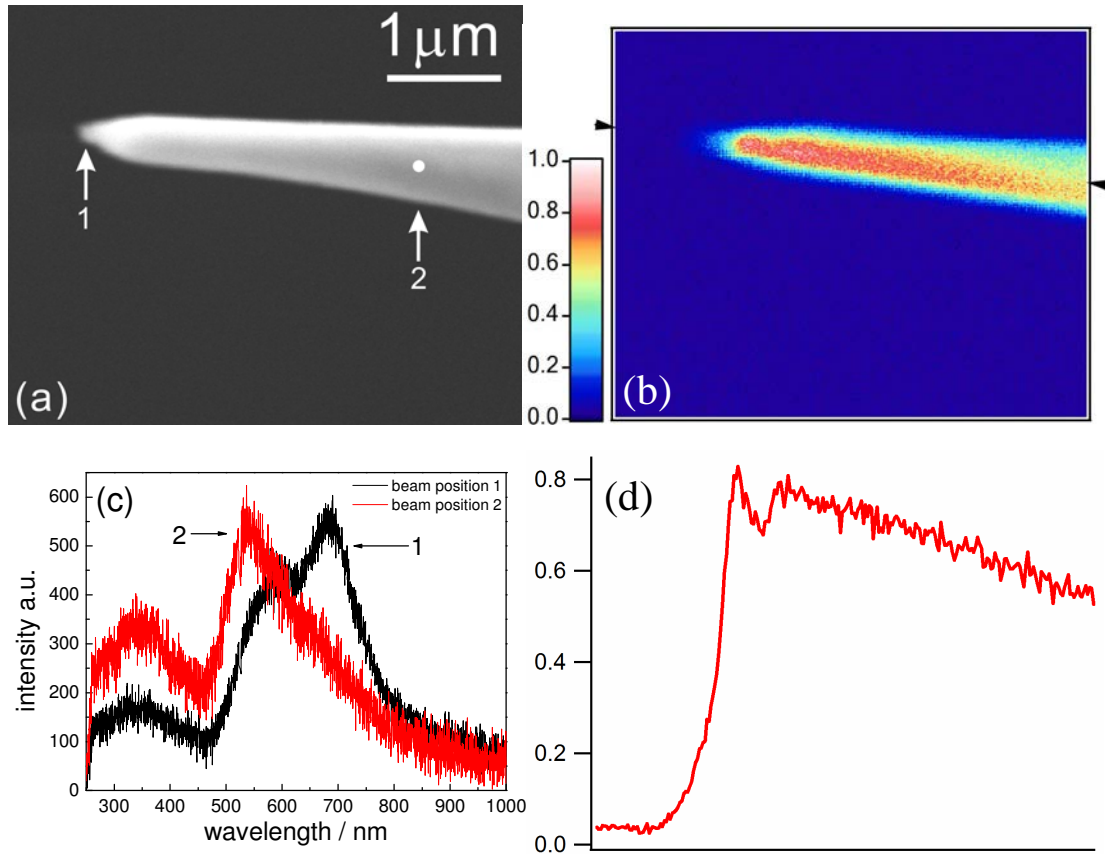


Fig. 6.5 (a) SEM image of an Au tip and (b) its corresponding CL image, irradiated with a 20keV, 1nA electron beam, the dwell time was 10ms/pixel, the maximum counting rate (268 counts/10ms) was normalized to 1; (c) the spectra were obtained from two electron beam (15keV, 3nA) irradiated positions indicated in (a), the integration time was 50s and the; (d) the intensity profile along the tip axis, indicated by arrows in (b).

When the apex diameter of Au tips suddenly enlarges, for example the Au tips were ended with an ellipsoid, as shown in Fig. 6.6 (a) and (c), the maximum emission was usually found at the ellipsoid for both cases. The intensity of the light emitted from the ellipsoid was enhanced by a factor of 3 with respect to the light from the rest part of the tip, though the diameter of the rest part of tip is much smaller than the diameter of the ellipsoid. Compared to the slightly enhanced emission at the apex of the Au tips discussed in previous sections, the strongly enhanced emission upon irradiation at the ellipsoids indicates an easier excitation of surface plasmons and a higher field enhancement near the ellipsoid. The spectra in Fig. 6.6 (e) show that the light emitted at the ellipsoid is peaking at 560nm. The peak position shifts only about 20nm from the peak position of transition radiation at 540nm. However the integrated area of the spectrum is much higher, which is in accordance with the CL image. Though the emission intensity was enhanced, using such tips for tip-enhanced spectroscopy would be in expense of the spatial resolution, due to their large diameter.

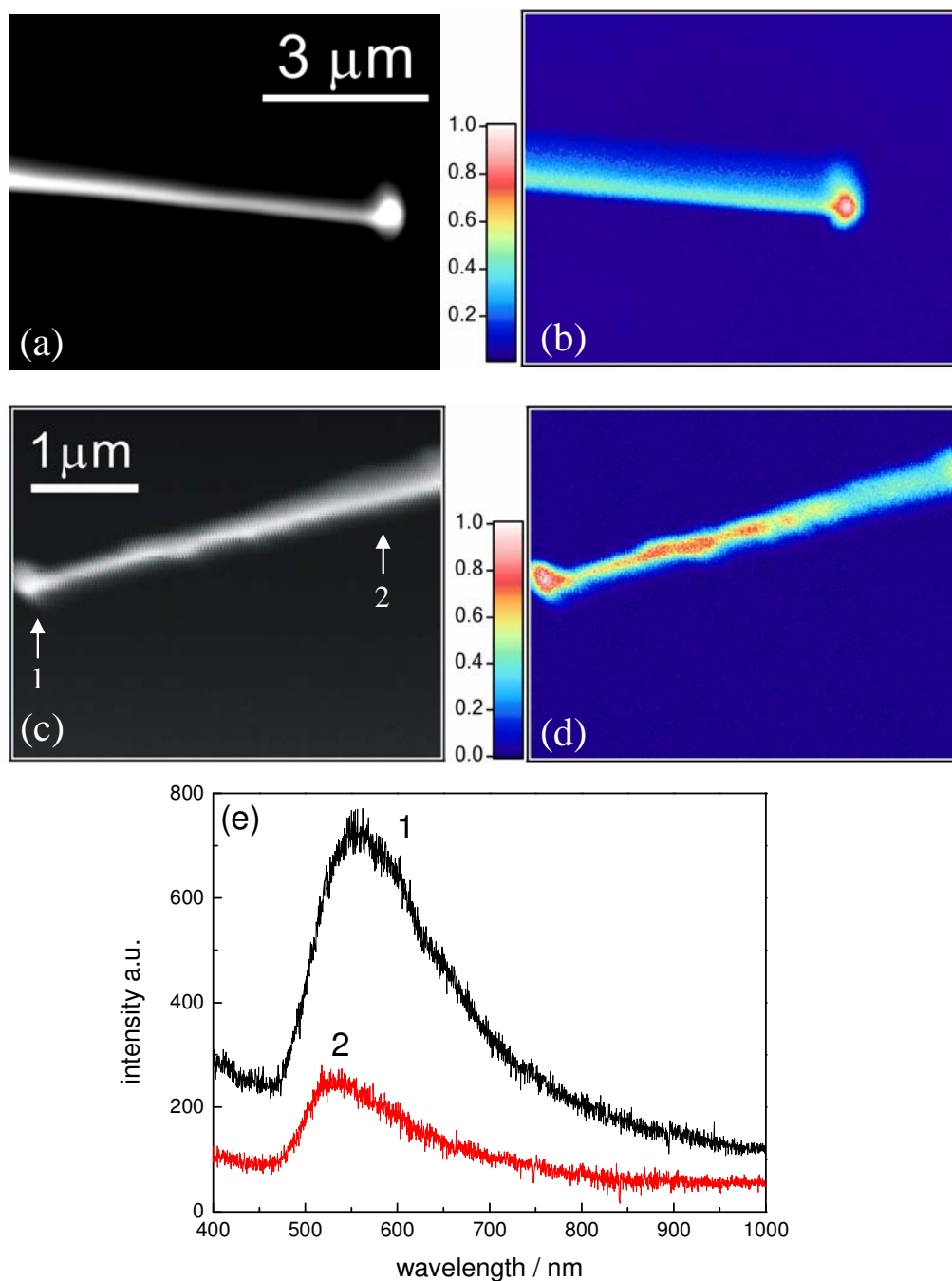


Fig. 6.6 (a) and (c) SEM images of two Au tips with an ellipsoid at the apex; (b) and (d) their corresponding panchromatic cathodoluminescence images (15keV, 9nA for (b) and 15keV, 3nA for (d)), the maximum intensity (b:1031, d:297) was normalized to 1, the dwell time for both images was 10ms/pixel; (e) the spectra were obtained from two electron beam irradiated positions indicated in (c), irradiated with a 15keV, 3nA electron beam and the integration time was 50s.

In order to irradiate the cone of the apex along the tip axis, the tips were arranged with their axis parallel to the incidence of the electron beam. Limited by the depth of focus of the scanning electron microscope, only the sharp end of the Au tip was imaged and is shown in Fig. 6.7 (a). This was helpful for placing the electron beam at the apex of the tip, though the axis of the tip was not perfectly parallel to the incident direction of the electron beam in this case. Upon irradiation of the apex with electrons, the emitted light was peaking at 600nm, which was different from the light emitted from another position indicated in Fig. 6.7 (a). This reveals that surface plasmons were excited at the apex of Au tip with the resonance at 600nm.

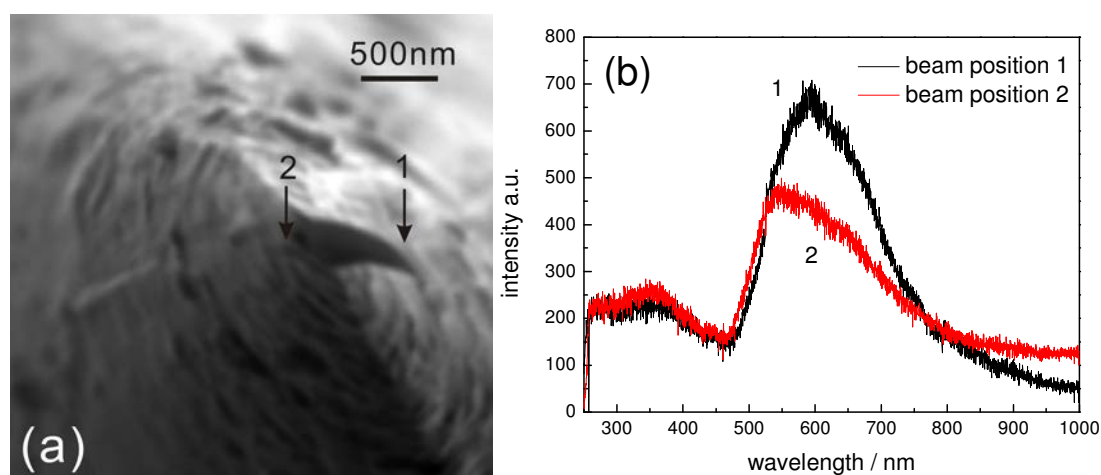


Fig. 6.7 (a) SEM image of an Au tip with its axis almost parallel to the incidence of an electron beam; (b) the spectra were obtained from two electron beam irradiated positions indicated in (a), irradiated with a 15keV, 3nA electron beam, the integration time was 50s.

## 6.5 Conclusions and outlook

The optical properties of Ag tips and Au tips were studied with cathodoluminescence in this chapter. Enhanced emission was found upon electron beam irradiation at the apex of the Ag tips. The enhanced emission spot confined at the apex of the Ag tips has a diameter of a few 100nm. The radiative decay of excited surface plasmons at the apex was the reason for the enhanced emission, which was peaking at about 360nm.



In the case of Au tips, a significant enhancement of the light emission upon irradiation of the apex was rarely observed. However, the spectral measurements revealed that the light emitted when the electron beam irradiated the apex of the Au tips was typically peaking around 600nm, which was different from the peak position of transition radiation of gold. The CL images and the spectra demonstrate the weak excitation of surface plasmons at the apex of the Au tips by the electron beam. The spectra depended on the detailed shape of the tip, which indicates that the excitation of surface plasmons is sensitive to the geometry of the Au tip.

Angularly resolved measurements have been conducted but we were unable to record sufficiently intense projected images so far. In the case of Au tips, as mentioned above, no obvious enhancement at the apex was observed and the emission intensity was relatively low. In order to gain sufficient light to record a projection image with a typical exposure period of 2min, a high beam current up to a few 10nA has to be used. Upon the high beam current, the resolution of the SE image is low and the location of the electron beam at the apex of the tip is not well defined. For the case of Au nanostructures, the emission was strongly increased when the electron beam irradiated the structures and the focused light spot in-situ monitored by a CCD camera would become much more bright when the electron beam going from the unstructured gold surface to the structures. In that case it was easy to locate the electron beam at a spot with high emission intensity. However, in the case of Au tips, the emission intensity was almost constant for all irradiation positions at the tip. Therefore it was hard to locate the beam to the spot where the surface plasmons could be strongly excited. Only green background was recorded for the gold tips and no red light pattern was observed.

The CCD chip of the camera we use in the current experiments is insensitive to UV light. Additionally, the energy of bulk plasmons and surface plasmons of silver are too close to be discriminated by the color of the CCD images. These limit the applications of the CCD projection images to find out the emission angles of light upon surface plasmons of silver. Narrow band filters may solve this problem and the angularly resolved measurements of the tips will be conducted deeply in the future.

# Chapter 7 Light emission from scanning tunneling microscope

## 7.1 Light emission induced by inelastically tunneling electrons in an STM

Light emission induced by inelastically tunneling electrons was first observed from a metal-oxide-metal tunneling junction by Lambe and McCatthy<sup>[185]</sup> in 1976, before the invention of scanning tunneling microscope (STM)<sup>[186]</sup>. Soon after the invention of the scanning tunneling microscope, the local light emission from a nanometer tunneling gap between a metal tip and a Si(111) single crystal or an Ag film was first reported by Gimzewski and Coombs et al.<sup>[17, 18]</sup>. This was the starting point of the wide investigations on the STM induced light emission. Since a relatively high bias voltage is applied to a tip, inelastic tunneling channels are opened in addition to the predominately elastic tunneling<sup>[187]</sup>. As sketched in Fig. 7.1, the strongly confined inelastically tunneling electrons excite localized surface plasmons inside a nanometer cavity formed by a tip and a sample. These tip induced surface plasmons are probably aligned along the axis of the tip. They are oscillating vertically to the sample surface<sup>[188, 189]</sup> and have dipolar character. These so called gap plasmons can emit light directly like a dipolar oscillator. For example, light emitted from an Au-Au tunneling gap was imaged with a inverted optical microscope by Bharadwaj et al. recently<sup>[72]</sup>. The image showed a minimum intensity along the tip axis, which demonstrates that the tip induced gap plasmons oscillated along the tip axis<sup>[72]</sup>. Compared to conventional tunneling spectroscopy where the contribution of inelastic tunneling to the total tunneling current is considerably small, the light emitted from the gap stems mainly from inelastic tunneling, since the contribution of the elastically tunneling hot electrons by subsequent radiative energy loss can be neglected for metals<sup>[188]</sup>. The quantum efficiency of STM induced light emission is of the order of  $10^{-4}$  to  $10^{-5}$

photon per electron, as found in theoretical calculations<sup>[75]</sup> and experimental measurements<sup>[182]</sup>. The quantum efficiency is dependent on the materials of the tip and the substrate. Therefore, an efficient collection optics is very important to collect considerable light for recording photon maps and spectra with moderate tunneling currents<sup>[188]</sup>.

Intensity and frequency of emitted light reflect the characters of a tunneling gap<sup>[189, 190]</sup>, e.g., geometry and local dielectric properties of the gap. Although the excitation of the gap plasmons can be strongly confined inside the gap by the tips, the light source could extend from the gap due to excitation of propagating surface plasmons<sup>[72, 77]</sup>, which can travel a few micrometers from the gap. As sketched in Fig. 7.1, surface plasmons going to the left direction may be scattered into light by an edge. In this case, the emitted light does not directly reflect the properties of the tunneling gap, but rather the scattering properties of the surface defects for the propagating surface plasmons. On the other hand, surface plasmons traveling to the right direction in Fig. 7.1 on a perfect surface would be internally damped without radiation, since the momentum conservation is not fulfilled. On the smooth surface without contribution from the propagating surface plasmons, light stems solely from the tunneling gap and directly reflect the properties of the tunneling gap. However, as mentioned in chapter 2, if thin enough metal films are used as samples, the propagating surface plasmons may couple to light at a metal/dielectric (quartz or glass) interface with a specific emission angle given by Kretschmann's relation  $K_{spp} = (n\omega \sin\theta_L)/c$  ( $K_{spp}$  is the wave vector of propagating surface plasmons,  $n$  is the refractive index of the dielectric medium,  $\theta_L$  is the emission angle and  $\omega/c$  is the wave vector of the emitted light)<sup>[1]</sup>, although the propagating surface plasmons are excited on the other side. Such leakage radiation was experimentally observed and in turn proved the generation of the propagating surface plasmons on smooth Au films by the gap plasmons<sup>[72, 76, 77]</sup>.

Compared to the excitation of surface plasmons by high energy electrons in the SEM which has already been discussed in chapter 5, scanning tunneling microscope induced light emission may provide several advantages: i) the excitation of surface plasmons is more strongly confined, in the extreme with atomic resolution<sup>[191]</sup>; ii) the

considerable contribution of transition radiation upon high energy electrons can be eliminated<sup>[188]</sup> and the radiation purely reflects the properties of excited plasmons; iii) a possible contamination, due to deposition of a carbon film from trace of organic gases in the SEM<sup>[125]</sup>, can be avoided.

Light emission induced by an STM from Au films<sup>[192, 193]</sup> and Au nanoparticles<sup>[189]</sup> has already been investigated. Since the spatial intensity and spectral distribution of the emitted light reflect the electromagnetic near field of the nanostructures<sup>[194]</sup>, in this chapter we tend to investigate the optical properties of the electrochemically fabricated Au structures with STM induced light emission. In comparison with the electromagnetic near field inside a tunneling gap formed between an Au tip and a flat Au surface, as well the emitted light from such gap, we aim to understand the structure dependent electromagnetic near field distribution by proper design of Au structures, e.g., gap geometry and the local dielectric properties dependent emission, where the gaps are formed between an Au tip and Au structures.

Since the Au structures are usually fabricated on 0.1mm thick Au foils, the emitted light is detected in the Au/air hemi-space. The photon maps are simultaneously recorded with the STM topographies. However we still face several experimental problems, for example, oxidation of the gold surface upon tunneling with high bias voltages and high tunneling currents under ambient conditions, which lead to small light emission intensity and unstable tunneling conditions. Therefore, here we just present rather preliminary results. The spectrally resolved measurements are not carried out.

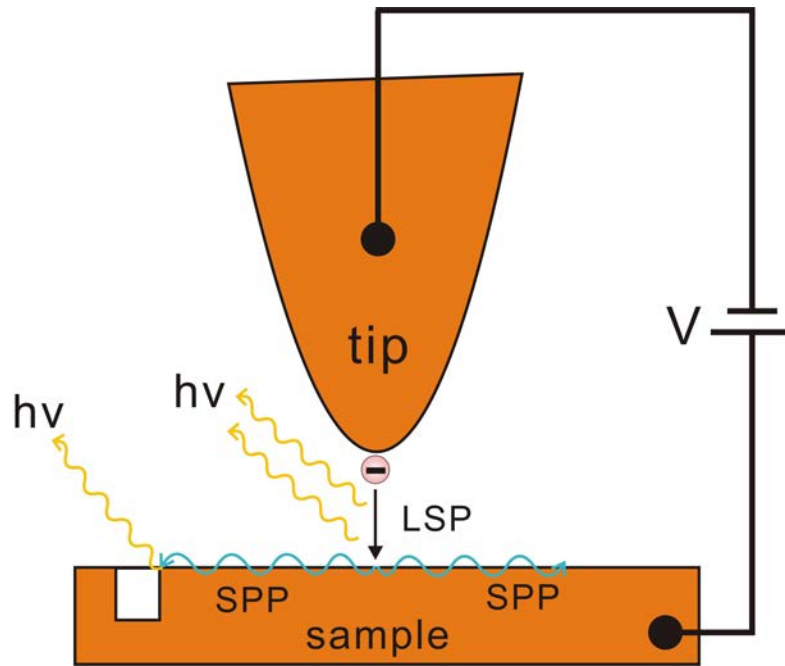


Fig. 7.1 Scheme of tip induced light emission by inelastically tunneling electrons in a scanning tunneling microscope.

## 7.2 Home-built scanning tunneling microscope for light emission investigations

The quantum efficient is not higher than the order of  $10^{-4}$  photon per electron for STM induced light emission<sup>[182]</sup>. Therefore, compared to a conventional scanning tunneling microscope, optimum light collection is one of the main experimental challenges in light emission STM. Considering the requirements of mechanical rigidity for the conventional STM, the space left for the light collection optics is usually very limited<sup>[188]</sup>. Directly placing a photomultiplier<sup>[192]</sup> or (single or multiple) optical fibers<sup>[195, 196]</sup> close to the tunneling gap is a simple optical set-up to collect the emitted light. A condenser lens<sup>[197, 198]</sup> or an optical microscope objective<sup>[72, 77]</sup> with a high numerical aperture (NA) is also commonly used to collect the light. In order to gain more space and wide open angles for the condenser lenses, the tips are usually not arranged vertically to samples<sup>[197]</sup>. Ellipsoidal<sup>[182]</sup> and parabolic reflectors<sup>[189, 199]</sup> can achieve very high collection efficiencies by placing the tunneling gap at the focal

point of these reflectors. In Addition to the considerations about the arrangement the light collection optics, in our experiment, an individual Au nanostructure has to be mechanically located within the scan range of the tip. The typical scan range of a STM piezo of the order of  $\pm 1\mu\text{m}^{[200]}$  is still very small compared to the resolution of a micrometer screw. In order to improve the resolution of the micrometer screws, a lever mechanical part was constructed. A detail of the lever part, sitting beneath the sample is shown in the inserted image in Fig. 7.2 (a). The ratio of the displacement of the micrometer screw to the displacement of the sample is about 10. The lateral adjustment of the sample is monitored by an optical microscope with a long working distance objective (EO Edmund, PLAN APO, 10x/0.28, WD=33.5mm), which is not shown in Fig. 7.2 (a). Under observation with the optical microscope, the tip is first coarsely approached to the sample. Then the tip is brought into the tunneling position with a lever mechanism driven again by a micrometer screw. For light detection, a photomultiplier tube (DIA-LOG) with a 50mm diameter cathode was placed as close as possible to the tunneling gap. The photomultiplier is optically sensitive from 320nm to 850nm with maximum response at 375nm. The distance from the tunneling gap to the cathode of the photomultiplier tube (PMT) is about 30mm. Because of the large diameter of the cathode, maximum collection solid angle was estimated to be about  $0.45\pi$ , even higher than the solid angle of the multi-optical fibers used for cathodoluminescence detection, as described in chapter 3. In order to achieve the highest sensitivity, the PMT is operated in single photon counting mode, where the light generated charge pulses, output from the PMT, are converted to TTL-pulses, whose rate is determined by a counter. The mechanical part of the STM shown in Fig. 7.2 (a) and the PMT are placed on a vibration isolation stage, enclosed with a black wooden box to avoid the stray light during the light emission measurements.

The electronic set-up of the scanning tunneling microscope is sketched in Fig. 7.2 (b). The sample is biased by a tunneling voltage  $U_{\text{bias}}$  and tunneling current is fed into a current-voltage converter. 10mV output corresponds to 1nA tunneling current. Since the tunneling current is exponentially dependent on the tip-sample distance, a log amplifier is used to linearize the current to the tunneling distance. The tunneling

current is then compared with the set current and the difference between them is amplified by an error amplifier. The error is integrated and then the output of the integrator drives the movement of the piezo in z-direction via a high voltage amplifier to make the tunneling current equal to the set current. The equilibrium position of the tip in z-direction is recorded by a computer via a National Instruments DAQcard (PCI 6251). The DAQcard has a maximum voltage range accuracy of 1.92mV (analog input). Scanning patterns driving the tip scan across the samples are also generated by the PCI6251 DAQcard. The scanning patterns output from the DAQcard is amplified by high voltage amplifiers with a maximum output of  $\pm 220\text{V}$ , in order to achieve a maximum scan range of the piezo of about  $5 \times 5\mu\text{m}^2$ . In order to simultaneously obtain the photon maps and topography, the charge pulses output from the PMT are also counted by a counter of the PCI 6251 DAQcard. This procedure is similar to the recording of the photon maps described in chapter 5. All STM induced light emission experiments are conducted under ambient conditions.

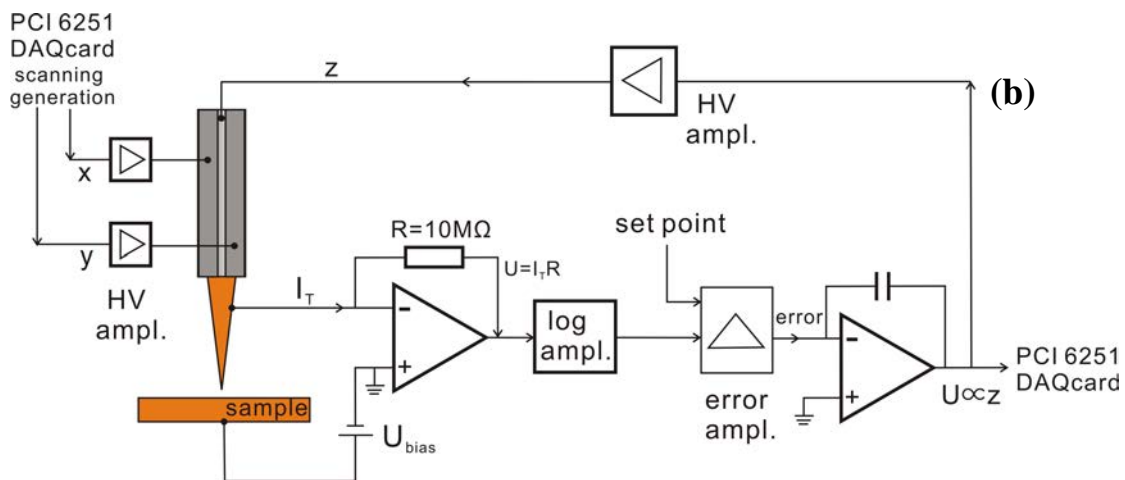
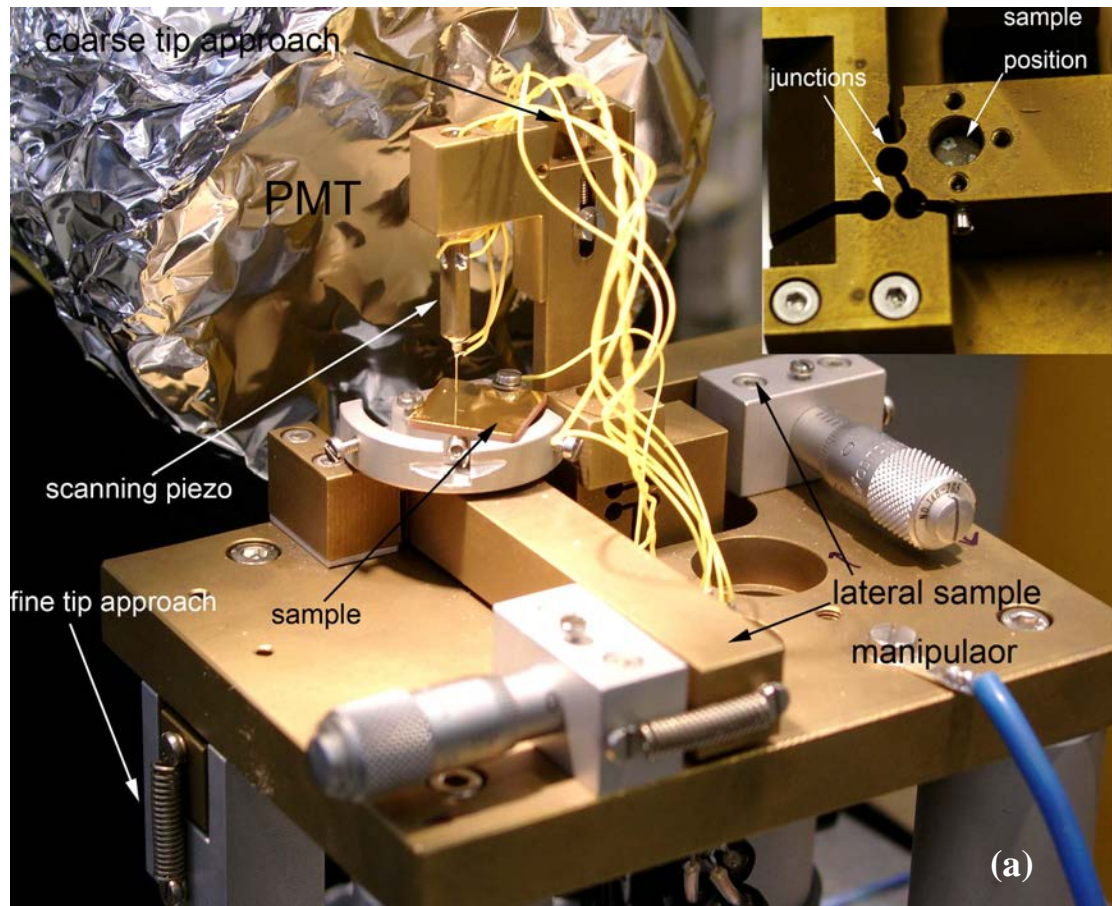


Fig. 7.2 (a) Photograph of a home-built scanning tunneling microscope, the inserted image shows details of the lever mechanism of the sample manipulator; (b) Scheme of the electronics of the scanning tunneling microscope.

Tungsten (W), platinum (Pt) and platinum/iridium (Pt/Ir) tips are widely used for high resolution scanning tunneling microscope images due to their hardness and easy preparation. However due to the large imaginary part of the complex dielectric



constants in the visible and near-infrared spectral regime of those materials, the dielectric losses are too strong for these materials to gain high emitted light intensities<sup>[188, 190, 195]</sup>. For example, light emitted from a W-Au tunneling gap was reported to be more than one order of magnitude lower, compared to the light emitted from an Au-Au<sup>[72, 190]</sup> or from an Au-Ag<sup>[77]</sup> tunneling gap, since the excited localized surface plasmons were efficiently quenched by the W tip. Hence Au tips are usually used in order to obtain high quantum efficiencies, though their softness may lead to unstable tunneling and relatively low resolution.

As mentioned above, the positioning of the tip in the vicinity of an individual Au structure within the scan range of the piezo tube is fairly difficult. One straightforward way to solve this problem is by fabrication of many similar structures in a relatively wide area in order to increase the chance to hit one of them. Fig. 7.3 (a) shows an SEM image of an array of triangles in a  $27 \times 32 \mu\text{m}^2$  area, spaced by about  $10 \mu\text{m}$ . The sides of the triangles are about  $1 \mu\text{m}$  long and the trough is about  $350 \text{nm}$  wide and about  $600 \text{nm}$  deep. They were fabricated into an Au foil with a pulse train of  $5.6 \text{V}$ ,  $11 \text{ns}$  and the machining time for each triangle was about  $15 \text{min}$ . Fig. 7.3 (c) shows an STM image of a triangle, which is indicated by an arrow in the STM image. Its corresponding SEM image is shown in Fig. 7.3 (b). The quality of the STM image is rather low. At least the contrast is not good enough. The trough enclosed the triangle is about  $600 \text{nm}$  deep and  $350 \text{nm}$  wide. However, it is not very obvious in the STM image in Fig. 7.3 (c). This is probably caused by the large scan range and the size of the apex of the Au tip. If the Au tip with a curvature radius larger than the width of the trough, it could not approach the bottom of the trough when it scanned across the triangle. Furthermore, probably due to insufficiently stable tunneling conditions, the structure was mechanically affected during the scanning. An SEM image of a triangle after repetitive scanning with high tunneling current, i.e., small tunneling distance, is shown in Fig. 7.4 (b)

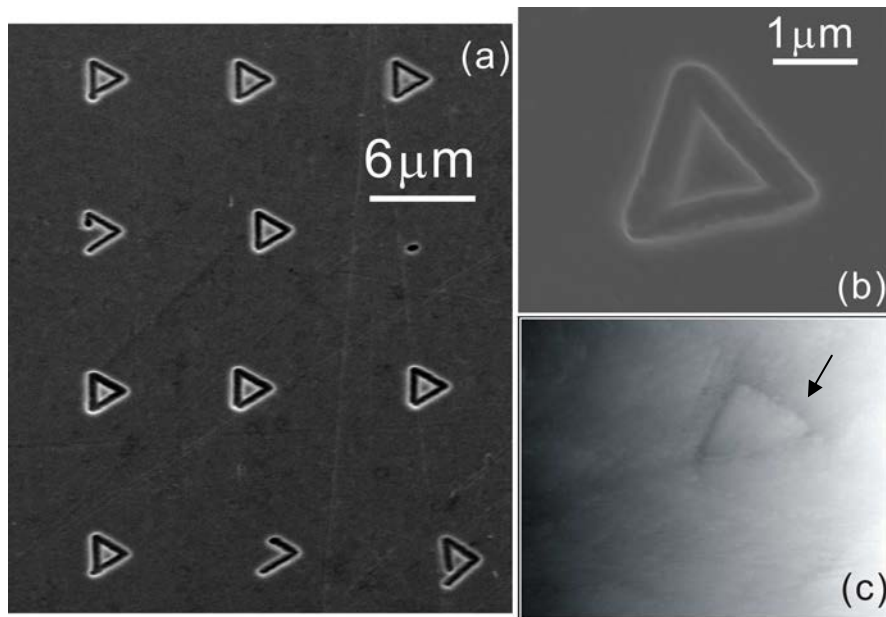


Fig. 7.3 (a) SEM image of triangles fabricated into a gold foil with a 5.6V, 11ns voltage pulse train; (b) high magnification SEM image of one triangle and (c) its corresponding STM image ( $U_T=100\text{mV}$ ,  $I_T=10\text{nA}$ ).

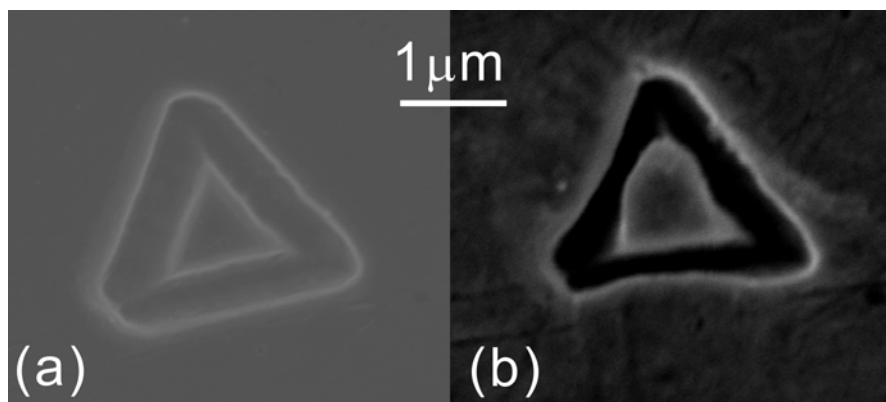


Fig. 7.4 SEM image of a triangle fabricated on a gold foil, imaged (a) before a tip scanned across and (b) after a tip scanned across.

## 7.3 STM induced light emission

### 7.3.1 Light emission from flat gold films

Fig. 7.5 shows the intensity of light emitted from an Au film evaporated onto a quartz substrate upon tunneling with an Au tip ( $U_T = -3V$ ,  $I_T = 10nA$ ). 60 measurements were taken from 3 different positions. The time interval between the measurements was 2s. The unstable emission with time is indicated in Fig. 7.5. Usually the first measurement after application of -3V was the highest. Then the intensity rapidly decreased and stayed relatively stable after 10 measurements. An average counting rate of 1000 per second was observed. This is in accordance with the observations of Bischoff et al.<sup>[201]</sup>. They induced light emission from an Au-Au gap by 1.8V, 20nA tunneling electrons in air. A water meniscus would be formed in the nanometer gap under ambient conditions due to the capillary condensation<sup>[202]</sup>. The emission intensity from Au-Au tunneling gaps as a function of relative humidity was carefully studied by Boyle et al. recently and the emission intensity decreased with increasing relative humidity<sup>[203]</sup>. In the presence of the water meniscus, the surface of the gold film might be oxidized by application of 3V, similar to the localized oxidation of silicon surface induced by AFM tips<sup>[54, 204]</sup>. Therefore, the low and the fluctuation of the emission intensity can be attributed to surface oxidation of the Au film and the unstable tunneling current upon 3V bias voltage under ambient conditions, as well the possible contamination of the Au tip<sup>[195]</sup>. To estimate the quantum efficiency of the light emitted from the Au-Au tunneling gap, we assume a typical count rate of 1000 with  $6.25 \times 10^{10}$  tunneling electrons per second (10nA). Taking a quantum efficiency of the PM cathode of 10% at 550nm and the maximum collection efficiency of 20% into consideration, the quantum efficiency is about  $10^{-6}$ , which is about one order of magnitude lower than Gallagher et al.'s measurements of  $10^{-5}$  at  $U_{bias}=2.0V$ <sup>[195]</sup> in air. We ascribe this to the strongly electrochemical oxidation of the Au surface upon application of  $U_{bias}=3.0V$  under ambient conditions.

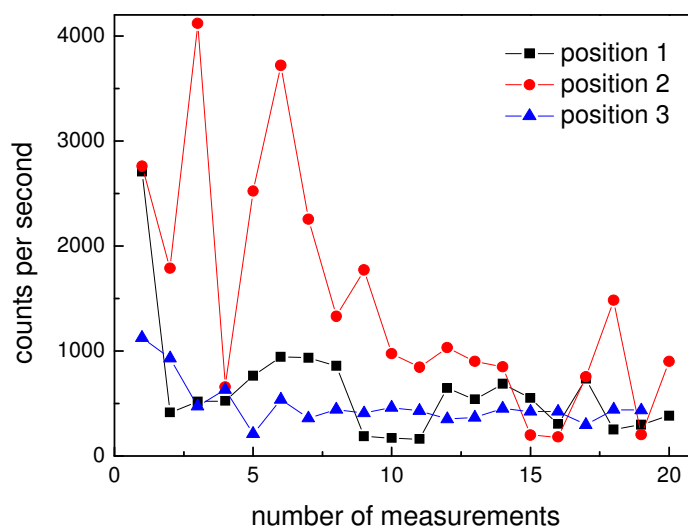


Fig. 7.5 Counting rate of photons emitted from an Au-tip/Au-film gap during 20 subsequent measurements (interval 2min) at three positions; The dark counts were subtracted.

In order to reveal the main emission angle of the light, a 3mm wide aperture was placed between the tunneling gap and the photomultiplier at a distance of 8mm from the tunneling gap. By stepwise vertical movement of the aperture, intervals of the collection angle of  $0 - 20.6^\circ$ ,  $20.6 - 36.9^\circ$  and  $36.9 - 48.4^\circ$  with respect to the sample surface were defined. The emitted light intensity obtained from these three emission angle intervals is plotted in Fig. 7.6 together with the counting rate without aperture. For every angle interval, 10 subsequent measurements were taken. As can be clearly seen from the Fig. 7.6, the highest light intensity was observed at the emission angle interval between  $20.6^\circ$  and  $36.9^\circ$ . Notice that sum of the emission intensity obtained at the emission angle interval of  $0 - 48.4^\circ$  is slightly higher than the counting rate without aperture. We ascribe this to the stray light and the missing subtraction of the dark counts. In addition, the tunneling gap was unstable, which resulted in fluctuations of the emission intensity. The whole experiment was repeated several times, which all showed an emission angle interval between  $20.6^\circ$  and  $36.9^\circ$  had maximum intensity. As mentioned above, the direct emission from the gap plasmons was the main contribution to the observed light in Fig. 7.6. The angular distribution of

the emitted light is dependent on the orientation of the induced dipole. The gap plasmons induced by inelastically tunneling electrons is oscillating vertically to the samples surface<sup>[188, 189]</sup>. Thus, the maximum emission angle of  $35^\circ$  with respect to the surface was predicted from the theoretical calculations<sup>[205, 206]</sup>. Experimentally, Yamamoto et al.'s results indicate that light originating from a dipole oscillating along the surface normal mainly emits in the zenith angles between  $20^\circ$  to  $40^\circ$  with respect to the sample surface<sup>[162]</sup>. These are in accordance with our observation, as shown in Fig. 7.6.

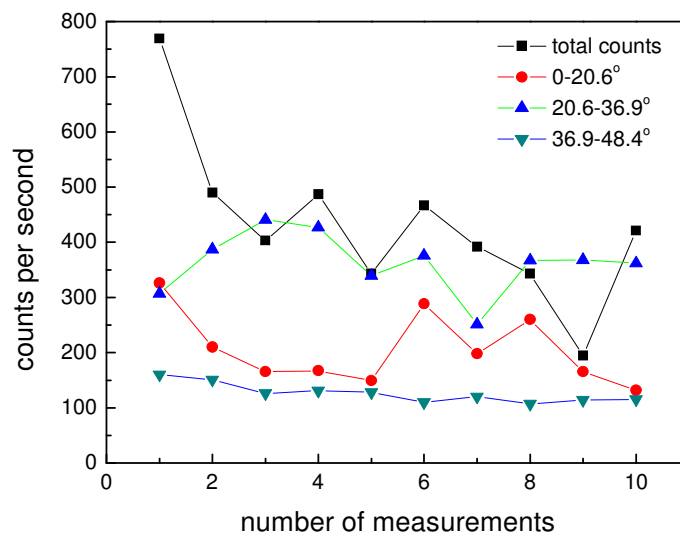


Fig. 7.6 Plots of counts of photons emitted from an Au - Au tunneling gap per second, obtained from various open angle intervals with respect to sample surface, upon 3.0V bias voltage and 10nA tunneling current; background was not subtracted.

### 7.3.2 Light emission from gold microstructures

Fig. 7.7 (b) shows a photon map of an Au triangle induced by tunneling electrons with an Au tip ( $I_T = 60\text{nA}$  and  $U_{\text{bias}} = -2.0\text{V}$ ). Time for photon counting was 5ms per pixel. Obviously, the light intensity increased when the tip was close to the edges of the trough. There are two possible reasons for the observation of the increased intensity near the edges of the trough: i) effective scattering of propagating surface plasmons, ii) effective excitation of localized surface plasmons near the edges. The propagation

lengths of surface plasmons on gold surfaces are expected to be of the order of several micrometers in the visible and near infrared<sup>[12]</sup>. However the light emitted when the tip was positioned at the center of the triangle is much lower than close to the edge, although the center was less than about 500nm from the edges. Thus the efficient edge scattering of propagating surface plasmons was not the main reason for the enhanced emission upon tunneling at the edges. Efficient excitation of localized surface plasmons near the edges of the trough probably significantly contributed to the enhanced light intensity.

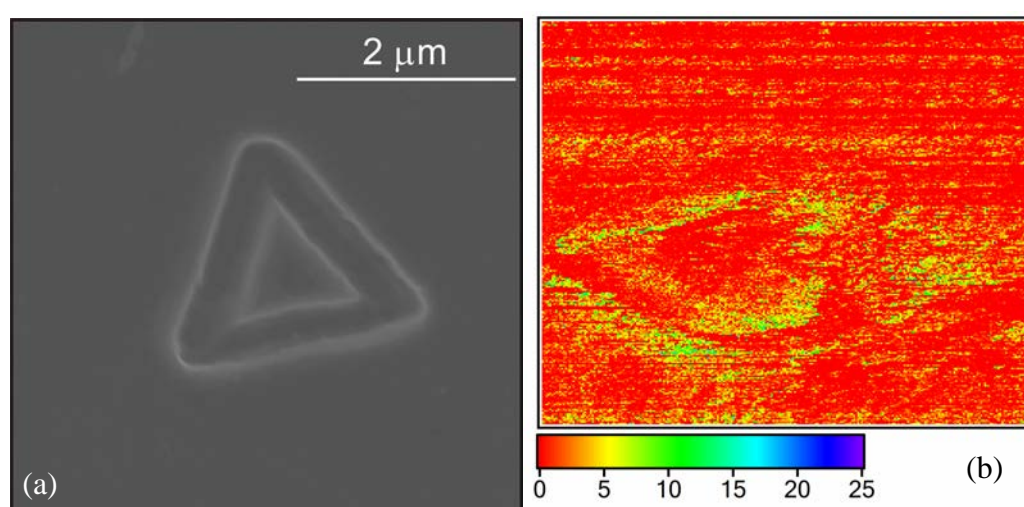


Fig. 7.7 (a) SEM image of a triangle fabricated on an Au foil and (b) its corresponding photon map indicated in STM with the following parameters:  $U_T = -2.0V$ ,  $I_T = 60nA$ , 5ms/pixel.

## 7.4 Conclusions, problems and outlook

In this chapter, a home-built STM equipped with a lateral manipulator was constructed for position of an individual, electrochemically fabricated Au structure within the scan range of an Au tip. The main emission angles of light upon tunneling on a flat Au film were found to be between  $20.6^\circ$  and  $37^\circ$  with respect to sample surface. The emitted light is ascribed to the excitation of localized gap plasmons, which aligned along the tip axis. Similarly, also upon tunneling across an electrochemically fabricated Au triangle, the enhanced light emission near the edges

of the triangle can be ascribed to the effective excitation of localized surface plasmons at the edges.

In order to achieve sufficient emission intensity, high bias voltages of the order of 3V and high tunneling currents were applied. The present experiments were carried out under ambient conditions. These conditions caused strong fluctuations of the emitted light intensity and an unstable tunneling process. Furthermore, mechanical deformation of the structures was observed after repetitive scanning. In order to solve these experimental problems, combination of the STM and the SEM and using the parabolic mirror optics, which has already been installed inside the SEM, are taken into consideration to collect the light emitted from the tunneling gap and to obtain the angular distribution of the emitted light. These experiments could provide several advantages: i) vacuum environment, the formation of water meniscus inside the tunneling gap and the electrochemical oxidation of sample surfaces can be avoided to achieve more stable tunneling process and high quantum efficiency of light emission upon tunneling electrons; ii) imaging with the SEM, position of an individual structure inside the tunneling gap and addressing of the tunneling gap to the focal point of the parabolic mirror become easier and the in-suit characterization of the tip and the gap geometry become possible.

# Appendix

The Cartesian coordinates of the coordinate system were defined in Fig. 5.6 in chapter 5. The focal length of our parabolic mirror is 2mm and the focal point of the parabolic mirror is at the origin. Surface of the parabolic mirror can be described by equation A.1. The width of the mirror ranges between -7.5 and 7.5 on the x-axis and the height of the mirror ranges between 0.5 and 8 on the z-axis. Equation A.2 and equation A.3 relate the azimuthal angle  $\varphi$  and zenith angle  $\theta$  to x, y, z coordinates. The following calculations are adopted from Dana and Wang's calculations<sup>[157]</sup>.

$$(y + 2) = \frac{x^2 + z^2}{8} \quad (-7.5 \leq x \leq 7.5, 0.5 \leq z \leq 8) \quad (\text{A.1})$$

$$\tan \varphi = \frac{y}{x} \quad (\text{A.2})$$

$$\sin \theta = \frac{\sqrt{x^2 + y^2}}{\sqrt{x^2 + y^2 + z^2}}. \quad (\text{A.3})$$

By combination of equation A.1 and equation A.2, the relation between azimuthal angle  $\varphi$  and (x, z) is obtained, as expressed by equation A.4:

$$\varphi(x, z) = \arctan \left( \frac{x^2 + z^2 - 16}{8x} \right). \quad (\text{A.4})$$

For the calculation of the zenith angle  $\theta$ , equation A.5 is obtained by combination of equation A.1 and equation A.3<sup>[157]</sup>:

$$\sin \theta \sin \varphi = \frac{y}{y + 4}. \quad (\text{A.5})$$

After the azimuthal angle  $\varphi$  has been obtained as a function of (x, z), the zenith angle  $\theta$  is also expressed as a function of x and z:

$$\theta(x, z) = \arcsin \left[ \left( \frac{x^2 + z^2 - 16}{x^2 + z^2 + 16} \right) \cdot \frac{1}{\sin \varphi} \right]. \quad (\text{A.6})$$

Light emitted into a unit solid angle is reflected and projected into a spot on the image plane. The spot area is dependent on the emission direction ( $\theta, \varphi$ ). Assuming that light is emitted from the focal point of the mirror into an infinitesimal solid angle  $d\Omega$  with



direction  $(\theta, \varphi)$  and is reflected by the mirror surface at distance  $r(\theta, \varphi)$  from the origin into a parallel beam with a cross section  $dA(\theta, \varphi)$ , then  $dA(\theta, \varphi)$  is simply given by the cross section of the diverging beam with  $d\Omega$  at the position, where it hits the mirror surface, i.e. at distance  $r(\theta, \varphi)$  from the origin. The infinitesimal area  $dA(\theta, \varphi)$ , which is identical to the area of the beam spot at the projected plane if the parallel beam is not extended or focused, e.g., by a lens, is given by equation A.7:

$$dA(\theta, \varphi) = r^2 d\Omega = r^2 \sin \theta d\theta d\varphi \quad (\text{A.7})$$

with  $r^2 = x^2 + y^2 + z^2$ .

By combination of equation A.1 and equation A.7, the relationship of the surface area at the image plane per unit solid angle of the diverging beam can be calculated by equation A.8:

$$\frac{dA(x,z)}{d\Omega} = \left( \frac{x^2 + z^2}{8} - 2 \right)^2 + x^2 + z^2 = r^2(x,z). \quad (\text{A.8})$$

# Bibliography

- [1] H. Raether, *Surface Plasmons on smooth and rough surfaces and on gratings*, Springer, Berlin, **1988**.
- [2] R. H. Ritchie, *Phys. Rev.* **1957**, *106*, 874.
- [3] C. J. Powell, J. B. Swan, *Phys. Rev.* **1959**, *115*, 869.
- [4] C. J. Powell, *Proc. Phys. Soc.* **1960**, *76*, 593.
- [5] J. L. Robins, *Proc. Phys. Soc.* **1962**, *79*, 119.
- [6] J. Thirlwell, *Proc. Phys. Soc.* **1967**, *91*, 552.
- [7] Y. Y. Teng, E. A. Stern, *Phys. Rev. Lett.* **1967**, *19*, 511.
- [8] G. Sauerbrey, E. Woeckel, P. Dobberstein, *Phys. Stat. Sol. B* **1973**, *60*, 665.
- [9] D. Heitmann, V. Permien, *Opt. Commun.* **1978**, *25*, 196.
- [10] A. Otto, *Z.Phys.* **1968**, *216*, 313.
- [11] E. Kretschmann, H. Raether, *Z.Naturforsch* **1968**, *23a*, 2135.
- [12] A. V. Zayats, I. I. Smolyaninov, *J. Opt. A* **2003**, *5*, S16.
- [13] W. L. Barnes, A. Dereux, T. W. Ebbesen, *Nature* **2003**, *424*, 824.
- [14] E. Ozbay, *Science* **2006**, *311*, 189.
- [15] T. W. Ebbesen, H. J. Lezec, H. F. Ghaemi, T. Thio, P. A. Wolff, *Nature* **1998**, *391*, 667.
- [16] L. Novotny, N. van Hulst, *Nat. Photonics* **2011**, *5*, 83.
- [17] J. Coombs, J. K. Gimzewski, B. Reihl, J. Sass, *J. Microsc.* **1988**, *152*, 325.
- [18] J. K. Gimzewski, B. Reihl, J. H. Coombs, R. R. Schlittler, *Z. Phys. B* **1988**, *72*, 497.
- [19] C. K. Chen, A. R. B. de Castro, Y. R. Shen, *Phys. Rev. Lett.* **1981**, *46*, 145.
- [20] G. T. Boyd, T. Rasing, J. R. R. Leite, Y. R. Shen, *Phys. Rev. B* **1984**, *30*, 519.
- [21] K. Kneipp, Y. Wang, H. Kneipp, L. T. Perelman, I. Itzkan, R. R. Dasari, M. S. Feld, *Phys. Rev. Lett.* **1997**, *78*, 1667.
- [22] S. Nie, S. R. Emory, *Science* **1997**, *275*, 1102.
- [23] R. M. Stokle, Y. D. Suh, V. Deckert, R. Zenobi, *Chem. Phys. Lett.* **2000**, *318*, 131.
- [24] B. Pettinger, B. Ren, G. Picardi, R. Schuster, G. Ertl, *Phys. Rev. Lett.* **2004**, *92*, 096101.
- [25] M. Moskovits, *Rev. Mod. Phys.* **1985**, *57*, 783.
- [26] F. J. García-Vidal, J. B. Pendry, *Phys. Rev. Lett.* **1996**, *77*, 1163.
- [27] J. F. Li, Y. F. Huang, Y. Ding, Z. L. Yang, S. B. Li, X. S. Zhou, F. R. Fan, W. Zhang, Z. Y. Zhou, Y. WuDe, B. Ren, Z. L. Wang, Z. Q. Tian, *Nature* **2010**, *464*, 392.
- [28] C. C. Neacsu, S. Berweger, M. B. Raschke, *Nanobiotechnol.* **2007**, *3*, 172.
- [29] S. A. Maier, *Plasmonics: fundamentals and applications*, Springer, New York, **2007**.
- [30] J. Jersch, F. Demming, L. J. Hildenhagen, K. Dickmann, *Appl. Phys. A* **1998**, *66*, 29.
- [31] F. Demming, J. Jersch, K. Dickmann, P. I. Geshev, *Appl. Phys. B* **1998**, *66*, 593.
- [32] M. Micic, N. Klymyshyn, Y. D. Suh, H. P. Lu, *J. Phys. Chem. B* **2003**, *107*, 1574.
- [33] B. Pettinger, B. Ren, G. Picardi, R. Schuster, G. Ertl, *J.Raman Spectrosc.* **2005**, *36*, 541.
- [34] J. Nelayah, M. Kociak, O. Stéphan, F. J. G. d. Abajo, M. Tencé, L. Henrard, D. Taverna, I. Pastoriza-Santos, L. M. Liz-Marzán, C. Colliex, *Nat. Phys.* **2007**, *3*, 348.
- [35] M. Bosman, V. J. Keast, M. Watanabe, A. I. Maarroof, M. B. Cortie, *Nanotechnology* **2007**, *18*, 165505.

- [36] M. N'Gom, S. Li, G. Schatz, R. Erni, A. Agarwal, N. Kotov, T. B. Norris, *Phys. Rev. B* **2009**, *80*, 113411.
- [37] N. Yamamoto, K. Araya, F. J. G. d. Abajo, *Phys. Rev. B* **2001**, *64*, 205419.
- [38] E. J. R. Vesseur, R. d. Waele, M. Kuttge, A. Polman, *Nano Lett.* **2007**, *7*, 2843.
- [39] C. E. Hofmann, E. J. R. Vesseur, L. A. Sweatlock, H. J. Lezec, F. J. G. de Abajo, A. Polman, H. A. Atwater, *Nano Lett.* **2007**, *7*, 3612.
- [40] E. J. R. Vesseur, R. d. Waele, H. J. Lezec, H. A. Atwater, F. J. G. d. Abajo, A. Polman, *Appl. Phys. Lett.* **2008**, *92*, 083110.
- [41] E. J. R. Vesseur, F. J. G. d. Abajo, A. Polman, *Nano Lett.* **2009**, *9*, 3147.
- [42] R. Schuster, V. Kirchner, P. Allongue, G. Ertl, *Science* **2000**, *289*, 98.
- [43] R. Schuster, *ChemPhysChem* **2007**, *8*, 34.
- [44] J. O. M. Bockris, A. K. N. Reddy, *Modern Electrochemistry, Vol. II*, Plenum, New York, **1970**.
- [45] A. J. Bard, L.R. Faulkner, *Electrochemical Methodes Fundamentals and Applications*, 2nd ed., John Wiley, New York, **2001**.
- [46] H. Guckel, *Proceedings of the IEEE* **1998**, *86*, 1586.
- [47] N. Maluf, *An Introdution to Microelectromechanical Systems Engineering*, Artech House, Norwood, **2000**.
- [48] Y. Xia, G. M. Whitesides, *Angew. Chem. Int. Ed.* **1998**, *37*, 550.
- [49] N. Bityurin, *Annu. Rep. Prog. Chem., Sect. C: Phys. Chem.* **2005**, *101*, 216.
- [50] L. Pain, B. Icard, S. Manakli, J. Todeschini, B. Minghetti, V. Wang, D. Henry, *Microelectron. Eng.* **2006**, *83*, 749.
- [51] A. A. Tseng, *J. Micromech. Microeng.* **2004**, *14*, R15.
- [52] K. Gamo, *Nucl. Instrum. Methods Phys. Res., Sect. B* **1992**, *65*, 40.
- [53] D. S. Ginger, H. Zhang, C. A. Mirkin, *Angew. Chem. Int. Ed.* **2004**, *43*, 30.
- [54] M. Calleja, R. García, *Appl. Phys. Lett.* **2000**, *76*, 3427.
- [55] D. M. Kolb, F. C. Simeone, *Curr. Opin. Solid State Mater. Sci.* **2005**, *9*, 91.
- [56] D. M. Kolb, R. Ullmann, T. Will, *Science* **1997**, *275*, 1097.
- [57] W. Schindler, D. Hofmann, J. Kirschner, *J. Electrochem. Soc.* **2001**, *148*, C124.
- [58] A. J. Bard, M. V. Mirkin, *Scanning electrochemical microscopy*, Marecl Dekker, New York, **2001**.
- [59] J. J. Sun, H. G. Huang, Z. Q. Tian, L. Xie, J. Luo, X. Y. Ye, Z. Y. Zhou, S. H. Xia, Z. W. Tian, *Electrochim. Acta* **2001**, *47*, 95.
- [60] K. H. Ho, S. T. Newman, *Int. J. Mach. Tool Manu.* **2003**, *43*, 1287.
- [61] C. K. Malek, V. Saile, *Microelectron. J.* **2004**, *35*, 131.
- [62] B. N. Chichkov, C. Momma, S. Nolte, F. V. Alvensleben, A. Tünnermann, *Appl. Phys. A* **1996**, *63*, 109.
- [63] S. Nolte, C. Momma, H. Jacobs, A. Tünnermann, B. N. Chichkov, B. Wellegehausen, H. Welling, *J. Opt. Soc. Am. B* **1997**, *14*, 2716.
- [64] M. Kock, Freien Universit'at Berlin (Berlin), **2004**.
- [65] M. Kock, V. Kirchner, R. Schuster, *Electrochim. Acta* **2003**, *48*, 3213.
- [66] V. Kirchner, L. Cagnon, R. Schuster, G. Ertl, *Appl. Phys. Lett.* **2001**, *79*, 1721.
- [67] E. M. Moustafa, O. Mann, W. Fürbeth, R. Schuster, *ChemPhysChem* **2009**, *10*, 3090.
- [68] P. Allongue, P. Jiang, V. Kirchner, A. L. Trimmer, R. Schuster, *J. Phys. Chem. B* **2004**, *108*, 14434.

- [69] H. Raether, *Excitation of Plasmons and Interband Transitions by Electrons*, Springer-Verlag, New York, **1980**.
- [70] J. M. Pitarke, V. M. Silkin, E. V. Chulkov, P. M. Echenique, *Rep.Prog.Phys.* **2007**, *70*, 1.
- [71] N. W. Ashcroft, N. D. Mermin, *Solid State Physics*, Brooks/Cole, salt Lake city, **1976**.
- [72] P. Bharadwaj, A. Bouhelier, L. Novotny, *Phys. Rev. Lett.* **2011**, *106*, 226802.
- [73] Z. K. Tang, P. Sheng, *Nanoscale Phenomena Basic Science to Device Applications* Springer, New York, **2008**.
- [74] G. F. J. d. Abajo, *Rev. Mod. Phys.* **2010**, *82*, 209.
- [75] P. Johansson, R. Monreal, P. Apell, *Phys. Rev. B* **1990**, *42*, 9210.
- [76] K. Takeuchi, Y. Uehara, S. Ushioda, S. Morita, *J. Vac. Sci. Technol. B* **1991**, *9*, 557.
- [77] T. Wang, E. Boer-Duchemin, Y. Zhang, G. Comtet, G. Dujardin, *Nanotechnology* **2011**, *22*, 175201.
- [78] A. V. Zayats, I. I. Smolyaninov, A. A. Maradudin, *Phys. Rep.* **2005**, *408*, 131.
- [79] S. Link, M. A. El-Sayed, *J. Phys. Chem. B* **1999**, *103*, 8410.
- [80] W. A. Murray, W. L. Barnes, *Adv. Mater.* **2007**, *19*, 3771.
- [81] A. Bouhelier, M. R. Beversluis, L. Novotny, *Appl. Phys. Lett.* **2003**, *83*, 5041.
- [82] K. Li, M. I. Stockman, D. J. Bergman, *Phys. Rev. Lett.* **2003**, *91*, 227402.
- [83] D. W. Lynch, W. R. Hunter, in *Handbook of optical constants of solids, Vol. I* (Ed.: E. D. Palik), Academic Press, New York, **1985**.
- [84] C. Corti, R. Holliday, *Gold*, CRC Press, Boca Raton, **2010**.
- [85] P. B. Johnson, R. W. Christy, *Phys. Rev. B* **1972**, *6*, 4370.
- [86] W. Steinmann, *Phys. Rev. Lett.* **1960**, *5*, 470.
- [87] P. Chaturvedi, K. H. Hsu, A. Kumar, K. H. Fung, J. C. Mabon, N. X. Fang, *ACS Nano* **2009**, *3*, 2965.
- [88] L. S. Cram, E. T. Arakawa, *Phys. Rev.* **1967**, *153*, 455.
- [89] M. Fleischmann, P. J. Hendra, A. J. McQuillan, *Chem. Phys. Lett.* **1974**, *26*, 163.
- [90] W. Zhang, B. S. Yeo, T. Schmid, R. Zenobi, *J. Phys. Chem. C* **2007**, *111*, 1733.
- [91] A. Politano, G. Chiarello, *Gold Bull.* **2009**, *42*, 195.
- [92] M. E. Hoenk, K. J. Vahala, *Rev. Sci. Instrum.* **1989**, *60*, 226.
- [93] J. Solé, L. Bausa, D. Jaque, *An introduction to the optical spectroscopy of inorganic solids*, Wiley, West Sussex **2005**.
- [94] Hamamatsu, *Photon counting using photomultiplier tubes*, **1998**.
- [95] I. R. Kenyon, *The light fantastic*, Oxford University Press, Oxford, **2008**.
- [96] T. Coenen, E. J. R. Vesseur, A. Polman, F. Koenderink, *Nano Lett.* **2011**, *11*, 3779.
- [97] K. Takeuchi, N. Yamamoto, *Opt. Express* **2011**, *19*, 12365.
- [98] T. Suzuki, N. Yamamoto, *Opt. Express* **2009**, *17*, 23664.
- [99] R. J. Puddephatt, in *Comprehensive coordination chemistry, Vol. 5* (Eds.: G. Wilkinson, J.A. McCleverty, R. D. Gillard), Pregamon Press, Oxford, **1987**.
- [100] J. H. Gallego, C. E. Castellano, A. J. Calandra, A. J. Arvia, *J. Electroanal. Chem. Interfac.* **1975**, *66*, 207.
- [101] G. M. Schmid, M. E. Curley-Fiorino, in *Encyclopedia of electrochemistry of the elements, Vol. IV* (Ed.: A. J. Bard), Marcel Dekker, New York, **1975**.
- [102] X. Ma, A. Bán, R. Schuster, *ChemPhysChem* **2010**, *11*, 616.
- [103] K. Izutsu, *Electrochemistry in nonaqueous solutions*, Wiley-VCH Weinheim, **2002**.

- [104] I. Persson, *Pure Appl. Chem.* **1986**, 58, 1153.
- [105] A. D. Goolsby, D. T. Sawyer, *Anal. Chem.* **1968**, 40, 1978.
- [106] D. Martin, A. Weise, H. J. Niclas, *Angew. Chem. Int. Ed.* **1967**, 6, 318.
- [107] J. N. Butler, *J. Electroanal. Chem. Interfac.* **1967**, 14, 89.
- [108] T. E. Suarez, R. T. Iwamoto, J. Kleinberg, *Inorg. Chim. Acta* **1973**, 7, 458.
- [109] M. D. Benari, G. T. Hefter, A. J. Parker, *Hydrometallurgy* **1983**, 10, 367.
- [110] M. H. Miles, L. W. McMahon, S. M. Nelson, *J. Phys. Chem.* **1975**, 79, 2312.
- [111] J. Catalán, C. Díaz, F. García-Blanco, *J. Org. Chem.* **2001**, 66, 5846.
- [112] D. M. Muir, P. Singh, C. C. Kenna, G. Senanayake, *Electrochim. Acta* **1989**, 34, 1573.
- [113] Y. Marcus, *Pure Appl. Chem.* **1985**, 57, 1129.
- [114] Y. Marcus, *Pure Appl. Chem.* **1983**, 55, 977.
- [115] K. K. Kundu, A. J. Parker, *J. Solution Chem.* **1981**, 10, 847.
- [116] G. Jarzabek, Z. Borkowska, *J. Electroanal. Chem. Interfac.* **1987**, 226, 295.
- [117] D. Robinson, J. E. Anderson, J. L. Lin, *J. Phys. Chem.* **1990**, 94, 1003.
- [118] A. Hamelin, *J. Electroanal. Chem. Interfac.* **1982**, 142, 299.
- [119] S. K. Si, A. A. Gewirth, *J. Phys. Chem. B* **2000**, 104, 10775.
- [120] M. S. Mousa, *Appl. Surf. Sci.* **1996**, 94-95, 129.
- [121] S. Chen, A. Kucernak, *Electrochem. Commun.* **2002**, 4, 80.
- [122] K. Kinoshita, *Carbon electrochemical and physicochemical properties*, Wiley, New York, **1988**.
- [123] J. P. Randin, in *Encyclopedia of electrochemistry of elements, Vol. VII* (Ed.: A. J. Bard), Dekker, New York, **1976**.
- [124] X. Ma, R. Schuster, *J. Electroanal. Chem.* **2011**, 662, 12.
- [125] L. Reimer, *Scanning electron Microscopy Physics of Image Formation and Microanalysis*, 2nd ed., Springer, Heidelberg, **1998**.
- [126] K. Kanaya, S. Okayama, *J. Phys. D* **1972**, 5, 43.
- [127] A. Lakshmananá, *Luminescence and Display Phosphors: Phenomena and Applications*, Nova Science Pub Inc, New York, **2007**.
- [128] V. I. Petrov, *Phys. Stat. Sol. A* **1992**, 133, 189.
- [129] B. G. Yacobi, D. B. Holt, *Cathodoluminescence microscopy of inorganic solids*, Plenum Press, New York, **1990**.
- [130] G. T. Boyd, Z. H. Yu, Y. R. Shen, *Phys. Rev. B* **1986**, 33, 7923.
- [131] A. Mooradian, *Phys. Rev. Lett.* **1969**, 22, 185.
- [132] E. Dulkeith, T. Niedereichholz, T. A. Klar, J. Feldmann, G. von Plessen, D. I. Gittins, K. S. Mayya, F. Caruso, *Phys. Rev. B* **2004**, 70, 205424.
- [133] J. D. Jackson, *Classical Electrodynamics*, John Wiley & Sons, New York, **1998**.
- [134] V. L. Ginzburg, *Physica. Scripta.* **1982**, T2/1, 182.
- [135] A. J. Garratt-Reed, D.C. Bell, *Energy-dispersive X-ray analysis in the electron microscope* Taylor&Francis, Oxford, **2003**.
- [136] S. Amelinckx, D. van Dyck, J. van Landuyt, G. van Tendeloo, *Handbook of Microscopy Applications in Materials Science Solid-state Physics and Chemistry Method II*, Wiley VCH, Weinheim, **1997**.
- [137] R. H. Ritchie, J. C. Ashley, L. C. Emerson, *Phys. Rev.* **1964**, 135, A759.
- [138] R. H. Hughes, T. A. Heumier, P. M. Griffin, *Appl. Opt.* **1981**, 20, 1350.

- [139] I. Frank, V. Ginzburg, *J. Phys. USSR* **1945**, 9, 353.
- [140] M. L. Ter-Mikaelian, *High-energy electromagnetic processes in condensed media*, Wiley, New York, **1972**.
- [141] N. Yamamoto, H. Sugiyama, A. Toda, *Proc. R. Soc. Lond. A* **1996**, 452, 2279.
- [142] R. P. DiNardo, A. N. Goland, *Phys. Rev. B* **1971**, 4, 1700.
- [143] R. W. Brown, P. Wessel, E. P. Trounson, *Phys. Rev. Lett.* **1960**, 5, 472.
- [144] G. E. Jones, L. S. Cram, E. T. Arakawa, *Phys. Rev.* **1966**, 147, 515.
- [145] E. T. Arakawa, N. O. Davis, R. D. Birkhoff, *Phys. Rev.* **1964**, 135, A224.
- [146] M. S. Chung, T. A. Callcott, E. Kretschmann, E. T. Arakawa, *Surf. Sci.* **1980**, 91, 245.
- [147] M. Kuttge, E. J. R. Vesseur, A. F. Koenderink, H. J. Lezec, H. A. Atwater, F. J. G. d. Abajo, A. Polman, *Phys. Rev. B* **2009**, 79, 113405.
- [148] E. T. Arakawa, L. C. Emerson, D. C. Hammer, R. D. Birkhoff, *Phys. Rev.* **1963**, 131, 719.
- [149] J. T. Van Wijngaarden, Utrecht University (Amsterdam), **2005**.
- [150] J. T. Van Wijngaarden, E. Verhagen, A. Polman, C. E. Ross, H. J. Lezec, H. A. Atwater, *Appl. Phys. Lett.* **2006**, 88, 221111.
- [151] P. Dawson, F. de Fornel, J. P. Goudonnet, *Phys. Rev. Lett.* **1994**, 72, 2927.
- [152] J. Renger, Technische Universität Dresden (Dresden), **2006**.
- [153] N. Yamamoto, T. Suzuki, *Appl. Phys. Lett.* **2008**, 93, 093114.
- [154] N. Behr, M. B. Raschke, *J. Phys. Chem. C* **2008**, 112, 3766.
- [155] V. Halka, M. J. Schmid, V. Avrutskiy, X. Ma, R. Schuster, *Angew. Chem. Int. Ed.* **2011**, 50, 4692.
- [156] H. D. Hattendorff, *Phys. Stat. Sol. A* **1977**, 42, 489.
- [157] K. J. Dana, J. Wang, *J. Opt. Soc. Am. A* **2004**, 21, 1.
- [158] J. A. Sanchez-Gil, *Appl. Phys. Lett.* **1998**, 73, 3509.
- [159] A. A. Maradudin, R. F. Wallis, G. I. Stegeman, *Prog. Surf. Sci.* **1990**, 33, 171.
- [160] J. A. Sánchez-Gil, A. A. Maradudin, *Phys. Rev. B* **1999**, 60, 8359.
- [161] B. Vohnsen, S. I. Bozhevolnyi, *Appl. Opt.* **2001**, 40, 6081.
- [162] N. Yamamoto, S. Ohtani, F. J. G. d. Abajo, *Nano Lett.* **2011**, 11, 91.
- [163] L. Novotny, B. Hecht, *Principles of Nano-optics*, Cambridge University Press, Cambridge, **2006**.
- [164] P. Bharadwaj, B. Deutsch, L. Novotny, *Adv. Opt. Photon.* **2009**, 1, 438.
- [165] L. Novotny, S. J. Stranick, *Annu. Rev. Phys. Chem.* **2006**, 57, 303.
- [166] C. Neacsu, G. Steudle, M. Raschke, *Appl. Phys. B* **2005**, 80, 295.
- [167] E. J. Sánchez, L. Novotny, X. S. Xie, *Phys. Rev. Lett.* **1999**, 82, 4014.
- [168] A. V. Zayats, V. Sandoghdar, *Opt. Commun.* **2000**, 178, 245.
- [169] L. Novotny, E. J. Sánchez, X. S. Xie, *Ultramicroscopy* **1998**, 71, 21.
- [170] A. Hartschuh, *Angew. Chem. Int. Ed.* **2008**, 47, 8178.
- [171] W. Zhang, X. Cui, O. J. F. Martin, *J. Raman Spectrosc.* **2009**, 40, 1338.
- [172] L. Novotny, R. X. Bian, X. S. Xie, *Phys. Rev. Lett.* **1997**, 79, 645.
- [173] A. Downes, D. Salter, A. Elfick, *J. Phys. Chem. B* **2006**, 110, 6692.
- [174] Y. C. Martin, H. F. Hamann, H. K. Wickramasinghe, *J. Appl. Phys.* **2001**, 89, 5774.
- [175] R. M. Roth, N. C. Panoiu, M. M. Adams, R. M. Osgood, C. C. Neacsu, M. B. Raschke, *Opt. Express* **2006**, 14, 2921.
- [176] C. C. Neacsu, G. A. Reider, M. B. Raschke, *Phys. Rev. B* **2005**, 71, 201402.

- [177] B. Ren, G. Picardi, B. Pettinger, *Rev. Sci. Instrum.* **2004**, *75*, 837.
- [178] M. G. Boyle, L. Feng, P. Dawson, *Ultramicroscopy* **2008**, *108*, 558.
- [179] E. Bailo, V. Deckert, *Chem. Soc. Rev.* **2008**, *37*, 921.
- [180] K. Dickmann, F. Demming, J. Jersch, *Rev. Sci. Instrum.* **1996**, *67*, 845.
- [181] C. Zhang, B. Gao, L. G. Chen, Q. S. Meng, H. Yang, R. Zhang, X. Tao, H. Y. Gao, Y. Liao, Z. C. Dong, *Rev. Sci. Instrum.* **2011**, *82*, 083101.
- [182] R. Berndt, R. R. Schlittler, J. K. Gimzewski, *J. Vac. Sci. Technol. B* **1991**, *9*, 573.
- [183] C. Ropers, C. C. Neacsu, T. Elsaesser, M. Albrecht, M. B. Raschke, C. Lienau, *Nano Lett.* **2007**, *7*, 2784.
- [184] J. B. Marion, M. A. Heald, *Classical electromagnetic radiation*, 2nd ed., Academic Press, Orlando, **1980**.
- [185] J. Lambe, S. L. McCarthy, *Phys. Rev. Lett.* **1976**, *37*, 923.
- [186] G. Binnig, H. Rohrer, C. Gerber, E. Weibel, *Appl. Phys. Lett.* **1982**, *40*, 178.
- [187] C. J. Adkins, W. A. Phillips, *J. Phys. C* **1985**, *18*, 1313.
- [188] R. Wiesendanger, *Scanning probe Microscopy Analytical Methods*, Springer, Heidelberg, **1998**.
- [189] N. Nilius, N. Ernst, H. J. Freund, *Phys. Rev. B* **2002**, *65*, 115421.
- [190] R. Berndt, J. K. Gimzewski, P. Johansson, *Phys. Rev. Lett.* **1993**, *71*, 3493.
- [191] R. Berndt, R. Gaisch, W. D. Schneider, J. K. Gimzewski, B. Reihl, R. R. Schlittler, M. Tschudy, *Phys. Rev. Lett.* **1995**, *74*, 102.
- [192] V. Sivel, R. Coratger, F. Ajustron, J. Beauvillain, *Phys. Rev. B* **1992**, *45*, 8634.
- [193] C. Maurel, R. Coratger, F. Ajustron, G. Seine, R. Péchou, J. Beauvillain, *Eur. Phys. J-Appl. Phys* **2003**, *21*, 121.
- [194] C. Noguez, *J. Phys. Chem. C* **2007**, *111*, 3806.
- [195] M. J. Gallagher, S. Howells, L. Yi, T. Chen, D. Sarid, *Surf. Sci.* **1992**, *278*, 270.
- [196] N. J. Watkins, J. P. Long, Z. H. Kafafi, A. J. Mäkinen, *Rev. Sci. Instrum.* **2007**, *78*, 053707.
- [197] G. Hoffmann, J. Kröger, R. Berndt, *Rev. Sci. Instrum.* **2002**, *73*, 305.
- [198] S. Ushioda, *Solid State Commun.* **2001**, *117*, 159.
- [199] Y. Khang, Y. Park, M. Salmeron, E. R. Weber, *Rev. Sci. Instrum.* **1999**, *70*, 4595.
- [200] C. J. Chen, *Introduction to Scanning Tunneling Microscopy*, Oxford University Press, Oxford, **1993**.
- [201] M. M. J. Bischoff, M. C. M. M. van der Wielen, H. van Kempen, *Surf. Sci.* **1998**, *400*, 127.
- [202] B. L. Weeks, M. W. Vaughn, J. J. DeYoreo, *Langmuir* **2005**, *21*, 8096.
- [203] M. G. Boyle, J. Mitra, P. Dawson, *Nanotechnology* **2009**, *20*, 335202.
- [204] R. García, M. Calleja, F. Pérez-Murano, *Appl. Phys. Lett.* **1998**, *72*, 2295.
- [205] R. W. Rendell, D. J. Scalapino, *Phys. Rev. B* **1981**, *24*, 3276.
- [206] F. Rossel, M. Pivetta, W. D. Schneider, *Surf. Sci. Rep.* **2010**, *65*, 129.

# Acknowledgments

First, I would like to express my gratitude to my supervisor Prof. Dr. Rolf Schuster for the opportunity to work under his supervision. I am grateful to him for his patient instructions, guidance, many meaningful discussions and he provided pressure-less and open mind research environment. I also sincerely thank him for his understanding, acceptance, supporting and encouragement.

I am sincerely grateful to PD. Dr. Detlef Nattland for his carefully reading of my thesis and his very meaningful discussions and suggestions on my thesis. I also thank his supporting during these years.

I sincerely thank Prof. Dr. Werner Freyland for his help and many friendly discussions.

I am sincerely grateful to Ms. Daniela Rohmert-Hug for her patient help in daily life.

I am sincerely thankful to all my colleagues for the friendly atmosphere and the nice time we spent together as well as their friendly help and support in scientific life and daily life: Axel, Katrin, Kai, Jens, Judith, Martin, Matthias, Raphael, Vadym, Essen and Olivier, especially to Raphael and Katrin for their help to translate the abstract to German.

I would also like to thank Mr. Dieter Waltz and his colleagues from the mechanics workshop for their help in mechanical constructions of the experimental set-up and their patient discussions and their many helpful advices.

I am sincerely thankful to my master thesis supervisor Ass. Prof. Jing Tang and Prof. Bin Ren for their recommendation to let me have the opportunity to work here in this



nice group.

Finally, I want to thank my family for their unconditional supporting, especially to my wife, Manfang, for her supporting and encouragement. I also thank her for her careful reading of my thesis and the correction of English.

# Publications

1. Electrochemical Machining of Gold Microstructures in LiCl/Dimethyl Sulfoxide.

X. Ma, A. Bán, R. Schuster, *ChemPhysChem* **2010**, *11*, 616.

2. Locally Enhanced Cathodoluminescence of Electrochemically Fabricated Gold Nanostructures.

X. Ma, R. Schuster, *J. Electroanal. Chem.* **2011**, *662*, 12

3. Electron-Beam-Induced Deposition of Metallic Microstructures from a Molten-Salt Film on Conductive and Nonconductive Substrates.

V. Halka, M. J. Schmid, V. Avrutskiy, X. Ma, R. Schuster, *Angew. Chem. Int. Ed.* **2011**, *50*, 4692.

# Curriculum Vitae

## PERSONAL DATA:

Family Name: Ma

First Name: Xinzhou

Date of Birth: July 17<sup>th</sup>, 1981

Place of Birth: Guangdong, China

Nationality: Chinese

## Education:

**16. 12. 2011**

**Ph.D Defense**

**Since 09/2007**

**Ph.D Student**

Institute of Physical Chemistry, Karlsruhe  
Institute of technology (KIT), Germany  
Supervisor: Prof. Dr. Rolf Schuster

**09/2004 – 07/2007**

**Master Degree in Applied Chemistry**

School of Chemistry and Chemical engineering,  
Xiamen University, China

**09/2000 – 07/2004**

**Bachelor Degree in Material Science and  
Technology**

School of Science, Shenzhen University, China

**09/1997 – 07/2000**

Shimen High School, Nanhai, China

**09/1994 – 07/1997**

Dabu Middle School, Nanhai, China

**09/1988 – 07/1994**

Yanfeng Elementary School, Nanhai, China